LOCALIZED DEFORMATION IN SOFT SOLIDS
AROUND SPHERICAL CAVITIES

BY

MATTHEW P. MILNER

DISSERTATION

Submitted in partial fulfillment of the requirements
for the degree of Doctor of Philosophy in Mechanical Engineering
in the Graduate College of the
University of Illinois at Urbana-Champaign, 2020

Urbana, Illinois

Doctoral Committee:

Assistant Professor Shelby B. Hutchens, Chair
Professor John Lambros
Associate Professor Oscar Lopez-Pamies
Professor Sascha Hilgenfeldt

Abstract

Biological tissue, like internal organs, brain, or skin, are soft solids that may be exposed to injury inducing mechanisms at a range of rates, resulting in damage. Sport injuries, car crashes, traumatic brain injury, and ballistic impacts can produce strain rates from $10-10^5$ 1/s. The parameters governing failure in these soft solids (moduli $<$ 1 MPa) are challenging to quantify, requiring modifications or defying the use of traditional characterization techniques. Driving bubble/droplet growth or contraction provides a way to characterize these materials while avoiding some limitations of traditional techniques. Large deformations in these spherical geometries induce localized deformations at the surface of the cavity. In this thesis, I leverage these localized deformations, cracks during expansion and creases during contractions, to investigate fracture energy and strain stiffening, respectively.

A Small-scale Ballistic Cavitation device uses a high-pressure air reservoir to generate spherical deformation at high rates within soft solids. Air accelerates through a needle, reaching the speed of sound at the tip before delivery to the sample. The energy density of the air pulse matches that of bullets, producing small, ballistic-like cavitations. Independent control of pressure, needle diameter, and valve cycle time provides flexibility in experimental control variables not available in other ultrasoft solid cavitation techniques.

Using these needle-mediated, high rate spherical expansions, I investigate the parameters governing fracture initiation in soft solids by adapting a theory of fracture traditionally used in dynamic failure in hard materials. I present results from cavity expansions in silicone and gelatin samples. Increasing the rate of expansion increases the number of cracks initiated in the cavity surface, leading to multi-lobed cracks, as opposed to the penny-shaped cracks present in quasi-static cavitations. The elastic wave speed-dependent fracture correlation model I adapt suggests that counting the number of cracks provides a measure of the soft solid's fracture energy. Additionally, I include the implications of this model for analytical calculations in very tough, nonlinear materials. Finally, I demonstrate the multiple fracture phenomenon in ballistic impacts and present a method for analyzing damage that draws upon the understanding gained in from the bench-scale cavity expansions.

In the last chapter, I report on crease morphology and evolution at the surface of contracting cavities embedded within elastomeric solids of varying degrees of crosslinking. Cavity contraction is achieved through evaporation of an embedded water droplet. In validation of theoretical predictions, strain-stiffening is found to govern both crease onset and crease density. Neo-Hookean solids are found to prefer initiating creasing with many short creases that join to form a collapsed state with only a few creases, whereas creasing in Gent solids initiates with a few creases that propagate across the cavity surface.

To my family.

Acknowledgments

First, I would like to thank my advisor Shelby Hutchens for giving me the freedom and support to conduct research on something that has always fascinated me. I appreciate it and am glad that we were able to align our interests. The helpful insights and perspective she provided to get through the sticking points that always arise during research were much appreciated. Her meticulous approach to research and communicating those findings has made me both a better scientist and writer. Next, I would like to thank my committee members, Professor John Lambros, Professor Oscar Lopez-Pamies, and Professor Sascha Hilgenfeldt for their guidance and helpful discussions as I developed explanations and a path forward with some of my early findings. All your expertise helped me frame the problem in the correct way and avoid the dead ends. I am very appreciative to the MechSE Department for the years of funding my education with the TAM 2XX Head TA appointment. And many thanks to the various TAM 2XX instructors who I worked with for making it a positive, enjoyable, and impactful experience. I would like to thank the MechSE Machine Shop for their helpful insight and skills in developing my Small-scale Ballistic Cavitation device. Additionally, I would like to thank Dynamic Structures and Materials for working with me on implementing their piezoelectric actuators with my device and the helpful insight on engineering it for the best valve operation. And most importantly, for helping me do it again (and better) after a mishap! Additionally, I would like to thank my fellow labmates Bingyang and Amrita for making my research experience better and letting me bounce both research thoughts and otherwise off them. To all the MechSE staff, especially Kathy Smith, who are the most kind and helpful people, thank you.

Finally, to my family: Mom, Dad, Alexis, Samantha, Mackenzie, and all those in Ohio; thank you for your support, I love y'all. And to Grandad, the only other mechanical engineer in the family, you first got me interested in firearms and shooting, thank you. You were always there for me, thanks for coming to the decade-plus of those football practices and I am glad that you got to see me play at ECU, wish you were here to see this, *Semper Fi*. And "what'd ya say," you were right, I've become an engineer and they haven't let me drive a train yet.

Contents

List of Tables . . . . **x**

List of Figures . . . . **xi**

Chapter 1 Introduction **1**
- 1.1 Why do we need more high rate failure testing of soft materials? 3
- 1.2 Localizations during spherical contraction 5
- 1.3 Research aims 6

Chapter 2 A device to fracture soft solids at high speeds **7**
- 2.1 Overview 7
- 2.2 Introduction 8
- 2.3 Design Constraints 10
- 2.4 Device Design 14
  - 2.4.1 Operating at High Chamber Pressure 14
  - 2.4.2 Varying Needle Geometry 15
  - 2.4.3 High Speed Valve Control 17
- 2.5 Results and Discussion 17
  - 2.5.1 Verification of Experimental Performance 18
  - 2.5.2 Demonstration of Variable Control 20
- 2.6 Summary and Conclusions 23
- 2.7 Acknowledgements 23
- 2.8 Supplementary Information 23
  - 2.8.1 Ballistic Energy Density 23
  - 2.8.2 Derivation of Energy Balance 24
  - 2.8.3 Flow Equations 25
  - 2.8.4 Fanning Friction Factor 27
  - 2.8.5 Device Sealing Details 28

Chapter 3 Multi-crack formation in soft solids during high rate cavity expansion **29**
- 3.1 Overview 29
- 3.2 Introduction 29
- 3.3 Crack Formation at High Rates 32
- 3.4 Methods and Materials 37
  - 3.4.1 Sample Preparation 37
  - 3.4.2 High-Rate Cavity Expansion Procedure 38
  - 3.4.3 Image Processing 40

3.5 Experimental Results and Discussion 40
3.5.1 Overview of Experimental Results 40
3.5.2 Evolution of Cavity Morphology 42
3.5.3 Relating Number of Cracks to Fracture Energy 46
3.6 Conclusion 51
3.7 Acknowledgements 52
3.8 Supplementary Information 53

Chapter 4 The effect of material non-linearity on dynamic fracture length scale 66
4.1 Overview 66
4.2 Introduction 66
4.3 Modeling Number of Cracks Formed 67
4.3.1 Crack Correlation Length 67
4.3.2 Onset of fracture 69
4.4 Comparing Linear and Non-linear Predictions 72
4.5 Conclusions 72
4.6 Supplementary Information: Instantaneous Wavespeed 74

Chapter 5 Multi-crack formation in ballistic impacts 75
5.1 Overview 75
5.2 Methods and Materials 75
5.2.1 Ballistic Gelatin Preparation 75
5.2.2 Ballistic Impacts 76
5.3 Experimental Results and Discussion 76
5.3.1 Overview of Experimental Results 76
5.3.2 Multiple Crack Formation in Ballistic impacts 79
5.3.3 Energy Effects on Damage Formation 80
5.3.4 Rate Effects on Damage Formation 83
5.3.5 Multiple Fracture Theory Applied to Ballistic Impacts 85
5.4 Conclusion 85
5.5 Acknowledgements 86

Chapter 6 Creasing in evaporation-driven cavity collapse 87
6.1 Overview 87
6.2 Introduction 87
6.3 Methods 91
6.3.1 Cavity Sample Fabrication and Testing 91
6.3.2 Compression Sample Fabrication and Testing 91
6.3.3 Finite element simulation 92
6.4 Results and Discussion 92
6.4.1 Evaporation During Breathing Mode 93
6.4.2 Crease Onset 95
6.4.3 Crease Morphology and Evolution 98
6.4.4 Cavitation and Surface ‘Bubble’ Formation 105
6.5 Conclusions 107
6.6 Acknowledgments 108
6.7 Supplementary Information 108
6.7.1 Crease Onset 108

6.7.2 Homogeneous Cylinder Deformation 109
6.7.3 Characterization of Sylgard 184 at Room Temperature and Hydrated at 60 °C 110
6.7.4 Quantification of Crease Morphology 110
6.7.5 Cavitation Event Frequency 111
6.7.6 Crease Onset Interpolation 111
6.7.7 Strain Hardening 112
6.7.8 ‘Microbubbles’ on Void Surface 113
6.7.9 Finite Element Simulation 114

Chapter 7 Summary and Outlooks 118

Chapter 8 Bibliography 121

List of Tables

2.1 SBC components 16

5.1 Bullet and ballistic impact characteristics 77

6.1 Shear moduli (μ) and strain hardening (J_{lim}) fit parameters Sylgard 184 . . . 111
6.2 Crease counts during cavity contraction 113

List of Figures

2.1 Overview of Small-scale Ballistic Cavitation device and experiments 9
2.2 SBC flow path and energy output 13
2.3 Visualization of device components 15
2.4 SBC experimental performance and validation 19
2.5 Varying rate of energy density transfer 22

3.1 Overview of multiple fracturing experimental setup and representative results 31
3.2 Cavity schematic and effect of material rate dependence on crack formation . 33
3.3 PDMS and gelatin strain rate dependence 38
3.4 Cavity wall velocity 41
3.5 Cavity crack evolution 43
3.6 Crack number dependence on fracture behavior 44
3.7 Intermediate time-scale cavity morphology for two mass fraction PDMS cavitations 46
3.8 Final cavity morphology for two mass fraction PDMS cavitations 47
3.9 Cavitations performed in 35:$1_{20\%}$ PDMS for three needle sizes 48
3.10 Fracture energy predictions 49
3.11 Cavitations performed in 10% ballistic gelatin for three needle sizes 51
3.12 Mesoscale ballistic cavitation device 54
3.13 Intermediate time-scale cavity morphology for all samples of crosslinker mass fraction, $f_x = 0.019$ 55
3.14 Intermediate time-scale cavity morphology for all samples of crosslinker mass fraction, $f_x = 0.022$ 56
3.15 Final cavity morphology for all samples of crosslinker mass fraction, $f_x = 0.019$ 57
3.16 Final cavity morphology for all samples of crosslinker mass fraction, $f_x = 0.022$ 58
3.17 High speed images of cavities in silicone (crosslinker mass fraction, $f_x = 0.019$) 59
3.18 High speed images of cavities in silicone (crosslinker mass fraction, $f_x = 0.022$) 60
3.19 High rate cavity morphology of $35 : 1_{20\%}$ PDMS at different needle sizes 61
3.20 Brittle crack formation in PDMS formulations 62
3.21 Cavitation images in gelatin (178 μm radius needle) 63
3.22 Cavitation images in gelatin (496 μm radius needle) 64
3.23 Cavitation images in gelatin (788 μm radius needle) 64
3.24 Cavitations in 20% gelatin (178 μm needle) 65

4.1 Nonlinear failure onset dependence on the elasto-fracture parameter $\Gamma/\mu A_0$. 70
4.2 Predictions for the number of cracks formed in expanding spherical cavities . 73

5.1 Image of firing range at Police Training Institute Tactical Training Center . . . 78
5.2 Temporary cavity expansion images 79
5.3 Total Crack Area (TCA) measurements 82
5.4 Ballistic impact analysis: Total Crack Area 83
5.5 Bullet kinetic energy and cavity wall velocity 84
5.6 Bullet expansion radii estimates for multiple fracture theory 86

6.1 Overview of creasing experimental setup 89
6.2 Droplet evaporation experimental setup and modeling 92
6.3 Cavity morphology evolution for varying elastomer composition 94
6.4 Verification of delayed crease onset due to early onset of strain-stiffening as quantified by J_{lim} 96
6.5 Strain-stiffening material behavior of hydrated Sylgard 184 at 60 °C 97
6.6 Quantified crease morphology evolution 99
6.7 Simulated results for crease number trends for a cylindrical tube 100
6.8 Simulated crease number trends neo-Hookean and strain stiffening materials . 102
6.9 Surface energy effects on creasing in a cavity 106
6.10 Example crease images for 10:1 and 25:1 PDMS mixing ratios 112
6.11 Predicted crease onset from published data 113
6.12 Corresponding limiting stretch value, λ_{lim} for a given J_{lim}. 114
6.13 Optical micrographs of the ‘microbubbles’ at the surface of a cavity 115
6.14 Typical meshing used in FE simulation 116
6.15 Results from convergence studies of mesh refinement 117

Chapter 1

Introduction

Despite their importance and prevalence in biology, the properties of soft solids have proven particularly challenging to measure. In particular, materials like elastomers, polymers, and gels - typically with an elastic modulus < 1 MPa - often exhibit rate dependent behavior and a non-linear constitutive response that accompanies finite deformations. Their mechanical behavior shares characteristics of both hard materials and fluids; as a result, characterizing soft solid mechanical behavior using traditional experimental techniques poses several complications. These challenges arise from several features inherent to soft solids, including low stiffness, stickiness, and fragility, all of which combine to make manipulation of soft-solids into a testing apparatus difficult and can lead to premature failure during testing procedures typical of hard materials.

Successful experimentation on soft solids has required both reframing traditional characterization techniques and developing novel methods. Bubble-induced deformation is one approach that has been utilized to probe criticalities within fluids. When bubbles can be formed inside soft-solids, many of the challenges due to handling and manipulating the materials go away, and one only needs a reliable method of bubble generation. Bubbles generate a three-dimensional surface as opposed to typical planar test geometries, but since expansion is pressure driven, radial symmetry is maintained for small bubble deformations, simplifying analysis. At larger bubble expansions or contractions, localized deformations emerge at the surface of the spherical cavity where stretch in the soft solid is highest. These events occur when criticalities are attained and the homogeneity of the spherical surface is disrupted at isolated points. During expansions, such localized events equate to crack formation, while during contractions, creases form. This work exploits fluid driving forces to generate spherical deformation for mechanical property characterization using both types of bubble-driven deformation. Using a fluid driving force allows both rate and degree of deformation to be tuned to explore mechanical properties that are time or stretch dependent and difficult or impossible to measure with any other method.

Recently, new spherical deformation techniques have been proven experimentally useful in characterizing the mechanical properties of soft solids, beginning with quasi-static rates and progressing toward dynamic rates. Cavitation Rheology (CR) is a quasi-static, fluid-transfer method that generates unstable cavity expansion at a needle tip via an applied fluid pressure.[1–3] Mechanical properties, such as modulus or critical strain energy release rate, are measured by relating the critical pressure required to initiate cavitation/fracture. Building on this phenomenon, recent work has stressed the balance of elastic and fracture properties of the material during deformation and shown that fractures can appear at smaller strains than anticipated.[4–8] The geometry and size of defects as well as the nonlinear elastic stiffening response also have an influence on the development of damage and progression of damage.[5–8]

Dynamic methods of cavitation use laser pulsing[9] or ultrasound bursts.[10] The laser pulsing technique, known as Inertial Microcavitation Rheology (IMR), focuses on time-dependent viscoelastic material characterization, while researchers applying the ultrasound technique verify the criteria for damage onset due to material fatigue. The IMR technique primarily focuses on bubble oscillation and recovery for fitting viscoelastic properties, but by just examining oscillations after maximum strain has occurred it does not address the fracture properties of the material that determine cavity creation. The ultrasound technique cycles loading hundreds of times to induce failure and has no systematic control on the initial geometry and size of defects which, as indicated above, has an influence on the development of fracture. By developing a controllable and reliable technique that drives a single high-rate spherical expansion while also observing the expanding deformation, the properties of fracture critical in soft-solids can be examined for predicting terminal ballistic outcomes.

In classic penetration mechanics, a phenomenon also known as cavitation occurs when an impacting projectile forms a hole in a target larger than projectile. In terminal ballistics the penetration and failure mechanisms of projectile (metal) and target (metal, ceramic) interactions have been extensively studied,[11–17] but this continued to prove difficult for penetration of soft solids. Cavitation in penetration mechanics was first studied around WWII[11] when a quasi-static model was developed to predict the pressure required to enlarge a spherical or cylindrical hole.[13] Building off of cavity expansion studies,[12] the theory progressed to explanations of dynamic penetrations.[14–16,18,19] Dynamic penetration theory was then extended to hard projectile impacts in soft targets which exhibit similar cavitation phenomenon, but on a temporary time scale since they collapse.[20–22] Characterization of soft target cavitation, particularly the energy required to expand a cavity, lags behind hard materials because modulus and fracture energy of soft materials during high rate loading are largely unreported.[22,23] Large apparent stretches are observed in the 'temporary' cavities that form in ballistic gelatins subject to projectile penetration, so fracture is expected and radial cracks are often observed.[24] Motivated by the observations of ballistic impacts causing cavitation and fracturing phenomenon in soft solids via a radial expansion and previous needle-based testing techniques, I designed a high-rate, fluid-driven device to produce similar phenomenon in soft solids at benchtop scales,[25] described in Chapter 2. As I then show in Chapter 3, the device allows for systematic investigation of fracture response of soft-solids and elucidates the physics of crack formation.

1.1 Why do we need more high rate failure testing of soft materials?

Biological tissue, like internal organs, brain, or skin, are typical soft solids that may be exposed to a range of stimuli from injury inducing mechanisms at a range of rates and magnitudes of damage. Sport injuries, car crashes, traumatic brain injury, and the ballistic impacts discussed above can produce strain rates from $10 - 10^5$ 1/s with damage spread over large areas or localized in small areas of the body. However, revamping traditional high-rate techniques to be used on soft solids increases in complexity from the already challenging sample handling, large deformation, and signal-to-noise issues encountered when applying quasi-static techniques to soft solids.

Dynamic experimentation techniques that have been applied to soft solids include many borrowed from hard material studies, including the drop tower,[26,27] Hopkinson bar,[28–30] ballistic impacts,[22,31,32] and plate impacts.[33,34] These tests span the strain rates (10^1 to 10^5 1/s) relevant to tissue injury stimuli. Extracting moduli with these techniques requires several modifications arising from lower stiffness and yield strength and higher strain-to-failure than the hard materials for which the tests were designed.[35,36] Investigation of non-linear constitutive response has not yet been achieved with these types of methods since they lack the ability to drive strain far enough while maintaining measurement resolution and ability to detect nonlinearities along loading curves.[33,34,37–39] Failure experimentation on some soft solids utilizes the high-rate mechanisms discussed above; however, they are not used on the softest materials (with modulus $\leq$ 100 kPa).[40] Other traditional methods of high rate experimentation, extensively used with hard materials, include ballistic impact, explosives, or electromagnetic loading. Excluding ballistic impacts, these techniques have not generally been applied to soft solids.

Using the device that I describe in Chapter 2 to generate high-rate spherical expansion in soft solids,[25] I observed damage around expanding cavities that manifests as multiple radial cracks.[41] This behavior is reminiscent of an existing high-rate experimental geometry applied to hard materials that utilizes an expanding ring.[42] The expanding ring experiment induces radial loading with explosive or electromagnetic loading to cause dynamic deformation and fracture in a one-dimensional radial geometry.[43] Observations and explanations of dynamic ring expansion began with Mott in 1947 who studied the fragmentation of artillery shells[44] and developed fragment number predictions based on loading and material properties. Mott assumed a statistical distribution of flaws for crack initiation and assumed that stress wave propagation from fracture sites relieved stress in regions around cracked areas. Furthering this fragmentation theory, Grady[45,46] used energetic, Griffith-like fracture considerations to predict fragment size. The fractured fragment area was determined by an energetic minimum specific to the loading rate and material properties. Extrapolating from the ring geometry and adapting these principles to the geometry of a hole within a solid, the same energetic considerations can be used to predict radial cracking from a high rate impulse inside a hole. The size of the hole, loading rate, and properties of the material to be fractured determine how many radial cracks form, which has value in guiding blasting for rock excavation or oil recovery.[47,48] In Chapter 3, I show that the multiple cracking phenomenon generated by my device can be explained by adapting this fragmentation theory for soft solids and that this technique could be used to extract quasi-static and high-rate fracture energies in soft solids. In Chapter 4, I discuss the implications of nonlinear material behavior on this theory, and then in Chapter 5, I show that ballistic impacts undergo a similar fracture process when cavitation occurs and propose a method of accounting for the damage.

1.2 Localizations during spherical contraction

Creasing is a type of localized deformation that occurs when a surface is compressed rather than stretched. Creasing, like crack formation, is driven by an energetic comparison between a creased and an uncreased state of deformation.[49] The crease forms during deformation when the energy in a system to crease is less than the energy to remain in a homogenous state. In soft materials this point is strain dependent and determined by nonlinear material properties, like strain stiffening.[50] Using the spherical geometry of a fluid bubble to observe contractions maintains the same benefits of minimal sample manipulation as already discussed. The cohesive strength and surface energy of the water enables quasi-static contraction as the bubble evaporates through the solid elastomer. In Chapter 6, I demonstrate the use of this deformation to characterize strain stiffening properties by observing creases during deformations in soft solids.[51] This achieves indirect determination of strain stiffening onset for the softest solids, which cannot be determined in bulk mechanical testing.

1.3 Research aims

This dissertation focuses on novel methods to induce and measure both spherical expansion and contraction in soft solids, and the localized deformations generated by each. In the second chapter, a device is developed to generate high-rate, spherical expansions. Motivated by the earlier discussion, this device fills a need for a method to generate high-rate expansions with control over deformation rate, deformation size, energy deposited, and fixed initial geometry (needle). In Chapter 3, using the developed device and similar fluid driven cavitation methods, high rate expansions are used to demonstrate differences in the fracture response of soft solid tissue simulants at high versus quasi-static rates. This theory allows for quantification of a soft solid's fracture energy by examination of the fractured surface. Implications of the results are extrapolated to other classes of materials in Chapter 4, by providing for nonlinear and finite deformation implications of the fracture theory. These fracture principles and findings from material characterization are then applied back to ballistic impacts in Chapter 5, which indicates a nonlinear rate dependent response to damage that was previously considered linear. In the final chapter, I establish creasing as a mechanism to characterize strain stiffening using quasi-static contractions.

Chapter 2

A device to fracture soft solids at high speeds

2.1 Overview

We describe the development of a device capable of high-rate, fluid-driven (pneumatic), spherical deformation to induce fracturing localized deformations. It fills a need for a method to generate high-rate expansions with control over deformation rate, deformation size, energy deposited, and fixed initial geometry (needle). The Small-scale Ballistic Cavitation (SBC) device uses a high-pressure reservoir to generate cavities within ultrasoft solids (moduli $<$ 100 kPa) in bursts as short as 3.8 ms. Flow accelerates through a needle embedded within a soft solid, reaching the speed of sound at the tip before delivery to the sample. The energy density of the air pulse matches that of handgun projectiles, enabling ballistic-like temporary cavities, but on a benchtop scale instead of requiring a shooting range. We validate the device using mass transfer measurements and find good agreement without the use of fit parameters between experiments and theory at the required operational pressures ranging from $\sim$30 to 160 atm. Independent control of pressure, needle diameter, and valve cycle time provides flexibility in experimental control variables (e.g., energy density, rate) that is not present in other ultrasoft solid cavitation techniques. The application of constant energy density with variable loading rate conditions demonstrates of the device's experimental flexibility and illustrates the importance of rate on fracture morphology in soft solids.

2.2 Introduction

The failure response of soft materials at high rates plays a critical role in the accumulation and extent of tissue damage associated with traumatic brain injury,[52–54] ultrasound-based destructive techniques[55,56], and ballistic trauma.[21] These injuries typically occur at high strain rates ($10^2 - 10^4$ 1/s) that present a challenge to traditional testing setups developed for hard materials,[57,58] though recent work has developed modifications enabling limited extension to soft solids.[27,59–61] Furthermore, a nominally radial deformation state is common to all of the above injuries. Here we report on a new needle-mediated, high-rate, cavity-generating device based on the quasi-static Cavitation Rheology (CR) method for inducing cavity expansion at the tip of an embedded needle under an applied critical pressure.[1–3]

Rather than quasi-statically increasing the pressure within the needle as in CR, we rapidly discharge a high-pressure pulse of air in under 5 ms (Figure 2.1b). Controlling pressure and needle geometry, we achieve ballistically-relevant input energy densities (normalized by probe-size) within a bench-top footprint. This Small-scale Ballistic Cavitation (SBC) device will enable rapid characterization of the failure properties of tissues and tissue phantoms.

Techniques currently utilized to characterize soft solids (primarily gels) under high-rate, nominally "cavity-inducing" loading conditions include Inertial Microcavitation high strain-rate Rheometry (IMR)[9], ultrasound-induced cavitation[10], and terminal ballistic testing.[31,62,63] We include the latter given the presence of a shock-load-induced "temporary cavity" that results in large radial stretch upon ballistic impact. Of these techniques, only IMR has the main focus of material characterization. Like IMR, our technique enables visualization via site-specific, localized deformation as opposed to the diffuse damage incurred at intrinsic flaws throughout the material during ultrasound-induced cavitation. Additional flexibility in SBC loading conditions enables this technique to independently control input energy density and probe or flaw size. SBC also accesses intermediate flaw sizes, crossing over with IMR at the smaller lengths ($\sim$100 μm) and approaching those used in ballistic

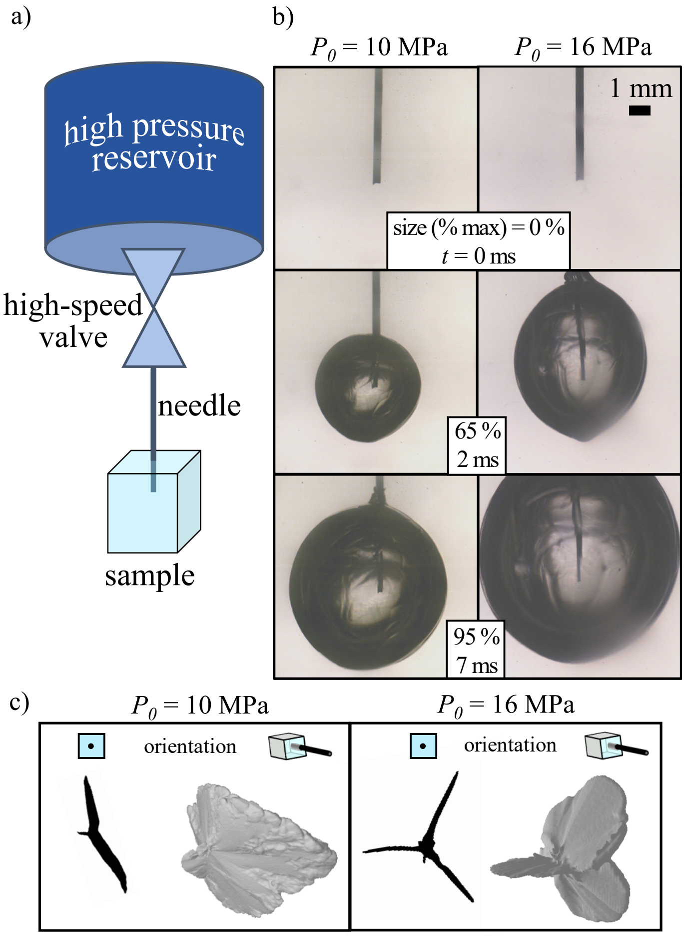

Figure 2.1 Overview of SBC. (a) Using a reservoir pressure, P_0, air pulses are delivered inside a soft material through a needle via a high-speed valve. (b) A series of images illustrate cavity formation following air pulse delivery using $P_0 = 10$ MPa and 16 MPa (needle: 178 μm, pulse time: 5 ms, material: Sylgard 184, 35:1 prepolymer:crosslinker). (c) After cavity inflation, the fractured surface is analyzed via microCT, providing 3D reconstruction of the fracture surface (gray) and enabling characterization of the maximum fractured cross section (black). Oriented cubes are provided for perspective reference. The higher energy density-driven fracture produces a three-lobed morphology, versus the penny-shaped morphology of the lower energy density test.

tests ($\sim$10 mm).[64,65] Finally, SBC maintains many of the strengths of the original CR technique: ease of sample prep for ultralow modulus materials ($<$ 100 kPa), potential *in vivo* and *ex vivo* application, needle-mediated control of the initial flaw size, and no requirement that the material be hydrated. The combination of mesoscale size and ballistically-relevant input energy densities makes SBC a promising technique for exploring damage induced under loading conditions similar to those encountered in traditional ballistic testing. The advantages to this new technique are: the absence of projectile contact or complex projectile dynamics contributions to material loading conditions; the small sample sizes needed, even under the restriction of minimal boundary condition effects; and a small lab footprint, since no shooting range is required. Like projectile testing, the input energy density and probe size (bullet/needle) can be independently tuned. Temporary cavity size, typically many times larger than the projectile size,[66,67] scales monotonically with projectile kinetic energy[21]. However, knowledge of the extent and morphology of fracture/damage that occurs due to this temporary cavity formation is limited. For example, plastically deforming ballistic soaps[21] that allow for post-mortem cavity measurement do not mimic the tissue properties they are approximating. In more elastic ballistic gels, various post-mortem crack length measurements have been used to characterize differences in projectile behavior,[32,62,68] but require numerous expensive tests to approach a quantity of data from which material/projectile interaction may be generalized. Fast, inexpensive SBC will enable *in situ* damage characterization of ballistic tissue simulants, which may lead to improved understanding of the relationship between the phantom material's properties and damage from high rate loading.

This article is organized as follows. We first outline the design constraints and theory governing a pressure-reservoir-driven and needle-delivered air pulse. Next, a discussion of device design choices illustrates the three primary experimental variables: reservoir pressure, pulse time, and needle diameter. We then demonstrate the device's agreement with its behavioral model and end with demonstrations of how to construct energy density-controlled experiments under varying needle size, time, and reservoir pressure conditions.

2.3 Design Constraints

Replicating ballistic temporary cavitation on a small scale requires rapid cavity formation under the driving force of a known energy density while maintaining a small volume. In ballistic testing, temporary cavities reach their maximum size in $\sim$5 ms[63]; this sets the required time scale for device operation, Δt. To keep samples small, we use cubes of less than 5 cm in size. A cavity of $\lesssim 1/5^{\text{th}}$ the sample size minimizes boundary effects. We therefore limit the volume delivered to 5 mL at atmospheric pressure. Despite the low mass transfer required by this constraint, the device reaches ballistically-relevant energy densities using high velocity air.

The SBC device is designed to produce handgun-relevant energy densities (as determined from projectile initial conditions). We calculate typical energy densities ranging from 2.7 to 15 MJ/m^2 (see SI). Normalization of the energy by projectile area produces a relation between the probe size and the generated cavity size that is consistent with previous results.[20,21] This relation allows for bench-top scaling. We estimate a lower bound for energy input using a transient energy balance around the air emerging from the needle tip by assuming a hypothetical scenario in which the initial air mass is zero and the state of the final air mass is determined by needle exit conditions. (h_2 and T_2 are the enthalpy and temperature of air at the needle exit, Figure 2.2a.) Air enters this control volume through the needle at the speed of sound with a constant mass flow rate, $\dot{m}$, but once inside, the air becomes stagnant transferring all kinetic energy to the control volume. The associated energy balance describing the rate of energy change within the system, dU/dt,

$$\frac{\mathrm{d}U}{\mathrm{d}t} = \dot{Q} - \dot{W}_{pV} + \dot{m}\left(h_2 + \frac{v_2^2}{2}\right), \tag{2.1}$$

bounds the work done by the air on the sample, $W_{pV} = \int \dot{W}_{pV} dt$. Fast pulse times ensure an adiabatic process so the heat transfer rate, $\dot{Q} = 0$. Assuming ideal gas behavior[1] and a constant specific heat, c_p, we estimate:

$$W_{pV} = \dot{m}\Delta t \left(R_{\text{air}} T_2 + \frac{v_2^2}{2}\right) \tag{2.2}$$

(see SI for full details). A more accurate estimate requires determination of the final system volume and a measurement of the pressure within it. However, the lower bound provides sufficient guidance for device design by satisfying minimum energy densities.

Eqn. (2.2) requires the state and mass flow rate of air at the needle tip. Air flows through

---

[1] $h = h(T)$ and $p\underline{\mathrm{v}} = R_{\text{air}}T$. p = pressure, $\underline{\mathrm{v}}$ = specific volume, and R_{air} = the ideal gas constant for air.

the device as illustrated in Figure 2.2a. When the valve opens, stagnant air within an infinite reservoir (p_0, T_0) accelerates isentropically through a conical nozzle attaining state p_1, T_1 prior to entering the needle (position 1). The Mach number (v/c), where v is velocity and c is the speed of sound in the air, equals M_1.[2] Within the needle, flow continues to accelerate due to friction (Fanno flow), choking at the needle exit (position 2). Reservoir pressures required for ballistically-relevant pulses ensure choked flow at the needle tip. Given this choking constraint, Fanno flow equations determine the relative state of air at the needle inlet (position 1) (Eqns. (S9-S11)). Isentropic flow relations relate the relative conditions between positions 1 and 0 (Eqns. (S12-S13)). The temperature, pressure, and Mach number within the nozzle-duct system are calculated using these relative states and the known p_0 and T_0 of the reservoir (Fig. 2.2b). Given our steady-state assumption, the mass flow rate is constant within the needle-duct system. For convenience, we choose position 1 to determine the mass flow rate:

$$\dot{m} = \rho_1 A_1 v_1, \tag{2.3}$$

where A_1 is the cross-sectional area of the needle, the density $\rho_1 = p_1/(R_{\text{air}} T_1)$, and $v_1 = M_1 c_1$. Because $\rho_1 \propto p_1$ and isentropic flow relations state that $p_1 \propto p_0$ (Eqn. (S12)), mass flow rate is directly proportional to the reservoir pressure, p_0.

Applying these state and mass flow conditions to Eqn. (2.2), we predict minimum pressure reservoir and needle size requirements for reaching ballistically-relevant energy densities within the 5 ms limit. Fig. 2.2c illustrates these predictions graphically, demonstrating the effect of inner needle diameter (127 - 432 μm) and reservoir pressure on input energy density. Energy is comprised of a thermal component associated with finite temperature mass input and a kinetic component from the stream velocity. Entropic considerations prevent the nozzle-needle geometry from delivering a higher velocity than Mach 1, restricting the contribution from kinetic energy. Exit temperature depends on Mach number and inlet temperature, both of which remain unchanged for fixed inlet conditions. Thus, throughout the range of relevant reservoir pressures, kinetic and thermal energy provide unchanging contributions to the energy input (Fig. 2.2d). While shortening the needle increases the flow

---

[2] assumed to be calorically perfect, $\sqrt{\gamma R_{\text{air}} T}$. $\gamma =$ the ratio of specific heats

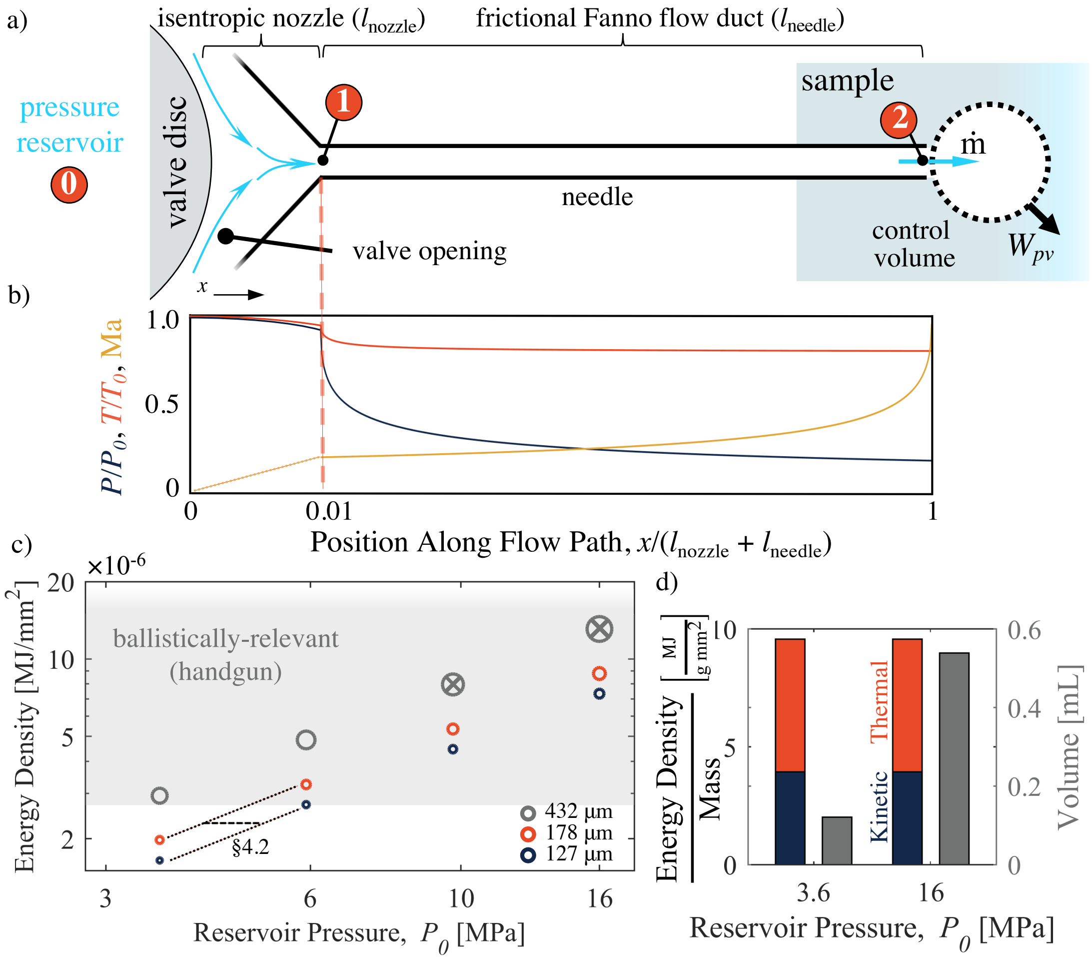

Figure 2.2 Device flow path and energy output. (a) A schematic of the flow path. Position 0 indicates the static state of the reservoir. With the valve open, air isentropically flows to position 1. Upon reaching the uniform needle duct, air accelerates to the needle tip at position 2 before entering a sample. (b) The relative change of pressure, temperature, and Mach number throughout the flow path shown in (a) for a 57 mm long, 127 μm diameter needle having a friction factor of 0.009. (c) Predicted energy density as a function of pressure for three needle diameters. The gray shaded region indicates ballistically-relevant values. Marker size corresponds to air pulse volume at standard temperature and pressure (STP) (normalized by smallest). Markers with an '×' exceed our imposed volume limits. (d) Energy density composition, normalized by mass. Bars illustrate energy density is comprised of unchanging relative thermal and kinetic contributions at each reservoir pressure. The predicted volume (corresponding to mass transfer) quantified on the right axis increases with increasing P_0.

rate, a reduction by half of the length used to generate Figs. 2.2c and d (5.7 cm) yields only a 15% average increase in the energy. Practical considerations require the needle be long enough to pass through the device wall and $\gtrsim 2$ cm into the sample to minimize boundary effects.

The size of the symbols in Fig. 2.2c denotes the relative volume of the air delivered (STP). Tests that exceed the 5 mL limit are marked with an '×', demonstrating that larger needles may require a reduction in reservoir pressure to avoid over inflation. Fig. 2.2d provides the volumes generated at the largest and smallest pressures using the 178 μm needle, illustrating they are well within the volume constraint.

2.4 Device Design

Given the constraints detailed in the previous section, we design the SBC device to achieve ballistically-relevant energy densities through variable reservoir pressure, needle geometry, and high speed valve operation. The device, pictured in Figure 2.3, operates by first pressurizing the closed reservoir chamber (F). Next, a pulse of air is released through the needle (G). To do so, the externally mounted piezo-actuator (A) holds the valve stem (B) in the down/sealed position until pulse generation. During pulse generation, the actuator moves the valve stem up, unsealing at the valve seat (IVNA) and allowing air to flow though the needle.

2.4.1 Operating at High Chamber Pressure

As Fig. 2.2c illustrates, the SBC device requires high driving pressures. Minimizing specialized equipment for pressurization limits the maximum pressure to 30 MPa for readily available pumps (Table 2.1). Even at these pressures all electrical devices must remain external to the tank to mitigate risk due to sparking in an oxygen dense environment. External mounting also lessens the footprint and volume of the device, reducing the required wall thickness and material costs. A vessel volume of 60 mL ensures a negligible pressure drop during pulse release (semi-infinite reservoir). Externally mounted components access the inner chamber through a seal (α) and pass-throughs.

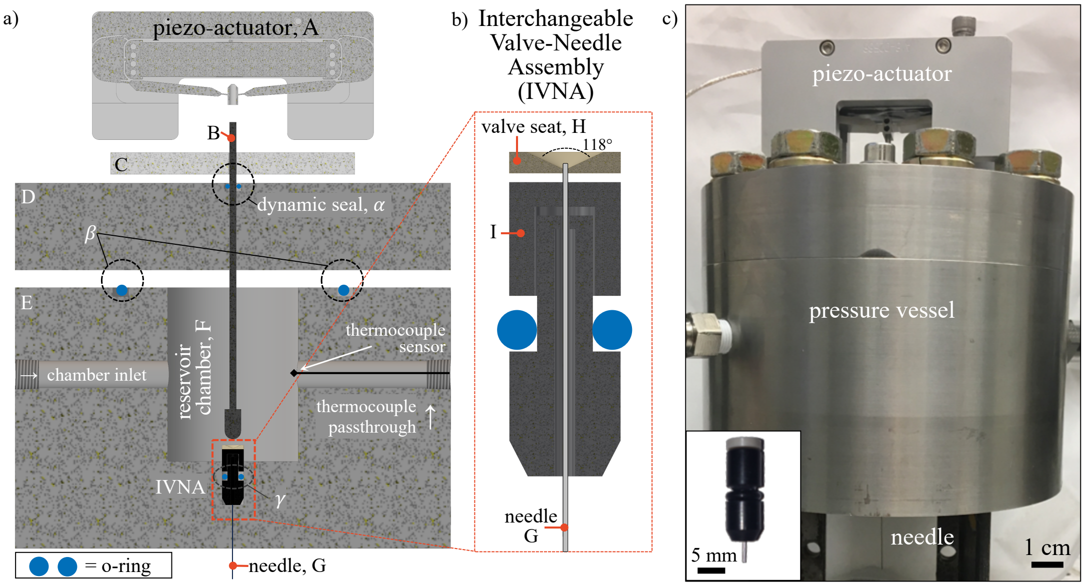

Figure 2.3 Visualization of device components. (a) An exploded cross section of the SBC device depicting the positioning of, and connections between, components. The piezo-actuator (A) drives the valve stem (B) up and down to control air flow. The lid (D) and the main chamber body (E) enclose the reservoir chamber (F), interfacing via static seal (β). An additional static seal (γ) prevents leakage around the IVNA. A dynamic seal (α) is held in place by the actuator mounting plate (C). (b) An exploded cross section of the IVNA. The valve seat (H) and main body (I) are bonded with the needle (G) to eliminate leakage (c) A photo of the device. Inset: the IVNA.

Dynamic (α) and static (β, γ) seals sustain the required pressures during valve operation. A dynamic rod seal (α) around the valve stem (B) and constrained between the actuator mounting plate (C) and the chamber lid (D) enables external actuation of the valve. The stem's small diameter (2 mm) lowers contact area, accommodating low resistance vertical travel, but is sufficiently large to resist lateral deflection. At the bottom of the device, a static radial gland seal (γ) at the Interchangeable Valve-Needle Assembly (IVNA) (Section 2.4.2) prevents leakage.

2.4.2 Varying Needle Geometry

Traditional needles and needle connections cannot withstand the large pressures required. A custom Interchangeable Valve-Needle Assembly (IVNA) enables variable needle geometry. Needles (G), constructed from blunt-tipped, high pressure hypodermic tubing are embedded within three bonded pieces assembled with an o-ring (Fig. 2.3b). The IVNA body (I) is

Component	Description	Manufacturer
Piezoelectric actuator	travel: 700 μm travel (-30 to 150 V) stiffness: 0.5 N/μm blocking force: 250 N resonant frequency: 1736 Hz	Dynamic Structures and Materials, LLC
Pressure sensor	range: 0 to 30 MPa resolution: 7 kPa	SSI Technologies (MG series)
Pump	maximum pressure: 30 MPa	Hill Pump (model MK4)

Table 2.1 List of key device components.

constructed from two pieces of epoxied polycarbonate. The two pieces that make up the body, I, should be epoxied after placing the o-ring and the epoxy should not contact the o-ring, finally this epoxy should fully set before adding the valve seat. While I is setting, the bottom of the valve seat (H) should be treated by a UVO cleaner for about 20 minutes to enhance the bonding of epoxy to the low surface energy polyether ether ketone (PEEK).[69] If the valve fails, it usually occurs at the base of the PEEK valve seat where it contacts the polycarbonate body. After UVO treatment the needle is threaded through the body and then the valve seat. Fast setting epoxy is applied to the needle and the top of I. Running the needle back and forth through I allows the epoxy to coat the needle and fill the clearance hole of the body. The valve seat is then be pressed onto the top of I, clay wrapped around the bottom of I can provide tension against the needle while positioning. A ball bearing, the same size or smaller than to be used in normal operation, is used to press the top of the needle down to an appropriate depth (so that the ball bearing clears the needle during normal valve cycling). Minimal epoxy and a tight clearance (± 0.001 in) around the valve seat pass through ensure sealing around the needle but also prevents epoxy from oozing through and potentially clogging the needle entrance. Ultimately the o-ring seals around the IVNA and epoxy seals the body of the valve leaving the valve seat as the only opening. The PEEK valve seat provides a smooth sealing surface and high stiffness for minimal elastic rebound during valve cycling. A steel sphere valve disc sharply contacts the valve seat's corner to minimize contact required to seal. The sharp corner contact is essential for minimal sealing force, a large contacting area increases the required force and stroke from the piezo actuator, which could be over matched. A shallow valve/nozzle angle (118°) reduces the vertical component of the momentum flux through the valve to reduce reaction forces on the valve stem (B) during flow.

2.4.3 High Speed Valve Control

Though fast, piezo-electric actuators have limited travel (typically $\sim$10 - 100 μm).[3] The stiffness (force) of the actuator is inversely related to the speed, requiring the valve to seal with minimal force and minimal deflection of the sealing surface as previously noted. In operation, the long (consequently heavy) valve stem decreases the actuator's resonant frequency. The stem must also resist lateral deflections that would inhibit valve seating. To accommodate these opposing constraints, a thin steel valve stem transitions to a larger aluminum hub at the end, providing a mounting point for the steel valve ball. Only a small force (at maximum pressure, $\sim$3 N) is required to break the seal because the area of the valve stem at the dynamic seal (α) is only slightly smaller than the valve's seating area on the IVNA. This provides a positive sealing force when pressurized, but is well within the actuator's limits. When the seal breaks, pressure pushes upward against the thin shaft, but the small shaft area prevents the force from exceeding operating limits.

The piezo-actuator (Table 2.1) permits 525 μm of positive travel and 175 μm of negative travel that can be utilized to seal the IVNA valve. The valve actuation trajectory tracks a 3-4-5 polynomial[70] (Figure 2.4a), which has zero acceleration and finite jerk at the beginning and end of motion, minimizing vibrations. Hysteretic properties of the actuator are mitigated by using a longer closing stroke.

2.5 Results and Discussion

Volume (mass transfer) measurements validate the ability to produce repeatable pulses of the volume predicted in § 2.3. We further illustrate the experimental control enabled by the SBC device design, validating its utility in capturing ballistically-relevant phenomena via variable-energy-density and constant-energy-density, variable-loading-rate conditions.

---

[3] Commercially available solenoidal valves were considered, but cannot reproduce sub-millisecond open and close times and usually operate at lower pressures.

2.5.1 Verification of Experimental Performance

Controlling valve open-time ensures that known mass and energy is delivered during an air pulse. The piezo-actuator input voltage specifies the actuator trajectory (light gray dashed line, Fig.2.4a); however, it must be adapted to counteract changes in forces present at different pressures that would otherwise delay or prevent valve closing. For the high speeds required by SBC, gas pressure on the valve stem affects the necessarily lower stiffness piezo-actuator. As the pressure increases, so does the force on the valve stem. We vary the amplitude ratio of the closing stroke of the voltage signal relative to the opening stroke (Fig. 2.4a), increasing this ratio for increasing pressures. We believe that both the pressure acting on the valve stem, as well as a reaction force due to higher mass flux into the valve, may result in a larger force resisting valve closing at high pressures. At high pressures, higher forces also tend to drive the valve open once a minimum separation is reached, resulting in loss of control for large maximum voltage values (i.e., larger than the overshoot in Fig. 2.4a). At low pressures, a too-low maximum voltage fails to clear the valve disc from the opening quickly enough for the rapid establishment of fully-developed flow. Thus, the required amplitude ratios and maximum voltages are empirically determined across the desired range of pressures.

Valve-stem trajectory is recorded with a high speed camera to verify timing for each desired operating pressure. Figure 2.4 illustrates valve trajectories for the extrema reservoir pressures in Fig.2.4a, 3.6 MPa and 16 MPa. We determine valve opening and closing (open and closed circles, respectively) by finding the first point that exceeds and the first point to fall below the maximum value of the baseline signal. The period between these points verifies the 5 ms valve open duration. This method assumes the time to full valve opening and closing are negligible. Audible detection of gas leakage is known to occur at valve displacements of at least 25 μm. Because opening and closing motions to this threshold account for $\lesssim$ 10% of the detectable valve movement, the approximation of deviation from baseline is sufficient. The validity of this assumption is supported by experimental measurement of the ejected air pulses.

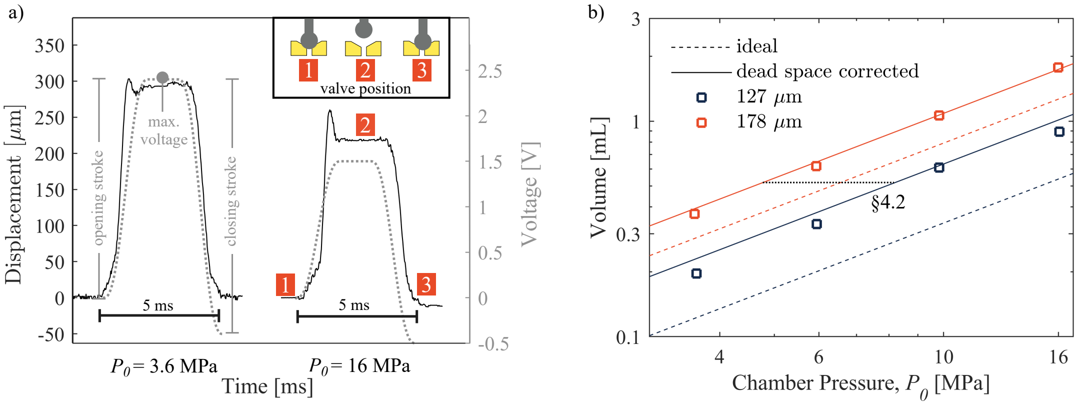

Figure 2.4 Experimental performance and validation. (a) Applied voltage signals (gray-dashed) and their corresponding measured valve trajectories at the lowest and highest operating pressures. Labels indicate the maximum input voltage, and opening and closing stroke lengths, which differ for the two pressures to overcome differing dynamic forces present at the start of flow. (b) Volumes of 5 ms air pulses from 127 and 178 μm diameter needles (blue and orange squares, respectively). The data are approximated by the idealized model from Eqn. (2.4) (dashed diagonals) and closely match the dead space corrected volume predicted in Eqn. (2.5) (solid diagonals).

To further validate valve control and the device operation model developed in § 2.3, we measure air pulses by capturing bubbles ejected into water. A graduated pipette, modified through the addition of a funnel at the tip, is filled with water and submerged next to the needle. Air ejected from the needle rises into the inverted funnel. The air bubble is then drawn up from the funnel into the pipette where volume is quickly measured using the graduated markings. We plot these measured volumes for two needle diameters in Fig. 2.4b (squares correspond to four measurements with standard error smaller than the symbol size). The linear dependence on P_0 arises from the proportionality between mass flow rate and P_0 (Eqn. (2.3)). Given the valve flow time, Δt, and assuming ideal gas behavior, the predicted volume, V_{ideal}, is

$$V_{\text{ideal}} = \frac{\dot{m} \Delta t R_{\text{air}} T_2}{p_{\text{atm}}} \tag{2.4}$$

Each measured volume is slightly larger than the predicted volume (dashed line). However, Eqn. (2.4) assumes flow stops immediately when the valve closes. In reality, a small, but finite, volume of pressurized air, V_{dead}, remains within the IVNA (a dead space). The air in the dead space escapes through the needle tip after valve closure. Though we minimize this space in the design and assembly process for the IVNA, $V_{\text{dead}} \approx 3\ \mu\text{L}$, estimated geometrically. Accounting for this behavior yields the dead-space corrected predicted volume,

$$V_{\text{corr}} = V_{\text{ideal}} + V_{\text{dead}} \frac{P_0}{P_{\text{atm}}}, \tag{2.5}$$

shown with solid lines in Fig. 2.4b. Note that no fitting parameters enter into these predictions. All quantities are experimentally determined or rely on published property data. The excellent agreement between V_{corr} and the data demonstrates SBC device control and validates the assumptions made in § 2.3.

2.5.2 Demonstration of Variable Control

Unlike existing high-speed cavitation methods, the SBC device uniquely allows for variation in experimental design based on ballistically-relevant control variable options. Although the variables of reservoir pressure, P_0; pulse time, Δt; needle diameter determine the device operation, energy density and mass transfer (analogous to final air bubble volume measured in § 2.5.1) provide more natural inputs for ballistic inquiry. Both energy density and mass transfer are determined via the relationships detailed in § 2.3, enabling the selection of either as a fixed variable while still allowing variation in the existing control variables.

We begin with an observation of the effect of energy density, which guided initial design choices. Using molded blocks of commercially available polydimethylsiloxane (PDMS, Sylgard 184) in a softer, non-standard ratio (35:1, pre-polymer to crosslinker, quasi-static Young's Modulus $\sim$ 220 kPa[4]), we perform cavitations using a 178 μm needle. As shown in Fig. 2.2c and demonstrated in the series of images in Fig. 2.1b-c, energy density increases at constant probe size (needle diameter) and Δt with increasing P_0. A higher mass flow (volume transferred) accompanies this energetic increase as indicated in Fig. 2.2c and d. The final morphology of the higher energy density test (Fig. 2.1c, $P_0 = 16$ MPa) shares qualitative similarities with observations from ballistic testing. First, the centralized region closest to the needle has a high density of cracks, decreasing to three as the distance from the needle increases. This morphology is reminiscent of the "extravasation" zone around a ballistic wound.[21] This region of tissue is created on the inner surface of the temporary cavity and coincides with increased damage and bleeding. Second, an increased energy density leads to an increased maximum temporary cavity diameter, D_{max}, similar to previous observations[66,67] (as determined from measurement of the widest part of the cavity during expansion, $D_{\text{max, 10 MPa}} = 7.4$ mm, $D_{\text{max, 16 MPa}} = 8.8$ mm). Together, these observations demonstrate the ability of SBC to replicate temporary cavities and other phenomena seen in terminal ballistics.

As illustrated in the previous example, keeping Δt constant means that in choosing a single control variable, at least two other experimental variables change. Aside from energy density, the variables of interest are probe size (needle diameter) and mass transfer. The effect of needle diameter on cavities might be used to examine materials having heterogeneous microstructural length scales, such as those encountered in biological tissue. Mass transfer, because of its relation to volume, is expected to relate to the displacement applied in creating the cavity and the final cavity volume. In some cases, anticipated effects may confound results if not accounted for. For a series of constant energy density tests where needle diameter is varied, a decrease in mass transfer accompanies a decrease in diameter. If the anticipated effect of decreasing final cavity size is ignored, smaller scale microstructural features may be misinterpreted as less stiff in reality, for example. A horizontal dashed line in Fig.2.2c (4-5 MPa range) illustrates this experimental scenario. Two parallel lines guide the eye, showing the dependence of energy density on reservoir pressure at two needle diameters. The horizontal line intersects these lines at the reservoir pressures required to generate identical energy densities. Similarly, for a series of constant mass transfer tests, needle diameter may again be varied, but increasing energy density accompanies a decrease in diameter. These experiments could explore the relative affect of probe size and final cavity volume. However the results (particularly surface area) would likely be influenced by increasing energy density, which also tends to drive cavity growth. Varying diameter at fixed mass transfer (proportional to volume at a given temperature) is illustrated by a horizontal dashed line intersecting the orange and blue lines in Fig.2.4b. Any competing responses should be addressed in the future via both simulation and experiment.

A particularly useful combination of experimental parameters arises when both energy

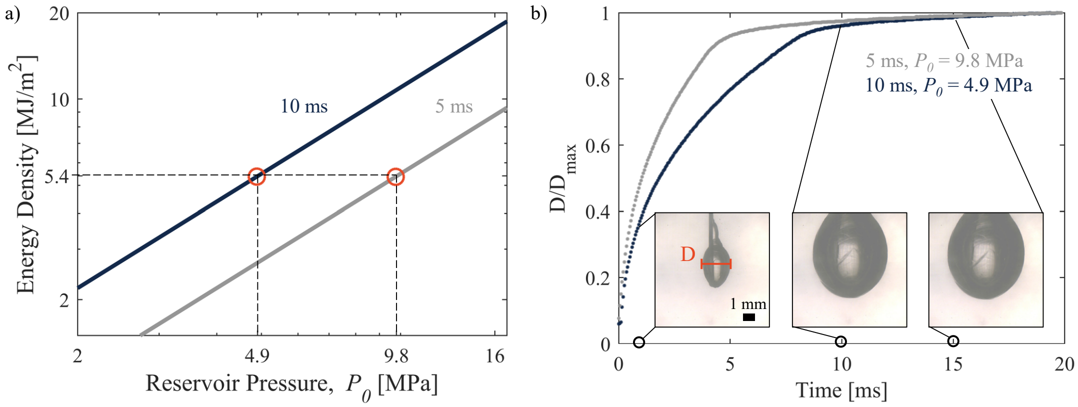

Figure 2.5 Varying rate of energy density transfer. (a) Energy density dependence on P_0 for 5 and 10 ms flow times (gray and blue lines, respectively) for a 178 μm needle. Both energy density and mass transfer (volume transfer) remain constant when multiplying flow time by a constant and dividing P_0 by the same constant. In this experiment, the 5 ms pulse is multiplied by two, requiring $\frac{P_0}{2}$. (b) The time evolution of cavity diameter at the conditions specified in (a), 5 and 10 ms (gray and blue, respectively) taken from high speed camera images. Inset: example images from the 10 ms experiment at 1, 10 and 15 ms after initiation.

density and mass transfer remain constant. This is possible through variation of Δt at fixed needle size, as illustrated in Figure. 2.5a. Given the expressions for energy density and mass flow (Eqns. (2.2) and (2.3), respectively), at identical needle diameters doubling the pulse time requires halving P_0 (from 9.8 to 4.9 MPa). The resulting tests produce different *rates* of energy density transfer. We demonstrate this effect in the same PDMS blocks. Cavitations are performed at the conditions shown in Fig. 2.5a and with the accompanying time-dependent expansion given in Fig. 2.5b (see SI for 0.002× speed videos of these tests). The high rate (5 ms, 9.8 MPa) cavity reaches 90% of D_{max} in 4.3 ms while the “low” rate (10 ms, 4.9 MPa) cavity takes 7.6 ms. When the valve closes, the cavity quickly approaches a maximum value, as evidenced by both curves and the “low” rate images at 10 and 15 ms (Fig.2.5b, inset). We observe that the “low” rate cavity reaches a 20% larger maximum diameter (2.9 mm versus 2.3 mm), suggesting that viscous effects may play a role in suppressing cavity expansion at the higher rate.

2.6 Summary and Conclusions

Building on past cavitation testing methods, but with a focus on high deformation rates, we create a Small-scale Ballistic Cavitation (SBC) device capable of delivering high energy pulses of air to soft solids via an embedded needle. To achieve high energy densities at a bench top scale, we first model the required energy transfer and mass flow to establish pressure and time scale requirements. Though these models make several idealized assumptions (ideal gas, steady-state, isentropic and frictional Fanno air flows) we show excellent experimental agreement, requiring no fit parameters, between device operation and model predictions for the delivered air pulses. The wide applicability of the SBC device to ballistically-relevant test conditions is validated with two comparisons: variable energy density and variable rate of energy density transfer (at constant total energy density and mass transferred). These tests demonstrate the ability of the device to duplicate phenomena observed in tissue and tissue simulant: temporary cavity formation and "extravasation." With its ability to be used in a lab setting, the SBC device will inexpensively facilitate the rapid generation of data capable of increasing our understanding of high-speed, soft solid failure.

2.7 Acknowledgements

The authors thank Prof. Kelly Stephani for discussions on choked flow; the Visualization Laboratory from the Beckman Institute Imaging Technology Group for use of the high speed camera; and Dynamic Structures and Materials, LLC for their helpful insight on interfacing with the piezo-actuator. Finally, we acknowledge start-up funding provided by the Mechanical Science and Engineering Department at UIUC.

2.8 Supplementary Information

2.8.1 Ballistic Energy Density

We calculate that handgun ballistic energy density ranges from 2.7 to 15 MJ/m^2. From a data set comprised of 10 handgun calibers (.22 LR to .44 Magnum), the lowest energy density was the .25 Auto and the greatest was the .44 Magnum. Energy density is determined by the round's kinetic energy at the muzzle (v: muzzle velocity, m: bullet weight) and the undeformed bullet's cross sectional area, A_0 using the expression

$$E_{\text{density}} = \frac{\frac{1}{2}mv^2}{A_0}. \tag{2.6}$$

2.8.2 Derivation of Energy Balance

We begin with a general energy balance around our transient, but stationary, control volume at the tip of the needle. This can be immediately simplified by recognizing that there is no heat flux, $\dot{Q}$, or mass flow out, $\dot{m}_{out}$ of our control volume and that potential energy is negligible.

$$\frac{\mathrm{d}U}{\mathrm{d}t} = \cancel{\dot{Q}} - \dot{W}_{pV} + \dot{m}_2 \left(h_2 + \cancel{\rho_2 z_2} + \frac{v_2^2}{2} \right) - \cancel{\dot{m}}_{out} \left(h_{out} + \cancel{pz_{out}} + \frac{v_{out}^2}{2} \right). \tag{2.7}$$

U is the internal energy of the system, and $\dot{m}$, h, ρ, z, and v are mass flow rate, enthalpy, density, height, and velocity with 2 referring to the properties at the needle tip and 'out' a hypothetical output stream. We then integrate with respect to time such that

$$\int dU dt = -\int \dot{W}_{pV} dt + \int \dot{m}_2 \left(h_2 + \frac{v_2^2}{2} \right) dt. \tag{2.8}$$

The work done by the system on the surrounding material is, $W_{pV} = \int \dot{W}_{pV} dt$. Steady-state flow from the reservoir through the duct make $\dot{m}_2$, h_2, and v_2 time-independent and $\dot{m}_2$ is simply $\dot{m}$ throughout the flow path. Therefore,

$$W_{pV} = U_0 - U_f + \dot{m}\Delta t \left(h_2 + \frac{v_2^2}{2} \right), \tag{2.9}$$

where U_f and U_0 refer to the final and initial internal energy states, respectively, and Δt is the pulse time. Because the system starts with no mass and therefore no energy, $U_0 = 0$. A switch to specific internal energy, $U_f = m_f u_f$ and recognizing that a mass balance gives

$m_f = \dot{m}\Delta t$, Eqn. (2.9) becomes

$$W_{pV} = m_f u_f - \cancel{m_0} u_0 = \dot{m}\Delta t \left(h_2 - u_f + \frac{v_2^2}{2} \right). \tag{2.10}$$

By definition, $u_f = h_f - P_f \underline{\mathrm{v}}_f$, where P_f and $\underline{\mathrm{v}}_f$ refer to the pressure and specific volume of the control volume after the pulse is complete. Thus,

$$W_{pV} = \dot{m}\Delta t \left(h_2 - \left(h_f - P_f \underline{\mathrm{v}}_f \right) + \frac{v_2^2}{2} \right). \tag{2.11}$$

Assuming ideal gas properties for the air makes enthalpy a function of temperature only and $P\underline{\mathrm{v}} = RT$. Combined with a constant specific heat approximation, c_p, Eqn. (2.11) becomes

$$W_{pV} = \dot{m}\Delta t \left(c_p \left(T_2 - T_f \right) + RT_f + \frac{v_2^2}{2} \right). \tag{2.12}$$

At this point, we must make an assumption about the final state of the control volume. By taking the final state as the barely expanded bubble of stagnant air, $T_f = T_2$, resulting in,

$$W_{pV} = \dot{m}\Delta t \left(RT_2 + \frac{v_2^2}{2} \right). \tag{2.13}$$

This is a lower estimate for the work done by the control volume on the test material.

2.8.3 Flow Equations

Flow through the IVNA is treated as compressible.[71] First isentropic flow takes the air from stagnant in the reservoir (position 0) through a nozzle that interfaces with the needle at position 1 (Figure 2). This is followed by Fanno flow through the needle, to the outlet at position 2. The properties of the air at the needle inlet (position 1) and outlet (position 2) are established relative to the reservoir (position 0).

Fanno Flow:

Working backward from the needle exit (position 2) under the assumption that flow at the outlet is choked, the Mach number at position 1, M_1, is given by the expression[71]

$$\frac{4fL}{D} = \frac{1-M_1^2}{\gamma M_1^2} + \frac{\gamma+1}{2\gamma} \ln\left[\frac{(\gamma+1)M_1^2}{2+(\gamma-1)M_1^2}\right], \tag{2.14}$$

where L, D, γ, and f are needle length, diameter, ratio of specific heats, and Fanning friction factor, respectively.

Given the Mach number at position 1, the pressure and temperature ratios across the needle are given by the following Fanno flow relations[71]:

$$\frac{P_1}{P_2} = \frac{1}{M_1}\sqrt{\frac{\gamma+1}{2\left(1+\frac{\gamma-1}{2}M_1^2\right)}}, \tag{2.15}$$

$$\frac{T_1}{T_2} = \frac{\gamma+1}{2\left(1+\frac{\gamma-1}{2}M_1^2\right)}. \tag{2.16}$$

At this point, the Mach number is known at positions 1 and 2, but only the relative states of the air at those positions (T_1, P_1 and T_2, P_2) are known.

Isentropic Flow:

Given M_1, the pressure and temperature ratios across the isentropic nozzle can be calculated using isentropic flow relations[71]:

$$\frac{P_1}{P_0} = \left(1+\frac{\gamma-1}{2}M_1^2\right)^{\frac{-\gamma}{\gamma-1}}, \tag{2.17}$$

$$\frac{T_1}{T_0} = \left(1+\frac{\gamma-1}{2}M_1^2\right)^{-1}. \tag{2.18}$$

The state of the reservoir, P_0 and T_0 are known before an experiment begins. Using Eqns. (2.15)-(2.18), to work forward through the system determines the states of the air at positions 1 and 2. The Mach number and state at any position is sufficient to determine the mass flow through the IVNA according to Eqn. (3).

2.8.4 Fanning Friction Factor

The Fanning friction factor, f, is key in determining the air's acceleration within the needle, but requires the state of the air through the needle because it is a function of the Reynolds number, Re

$$Re = \frac{\bar{u}D}{\bar{\nu}}. \tag{2.19}$$

$\bar{u}$ is the average air velocity and $\bar{\nu}$ is the average kinematic viscosity and primarily a function of T. Average values are calculated using the beginning (position 1) and end (position 2) state of air. Thus for each needle geometry, f must be solved for iteratively.

The iterative procedure to determine f begins with an assumed value of 0.005, an approximate value for stainless steel. The Fanning friction factor is related to the Darcy friction factor, f_D, via $f = f_D/4$, which in turn is related to Re via the Swamee-Jain equation[72]

$$f_D = \frac{0.25}{\left[\log_{10}\left(\frac{\varepsilon/D}{3.7}\right) + \frac{5.74}{Re^{0.9}}\right]^2}, \tag{2.20}$$

where ε/D is the diameter-normalized (relative) roughness ε. The initial guess therefore enables a calculation of 'guessed' state of the air as an average over the needle, via the Reynolds number. The state calculated using Eqns. (2.15)-(2.18) can be compared with the 'guess state.' If the states do not agree, the calculated state is taken as the new 'guess state' and Eqn. (2.20) is used to determine f. The cycle is repeated until the difference between the 'guess' and the calculated states agree is less than 1×10^{-5}.

The roughness is measured using an optical profilometer (Keyence VK-X1000). Oblique slices across the needle exposed the interior. The arithmetical mean roughness (Ra) was measured from an average of five lines along the needle's main axis (in the direction of flow). Using the profilometer's software, we determined a value of $\varepsilon = 0.77 \pm 0.1$ μm.

2.8.5 Device Sealing Details

The dynamic rod seal is comprised of a small, stiff, and well lubricated o-ring surrounding the stem (B) and is confined under the actuator mounting plate (C) (Fig. 3). A static seal (β) between the lid and the main chamber body provides manual access to the inner chamber (F); a thermocouple pass-through (E, right) monitors the air temperature within the chamber; and pressurization and pressure monitoring occurs via a fixed inlet (E, left). A three-way valve facilitates pressurization by switching between either the pump or a bleed valve. Once pressurized, the valve isolates the chamber. The valve seat (H) and needle tubing (G) must be simultaneously positioned and bonded to the main valve body (I) in order to seal the narrow space around the tubing while minimizing dead space within the valve.

Chapter 3

Multi-crack formation in soft solids during high rate cavity expansion

3.1 Overview

Using the SBC device and similar pneumatic cavitation techniques, we investigate the parameters governing initiation of localized deformation in high-rate spherical expansions to develop a theory of fracture observed in these cavities. This theory allows for quantification of a soft solid's fracture energy by examination of the fractured surface. The parameters governing failure in ultra-soft solids can be difficult to quantify since traditional characterization techniques often cannot be used. The effects of increasing rate further complicate efforts. However soft solids, especially biological tissues, are frequently subjected to high rate deformation leading to damage and failure. We present results from high rate, needle-mediated cavity expansions in soft silicone and ballistic gelatin samples with moduli on the order of 10 kPa. We find that increasing rate of expansion increases the number of cracks initiated in the cavity surface, leading to multi-lobed as opposed to penny-shaped cracked cavities. Comparison of these experimental observations with an elastic wave speed-dependent fracture correlation model originally developed for hard materials suggests that counting the number of cracks may provide a measure of the soft solid's fracture energy.

3.2 Introduction

Qualitative observation of ballistic wounding in soft tissue indicates that the degree of damage depends strongly on tissue properties and projectile size, type, and velocity.[20,21,66–68,73] For example, impacts on brittle tissues like the liver and spleen are damaged to a greater degree than tougher, more stretchable tissues like muscle or lung.[21,66,67,73,74] But projectile effects are primarily tested on only a few formulations of synthetic simulants, *e.g.*, ballistic gels, and frequently those projectiles are chosen from commercially available ammunition rather than for controlled variation of size, type, and velocity.[62,68] As a result, the fundamental dependence of damage in soft materials and tissues as a function of these parameters remains unknown.

Ballistic impacts in soft solids generate short-lived cavities larger than the size of the projectile when kinetic energy transfers radially from the projectile path. A debate exists between the existence of any significant damage caused by these 'temporary cavities'[66,73] and the other extreme in which temporary cavity size directly relates to ammunition effectiveness.[75] If no damage or fracture were to occur during this deformation, the material stretch in these temporary cavities would reach magnitudes on the order of ten. Such stretches without damage and failure are unprecedented for the ballistic simulants used and therefore we anticipate fracture at some point during the expansion. As has been observed quasi-statically, the extent of damage accumulated during temporary cavitation likely depends on material properties[76] and expansion rate.[77]

A multiplicity of radial cracks accompanies the expansion of these terminal ballistic cavities at high rates, however, existing damage analysis methods are notably limited in application and generalizability. Quantification includes post-mortem measurement of the number of cracks formed, their lengths, and the area enclosed by cracks.[21,24,32,62,68,78] However, correlation between these values and projectile energy is only found if the same projectile type is used [See[62,68] and references therein] since by design, some bullets may yaw or tumble while others deform.[20,62,66,68] This variability affects the local kinetic energy transfer rate along the projectile path. Thus, in addition to the dynamic rates involved, non-uniformity in applied deformation complicates experiments. Further, typical post-mortem analysis can be insensitive to crack initiation since as they grow, cracks can branch or become subsumed by larger cracks nearby, making comparison between different materials at different rates challenging.

To combat some of these challenges, we employ a Small-scale Ballistic Cavitation (SBC) device, in which cavities are inflated by releasing pressurized air in a controlled pulse

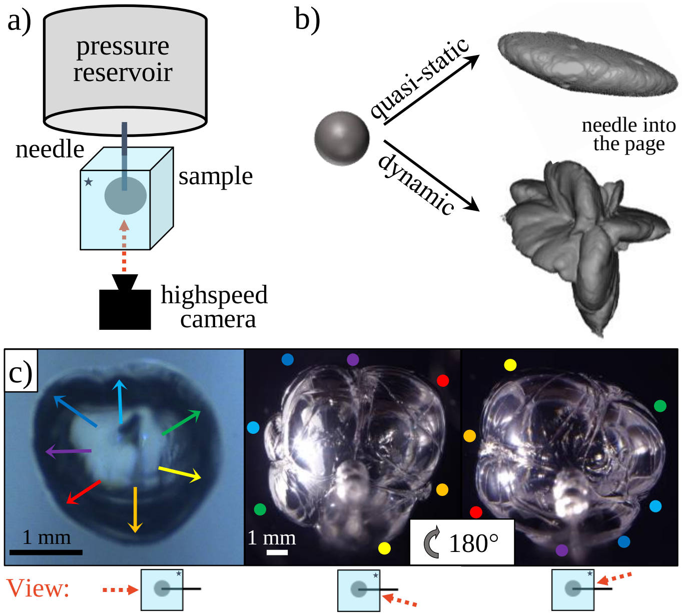

Figure 3.1 Overview of experimental setup and representative results. (a) The SBC device[25] generates cavities at high rates via an embedded needle. (b) When viewed along the needle axis, 3D reconstructions from CT scans of cavitations in 40:1$_{10\%}$ silicone show that quasi-static expansions generally produce penny-shaped cracks, while high rate expansions generate multiple crack lobes. (c) A high-speed image at early expansion times (left, bottom view) with cracks (colored arrows) at initiation grows to form a lobed sample at intermediate times (20 s) after the pulse (middle and right images). Corresponding cracks from two angles are indicated by colored dots.

through a needle embedded within a soft solid.[25] We maintain ballistic rates and a deformation mode typical of temporary cavities, but projectile variation effects are eliminated. Because the device localizes the expansion using an embedded needle, cracks predominantly grow radially outward with the line defining the crack tip being parallel to the needle axes. This alignment of fracture by the needle axis combined with a single, local expansion allows for characterization via a single, magnified viewpoint that is not possible in traditional terminal ballistics. The simplified, spherical cavity geometry also lends itself to approximate analytical modeling, as opposed to prior efforts to replicate total cavitation morphology using finite element simulation [*e.g.*,[31,79]].

Our aim is to provide a framework for beginning to understand the relative importance of rate, material properties, and characteristic size in the development of fracture morphology under conditions mimicking ballistically-induced cavitation. The single-cavity expansion geometry enables the application of a classic dynamic fragmentation theory.[45,46,48,80,81] This theory postulates that the number of fragments/fractures arises from a total system Griffith-like energy exchange constrained by an elastic-wave-speed-dependent correlation length scale over which cracks can interact. The model predicts increases in the number of cracks formed for increasing expansion rate (under most conditions), greater cavity size, and decreasing fracture energy when all other parameters remain constant. Unlike the traditional high modulus structural materials[82–84] for which this theory was originally developed, soft materials have a lower elastic wave speed, are highly rate dependent, and are often capable of finite deformations. We find that the latter does not affect our interpretation of the experimental data reported here. However, reduced elastic wave speed produces a multiplicity of cracks at even moderately high expansion velocities (~ 1 m/s). Failure to consider the rate dependence of modulus is unphysical when values can vary by more than an order of magnitude and, we find, provides a poorer description of the experimental observations.

To make comparisons between a elastic-wave-speed-governed crack density and high-speed cavitation morphology, we begin by adapting the theory for the density of cracks formed under ballistic loading conditions in hard materials. Guided by this model, we perform a series of ballistic-rate cavity expansions on soft materials of controlled formulation using the SBC device. The results from SBC are further extended through a modified cavity expansion device that enables the use of large needle sizes. We successfully interpret the size-dependent cavitation morphology using the simplified theoretical model.

3.3 Crack Formation at High Rates

In a series of articles, Grady[45,46,48,80,81] postulated a model for length scales resulting from dynamic fragmentation of an elastic body by combining Griffith-type fracture criteria with an elastic wave speed-dependent correlation horizon between cracks. Here, we explore the predictions resulting from these assumptions when applied to dynamically expanding cavities in soft solids.

Grady's correlation horizon is the distance at which two cracks can elastically-interact

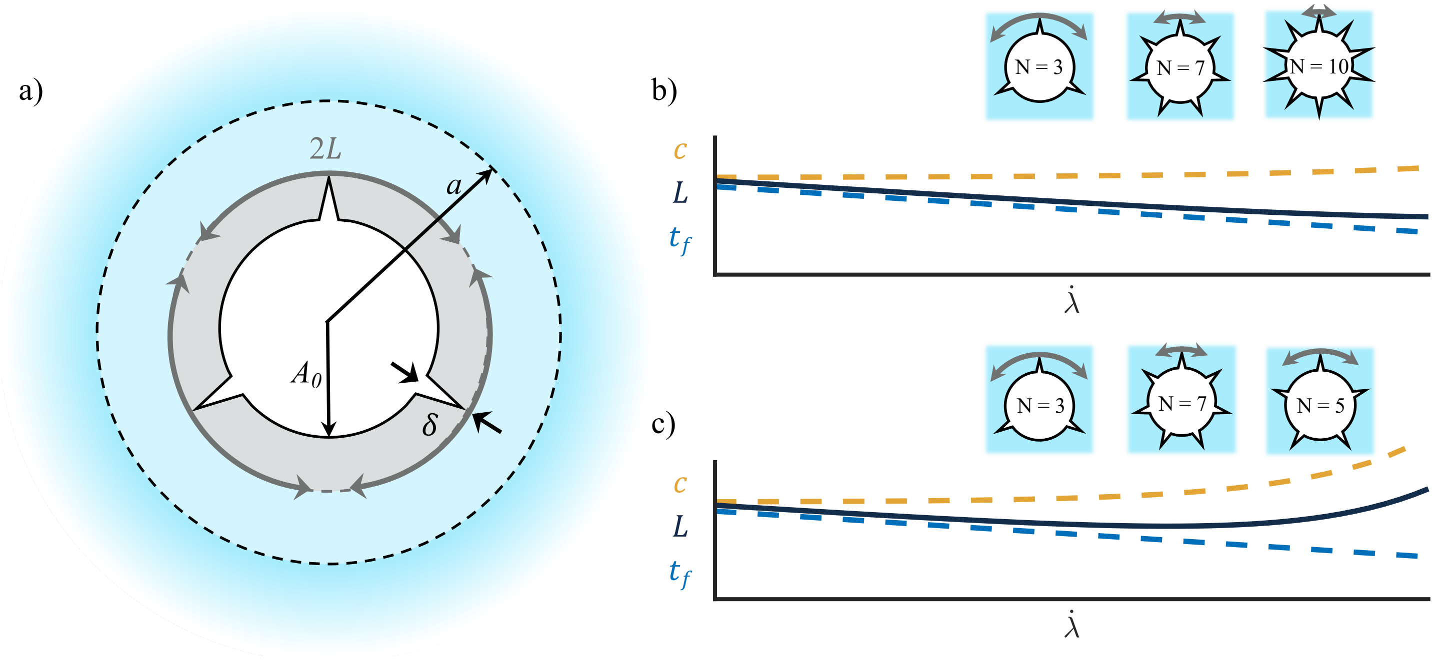

Figure 3.2 Cavity schematic and effect of material rate dependence on crack formation. (a) An undeformed cavity of radius A_0 expands to a size, a, denoted by the dotted line. Initial radius changes by a crack length, δ, when fracture occurs as indicated by the gray shaded area. (b) In materials with low or no strain rate sensitivity, the number of cracks initiated always increases with expansion rate due to the monotonic decrease of correlation length, L. (c) In materials exhibiting significant stiffening with increasing strain rate, the number of cracks may decrease at a threshold strain rate due to the non-monotonic behavior in L. $L = ct_f$.

at a dynamically expanding surface undergoing failure. This distance, L, is given by the elastic wave speed multiplied by the time available for travel of an elastic wave, *i.e.*, as an upper bound, the time of dynamic expansion until the onset of failure, t_f. It follows that the number of cracks predicted for a 2-D ring can be approximated by the circumference of the ring divided by $2L$ (since cracks propagate in both directions, see Figure 3.2). Experimental observations detailed in Section 5.3 find that, when viewed from the bottom, cracks propagate radially out from the needle. Thus, similarly to a 2-D ring, the number of cracks in a cavity of would be approximately the cavity circumference divided by $2L$. In the limit of the small deformations that accompany low relative fracture energies, the cavity circumference at failure is well approximated by the initial circumference, $2\pi A_0$, so that

$$N = \frac{2\pi A_0}{2L} = \frac{2\pi A_0}{2ct_f}, \tag{3.1}$$

where A_0 is the initial, undeformed cavity radius (on the order of the needle diameter.[5] See Figure 3.2. The time-to-failure, t_f, is a function of λ_f and the speed at which the cavity wall is expanding, V, where, $\lambda_f = a/A_0$, the relative deformation at fracture, arises from the Griffith fracture criteria in the following paragraph. Defining a pseudo 'strain-rate' for the cavity expansion, $\dot{\lambda} = V/A_0$ we can express t_f as,

$$t_f = (a - A_0)/V = \frac{\lambda_f - 1}{\dot{\lambda}}. \tag{3.2}$$

For linear elastic materials, the shear wave speed, c, is given by $\sqrt{\mu/\rho}$, where μ is the shear modulus and ρ is the density. Combining Eqns (4.1) and (4.2) provides a prediction for the number of cracks during the high speed expansion of a cavity in a soft solid,

$$N = \pi \frac{\dot{\lambda} A_0}{\sqrt{\mu/\rho}} \underbrace{\frac{1}{\lambda_f - 1}}_{f(\Gamma/\mu A_0)}. \tag{3.3}$$

$\dot{\lambda}$, A_0, ρ, and μ form one dimensionless group that governs crack number. λ_f depends on the onset of fracture, which we show in the next section is a function of $\Gamma/(\mu A_0)$, where Γ

is an effective fracture energy. As can be seen from Eqn. 4.3, N is linear in $\dot{\lambda} A_0/\sqrt{\mu/\rho}$ (or alternatively $V/\sqrt{\mu/\rho}$) and in general a non-linear function of $\Gamma/(\mu A_0)$. We wish to note here that we considered the effect of finite deformations on the model proposed here, but find that for our experimental data, stretch at fracture is always predicted to occur at a value of less than 1.5 for which linear models using the initial cavity diameter and neo-Hookean models using the deformed cavity diameter are practically identical. For simplicity, we treat only the linear deformation case here and leave exploration of the effects of non-linearity to future work.

Following a Griffith treatment, fracture occurs when the energy required to create a new surface due to growth of a crack by an infinitesimal length, δ, is equal to the elastic energy released during that same growth.[85] For a spherical cavity, this derivation has been discussed by multiple authors[3,86–88] so we will provide only a brief treatment. For the simplest case of a so-called 'spherical crack,' the energy released when a cavity in the undeformed configuration grows from an initial radius of A_0 to a new radius of $A = A_0 + \delta$ is given by

$$\Delta U_F = \Gamma(4\pi A^2 - 4\pi A_0^2) \approx 8\pi\Gamma A_0 \delta, \tag{3.4}$$

to first order in δ. The elastic energy, U_E, corresponding to the expansion of a cavity of initial radius A' to a deformed radius of a within an infinite, incompressible, neo-Hookean medium is given by Zhu, et al.[89]. Here, we model the linear elastic energy of the solid by using only the first order term of neo-Hookean expression determined upon taking the difference, ΔU_E,

$$\Delta U_E = U_E(a,A) - U_E(a,A_0) = U_E(a,A_0+\delta) - U_E(a,A_0), \tag{3.5}$$

in the elastic energy between a cavity expanded from an initial radius of A_0 and a fractured cavity having a radius $A_0 + \delta$. Keeping only the terms that are first order in δ yields

$$\Delta U_E(a/A_0) \approx 16\pi A_0^2 \mu (a/A_0 - 1)\delta. \tag{3.6}$$

Equating the energy changes per crack length, $\Delta U/\delta$, we determine cavity deformation at fracture, $\lambda_f = a/A_0$, where a is the deformed radius at fracture.

$$\lambda_f = \frac{1}{2}\frac{\Gamma}{\mu A_0} + 1 \tag{3.7}$$

Combining Eqns (4.3) and (4.2) leads to predictions for the correlation horizon,

$$L = \frac{1}{2\dot{\lambda}}\sqrt{\frac{\mu}{\rho}}\frac{\Gamma}{\mu A_0} \tag{3.8}$$

and the number of cracks formed,

$$N = \pi\frac{\dot{\lambda}A_0}{\sqrt{\mu/\rho}}\left(\frac{1}{2}\frac{\Gamma}{\mu A_0}\right)^{-1}. \tag{3.9}$$

It is important to note that the modulus value, μ used in Eqns. (3.8) and 3.9 is the shear modulus of the material *at the rate of expansion*. Unlike traditional high modulus structural materials, soft materials are highly rate dependent and, as shown in Fig. 3.3, their moduli can vary by several orders of magnitude as opposed to the nearly strain-rate independent elastic moduli values observed in metals and ceramics.[82–84] When predicting the number of cracks that will occur using a material's quasi-static modulus, μ_0, complications arise that require care in the application of Eqn. 3.9. The strain dependence of N is no longer apparently linear. Strain-rate-dependent modulus, μ, appears within both the $\dot{\lambda}A_0/\sqrt{\mu/\rho}$ and $\Gamma/(\mu A_0)$ terms. Fracture energy likely varies with strain rate as well and we discuss two possible limits using a scaling argument for the fracture energy, $\Gamma \sim \Gamma_0(\mu(\dot{\lambda})/\mu_0)^n$, where Γ_0 is the quasi-static fracture parameter. If the Γ scales linearly with the modulus ($n = 1$) as is the typical trend in Ashby-type plots,[90,91] then $\Gamma/(\mu A_0)$ remains unchanged with rate and $N \sim \dot{\lambda}[\mu(\dot{\lambda})]^{-1/2}$ (*i.e.*, $\Gamma/(\mu A_0) = \Gamma_0/(\mu_0 A_0)$). In some instances the scaling can be reduced to as low as, $\Gamma \sim \mu^{1/2}$ ($n = 1/2$), in which case the linear strain rate dependence is restored, $N \sim \dot{\lambda}$, but μ and $\Gamma/(\mu A_0)$ in Eqn. (3.9) are replaced by μ_0 and $\Gamma_0/(\mu_0 A_0)$, respectively. Here we typically assume that the linear scaling, $n = 1$, is the case unless otherwise stated, as it appears to be the more common relation.

As a result of the linear scaling between Γ and μ, strain rate dependence of crack number can exhibit a maximum whose location varies with A_0 and the strength of the modulus strain rate dependence. As Figure 3.3b shows for a projectile-sized initial cavity ($A_0 = 0.5$ cm), the high strain rate dependence of ballistic gelatin (orange curves) exhibit a maximum around 10^5 1/s. This non-monotonic behavior is due to increasing correlation length accompanying the rapidly increasing wave speed associated with the sharp increase in modulus with increasing strain rate and is illustrated schematically in Figure 3.2. The strain rate at which the peak occurs increases with increasing A_0 and thus only becomes possible at very high strain rates and/or for macro scale expansions. For the experimental parameters we report below, we would anticipate monotonically increasing N with $\dot{\lambda}$.

Given the limited strain rate data available, we turn to the normalized fits of the gelatin and PDMS data shown in Fig. 3.3a (see caption for details) to approximately account for strain-rate dependence when fitting our experimental data to the above model. Employing the form,

$$\mu = \mu_0 \tilde{\mu}(\dot{\lambda}), \tag{3.10}$$

where $\tilde{\mu}$ is a dimensionless function of $\dot{\lambda}$, we obtain a quasi-experimental strain rate dependence. The modulus in the quasi-static limit, μ_0, of the fits in Fig. 3.3a is replaced with the experimentally determined quasi-static modulus for a given formulation. See Section 5.3 for further discussion of these results.

3.4 Methods and Materials

3.4.1 Sample Preparation

PDMS and PDMS-oil PDMS and PDMS-oil samples are prepared as by Yang, et al.[76] Sylgard 184 [Dow Corning] pre-polymer and crosslinker are mixed in ratios of 30:1, 35:1, 40:1, 45:1, and 50:1. Diluted samples include an additional step of adding 10-35% 350 cSt silicone oil before mixing again. Samples cure in 4.1 × 4.1 × 5.1 cm (85 mL) transparent rectangular boxes at room temperature for 6 days, with testing on day 6.

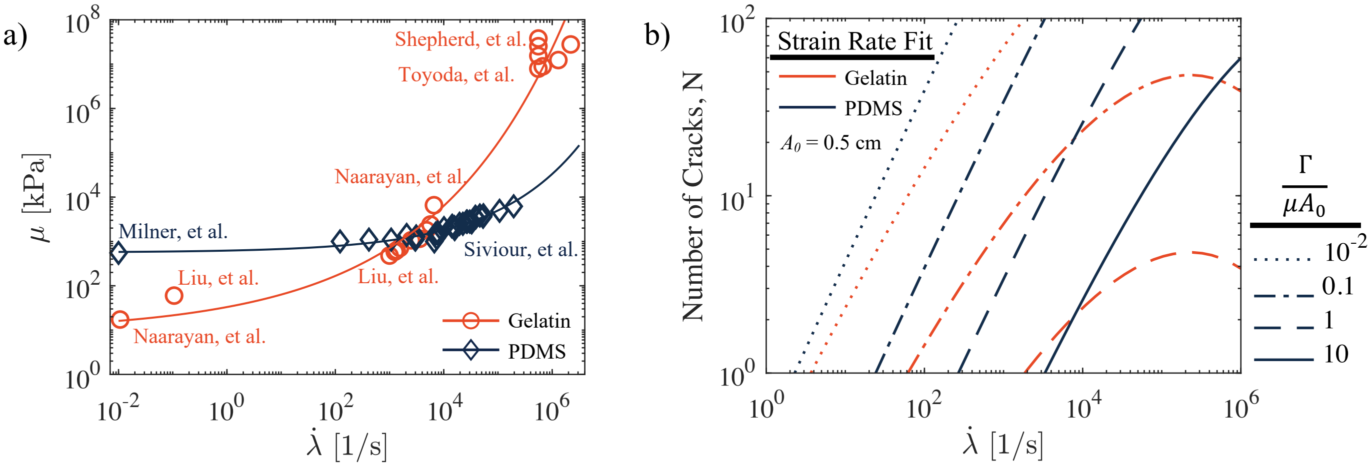

Figure 3.3 Material strain rate dependence. a) A collection of modulus data for ballistic gelatin[33,34,37,38] and PDMS (Sylgard 184) (dark blue)[25,39] at rates ranging from quasi-static to 10^6 1/s. Fits of the form $\mu = \mu_0 \exp\left[q_1 \dot{\lambda}^{q_2}\right]$ are shown using solid curves. (Gelatin: $\mu_0 = 9.1$ kPa, $q_1 = 1.294$, $q_2 = 0.176$; PDMS: $\mu_0 = 560$ kPa, $q_1 = 0.096$, $q_2 = 0.212$, where $\dot{\lambda}$ is in units of 1/s.] b) An example of the potential effect of strain rate dependent modulus on N using Gelatin and PDMS data from (a) as inputs to Eqn. (3.9) for an initial cavity radius $A_0 = 0.5$ cm. $\Gamma/(\mu A_0)$ (equivalently $\Gamma_0/(\mu_0 A_0)$ since $n = 1$) is varied over four orders of magnitude from 10^{-2} (dotted lines) to 10 (solid lines, not shown for Gelatin since N does not exceed one under these conditions). ($\rho = 10^3$ kg/m^3)

Ballistic Gelatin Ballistic gelatin preparation follows the detailed standardization method from Jussila,[92] where half of the required water is heated to 70°C and the other half remains room temperature (20°C). The entire amount of gelatin powder is mixed into the room temperature water until the solution is uniform and allowed to swell for at least two minutes before the heated water is added to the solution, which equilibrates to 45°C. This temperature is maintained and stirred to dissolve all gelatin. The solution is cooled at 5°C for 48 hours in the same molds as the PDMS.

3.4.2 High-Rate Cavity Expansion Procedure

Small-scale Ballistic Cavitation The Small-Scale Ballistic Cavitation (SBC) device generates cavities using a 356 μm diameter, blunt-tipped needle. Growing cavities are captured with 2× magnification and high-speed imaging (25,000 fps) from the bottom of the sample along the needle axis through a transparent sample stage. High resolution images of the final fractured geometry are obtained using a macro lens.

PDMS and PDMS-oil samples SBC testing begins by inserting the needle at a rate of 0.5 mm/s until the needle tip is approximately 2.5 cm into the sample, then retracting the tip 2 mm before allowing the deformation to relax for 10 min. An SBC reservoir pressure and valve cycle time of 8 MPa and 3.8 ms, respectively, are used for all tests.[25] Intermediate and long-time cavity images are gathered immediately after the test from the top of the sample at an angle of about 15 degrees from the needle axis. To do so, the stage is first lowered at 20 mm/s to extract the needle. The first intermediate time image of the cavity is captured within 20 s of the air pulse and four sides of the cavity (rotating 90 degrees along needle axis) are imaged within one minute. Long-time images are taken at 6 min after the air pulse, again from four sides.

Gelatin samples begin by inserting the needle at a rate of 5 mm/s. The needle penetrates the sample at least 2 cm before it is retracted 2 mm and then allowed to rest at least 30 s. The reservoir pressure is set to 4, 8, or 16 MPa and the valve cycle time is 5 ms. Pressurized air within the gelatin escapes immediately upon needle removal, therefore cavity morphology is imaged only during the high-rate expansion.

Meso-scale Ballistic Cavitation Cavity formation using larger needles (>635 μm diameter) requires an alternative device. This device (SI Figure 3.12) is comprised of two ball valves connected together to make a small chamber between them. The chamber is filled by opening one valve that is connected to a pump. An interchangeable passthrough attached to the other valve accommodates different tubing sizes. We use 991 μm and 1575 μm diameter tubes as blunt-tipped needles. To perform a test, the valve (1) nearest the pump is opened and the line is pressurized to 6.9 MPa, while the other valve (2) remains closed. Valve 1 is then closed, sealing air in the space between the valves. A pulse of air is delivered by opening valve 2, releasing the pressurized air stored between the valves. For these tests, needle insertion is performed at the same rate as in SBC, but the 991 μm and 1575 μm needles are retracted 4 and 6 mm, respectively, to maintain a similar order of magnitude between needle diameter and retraction distance. High speed images are captured along the needle axis as in the SBC tests.

3.4.3 Image Processing

Initial Cavity Expansion Rate An ellipse fitting procedure (ImageJ) identifies cavities from high-speed images taken concurrent with the applied air pulse duration. Fits are spot-checked manually. We plot the average of the ellipse fit axes at each time point and perform linear fit of the cavity size versus time to determine the initial wall velocity.

Crack Processing Cracks initiated within the expanding cavity are counted manually; the process is validated by comparing results between two independent observers. Crack tips are identified by the presence of 'corners' along the cavity edge or when corners are not present (typically when cracks number two to four) circles are manually fit around suspected crack tips to estimate the number of cracks. Crack identification is performed when the cavity is at an expansion ratio of 7, when the number of observed cracks is stable. Expansion ratio is determined from the ellipse fit normalized by needle radius. Examples of crack identification are shown in Figure 3.6a and in the SI.

3.5 Experimental Results and Discussion

3.5.1 Overview of Experimental Results

We expand cavities at high speeds in soft solids using pressurized air (>4 MPa) released through an embedded needle. Visual inspection of the post-mortem cavities finds that crack 'lobes' orient parallel to the needle axis. Thus, crack tips, biased by the needle, primarily grow radially outward from the needle and can be characterized from a view along the needle axis. We leverage this feature to monitor the high-speed crack growth early in the expansion process.

We quantify the high rate of expansion using high speed imaging. Representative data from the average of the axes of a best-fit ellipse to a 2-D image of the cavity from the bottom view (along the needle axis) versus time are shown in Figure 3.4. Cavity wall velocity, V, is determined from a linear fit of the 'radius' from 0.05 to 0.3 ms. We found that wall velocity varies little with changes in the oil concentration (*i.e.*, at constant modulus) as noted by the orange and dark blue square in Fig. 3.4. Changing the needle size has a greater effect on wall velocity since a constant pressure reservoir is used and air moves much more rapidly through the smaller needles (Light orange and blue graded points, Fig. 3.4).

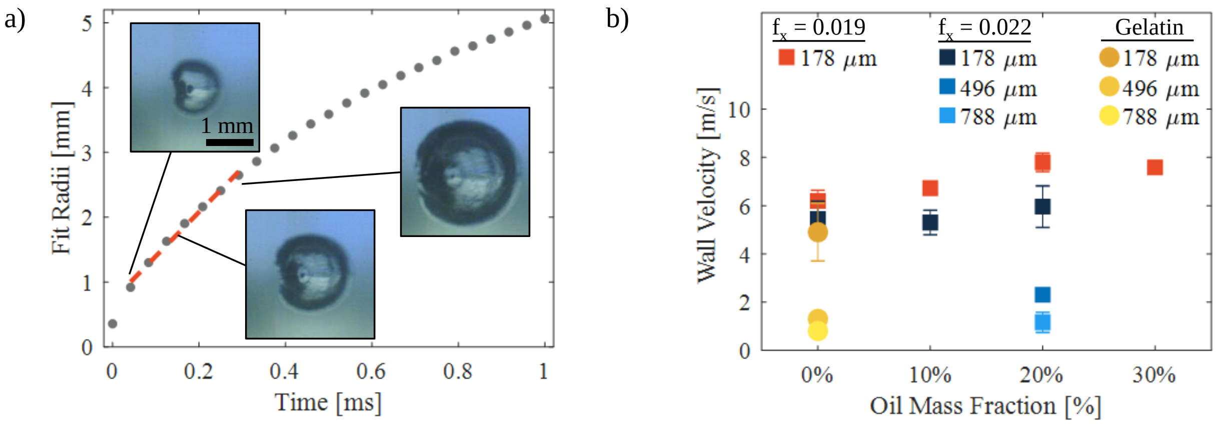

Figure 3.4 Cavity wall velocity. a) Approximate cavity diameter versus time (points) early during the air pulse-driven expansion. Wall velocity is obtained from a linear fit of the region shown (dashed line). Select representative images within this region are shown for context. b) Wall velocity versus oil percentage for both the silicone (orange and blue squares) and ballistic gelatin (yellow circles) materials. Rates obtained using larger needle sizes are indicated with decreasing color saturation for 20% silicone oil (dark blue to light blue) and ballistic gelatin (light orange to yellow). Error bars are the standard deviation from 5 or more samples.

Like the temporary cavities formed in terminal ballistics, air pulses drive cavities to large expansion ratios, Λ, defined approximately as the cube root of the final volume over the initial volume. As a first order estimate, we define the expansion ratio as cavity 'radius' normalized by the needle outer radius. Using the SBC device, the apparent Λ typically approaches 10-30. However, only under conditions of large $\Gamma/(\mu A_0)$, not anticipated here, is the expansion ratio expected to reach values larger than 1.5 without fracture. For the applied expansion rates we attain, a stretch of 1.5 typically occurs before the first frame of the high speed video. Visual analysis of cavities viewed along the axis of the needle within the pulse time reveal localized deviations from circularity. We interpret these deviations as crack tip formation and growth and find that the multiplicity of cracks formed aligns well with the proposed theory.

3.5.2 Evolution of Cavity Morphology

We divide discussion of the cavity fracture morphology into three approximate timescales: during pulse delivery ($\sim$ ms), intermediate times ($\sim$ s), and long times ($\sim$ min). Crack initiation occurs very soon after pulse initiation as indicated by localized deviations in the expanding cavity surface which, over time, grow into clearly defined crack lobes that occasionally combine or branch as illustrated in the time-lapse images of Figure 3.5a. After about 6 min, the cavity shapes in all but the 0% oil formulations have stopped evolving and reach a final morphology that typically exhibits multiple crack lobes.

During the pulse we anticipate that cracks initiated at or near the point of fracture have sufficient time to form and become visually apparent. In validation of this assumption, cracks are counted from randomly ordered images at three needle sizes and for the highest and lowest oil percentage formulations. (Random ordering avoids pattern matching that might occur in the analysis of sequenced images). As Figure 3.5b illustrates, the number of cracks reaches a plateau in all cases starting at $\Lambda = 7$ for the smallest needle and around $\Lambda = 5$ for the larger two needles. Because the plateau for the larger needles is maintained through $\Lambda = 7$, all PDMS and PDMS-oil cavities are analyzed for cracks at the same stretch, $\Lambda = 7$. (See Section 3.4.3 for more details.) All following comparisons to and use of the crack prediction model use cavities analyzed at $\Lambda = 7$.

Previous quasi-static cavitation experiments on identical materials[76] found that for materials having the same modulus, higher oil concentrations produced more brittle materials. Modulus is fixed by keeping the mass fraction of crosslinker constant while variation in the oil concentration and cross-linker to pre-polymer ratio are varied. For 'constant' modulus formulations cavitated at high speed and using the same needle size, A_0, we would therefore anticipate a decreasing $\Gamma/(\mu A_0)$ for an increasing oil concentration. Eqn. 3.9 predicts an increase in N as Figure 3.6 illustrates.

At the end of the pulse, approximately 3.8 ms, all cavities are roughly spherical (Fig. 3.5). Pressurized air trapped within the cavity changes this morphology which is mediated by both crack growth dynamics and viscoelasticity. Initiated cracks appear to have several

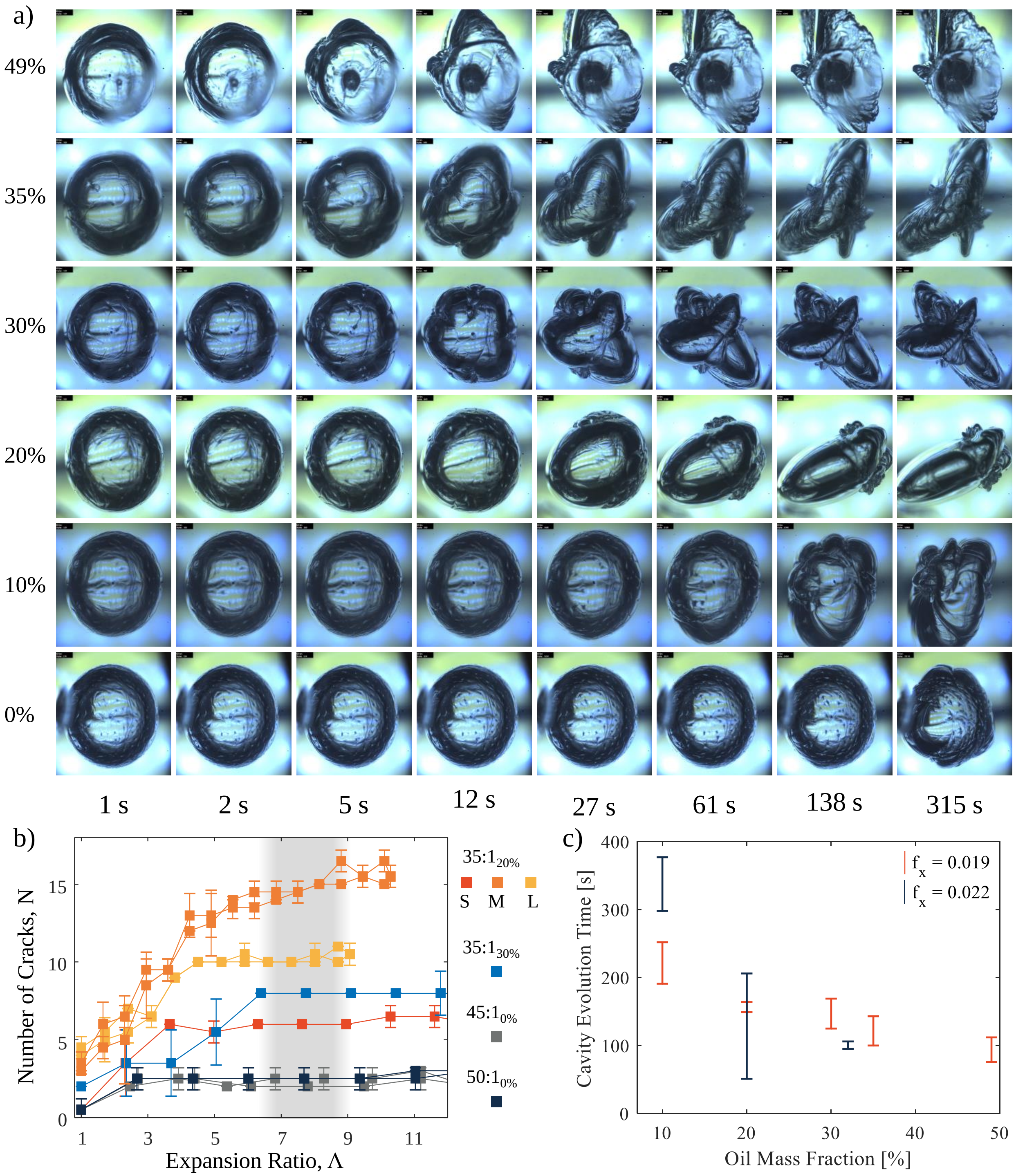

Figure 3.5 Cavity crack evolution. (a) Timelapse images (logarithmic scale) of cavities in samples of decreasing oil fraction ($f_x = 0.019$). (b) Crack counts versus time for both mass fractions at the highest and lowest countable oil fraction formulations for $f_x = 0.019$ (35:1$_{30\%}$ and 50:1$_{0\%}$) and $f_x = 0.022$ (35:1$_{20\%}$ and 40:1$_{0\%}$). Crack counts for different needle sizes (small (S), medium (M), and large (L)) are shown. c) Range of the end point of cavity evolution as a function of oil mass fraction.

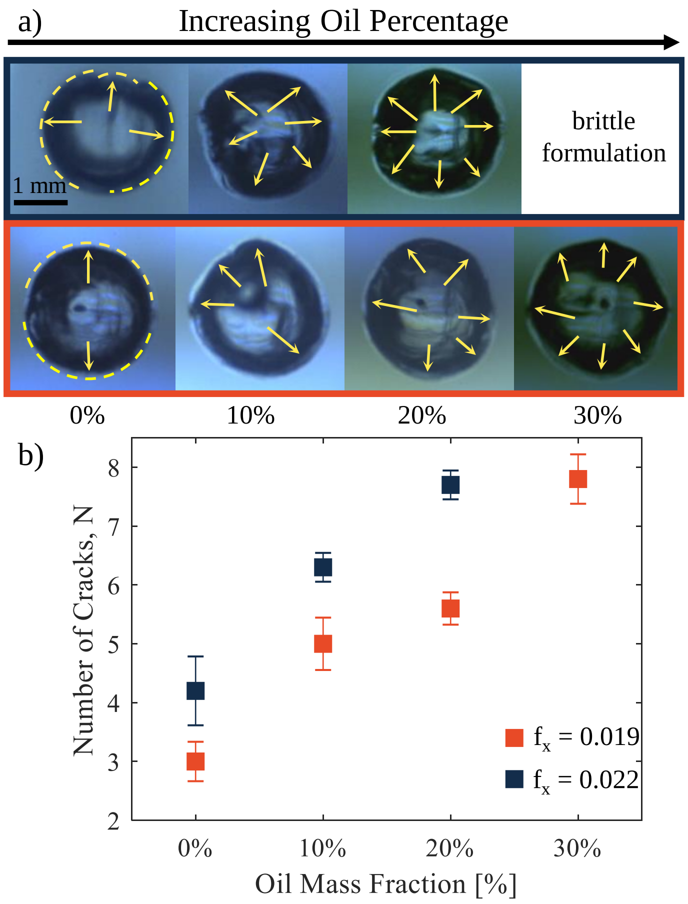

Figure 3.6 Crack number dependence on fracture behavior. a) Representative images from crosslinker mass fractions of f_x = 0.022 (top) and f_x = 0.019 (bottom) show how crack tips are visually identified. Constant f_x corresponds to constant modulus, while oil percentage varies the fracture response. More oil leads to reduced toughness. b) The number of cracks counted in each silicon formulation versus oil mass fraction (decreasing toughness). Error bars correspond to the standard deviation of 5 or more samples.

fates: they can continue to grow in their original trajectory, they can be subsumed by larger nearby cracks, they can merge with nearby cracks, or they can stop growing because nearby cracks have reduced their elastic driving force. The complex interactions of these post-initiation cracks which lead to the post-mortem cavity morphologies observed at the right of Figs. 3.5a and in Figs. 3.7 and 3.8 are beyond the scope of the predictions in section 3.3, however we make several observations that are consistent with the anticipated behavior of the silicone formulations used.

The rate of evolution toward the final, post-mortem shape for a material of a given modulus depends on its fracture energy and viscous response. Tougher materials (having a lower oil concentration and correspondingly higher loss modulus[77] remain spherical for longer during the post-pulse cavity growth phase (Fig. 3.5a - bottom row). Conversely, more brittle, higher oil-concentration formulations form crack lobes faster (Fig. 3.5a - top row). These observations are quantified in Fig. 3.5c which is obtained by using a noise threshold of differences between images at adjacent time points. The lower value is the first crossing of the threshold and the upper is the final time the difference falls below the threshold. To demonstrate the reproducibility of the observed crack morphologies, Figures 3.7 and 3.8 display high resolution images of the cavities at 20 s and 6 min after pulse initiation for four representative samples at each silicone formulation tested.[1] In both figures, one observes sharper and more pronounced lobes as one progresses down the figure. At 20 s (Fig. 3.7), we clearly see the effect of formulation on the rate of cavity morphology evolution. In these high-resolution images, multiple striations in the cavity surface (low oil concentrations) indicate the presence of crack tips, consistent with the idea that the cracks themselves are initiated early. Growth however is mediated by the viscous response of the material.

At long times, the cavity reaches its final shape as shown in Fig. 3.8. Major crack lobes are clearly visible and typically number from two to eight depending on the material formulation. More crack lobes are apparent in the formulations with higher oil percentage. In these formulations, lobes tend to be longer and narrower than the low oil percentage formulations, which have shorter lobe lengths and blunter crack tips. The final equilibrium cavity morphology for all expansions performed at high speed differs from that performed resulting from quasi-static expansions in the silicone materials we used. At high rates, cavities exhibit multiple lobes in the fractured state as opposed to penny-shaped cavities.[76] (One exception is the 50:1 formulation, the toughest and softest used, which maintains a blob-like shape at both rates due to the highly blunted crack tips that form.) Although the number of lobes does not directly correlate with the number of cracks observed at initi-

---

[1] See SI for complete data set.

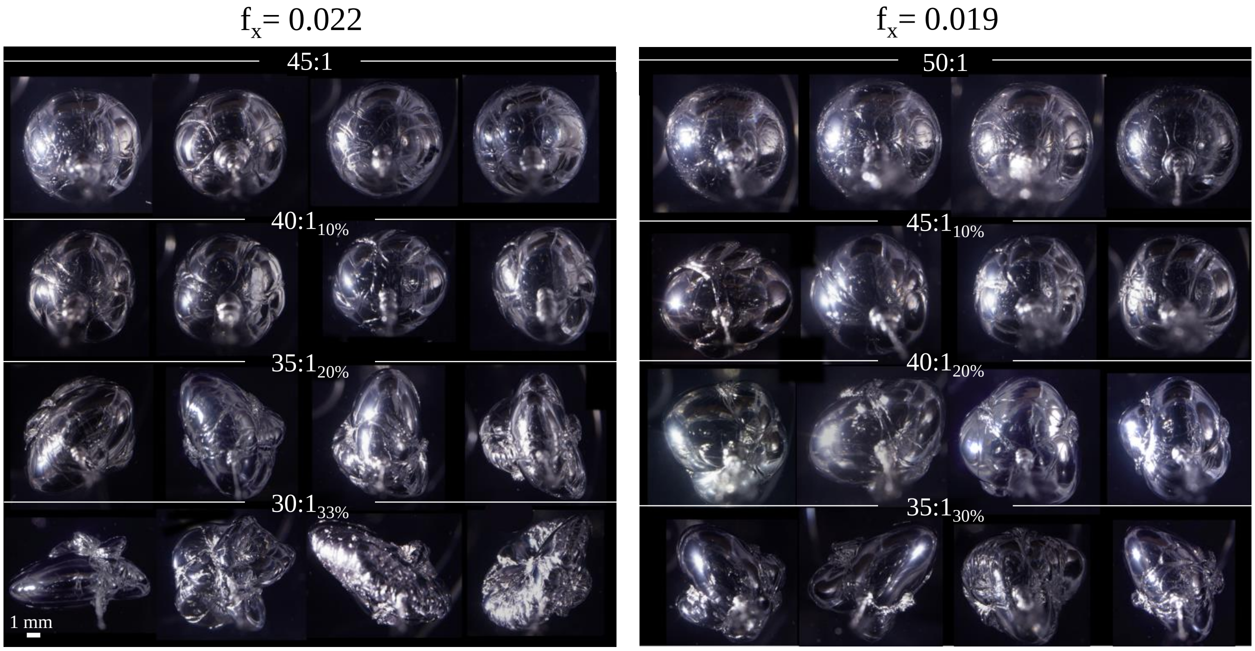

Figure 3.7 Intermediate time-scale cavity morphology. Optical images of cavities from four samples at each oil mass fraction composition from the two crosslinker mass fractions tested ($f_x = 0.022$, left, and $f_x = 0.019$, right) show that higher oil content leads to earlier lobe formation. Cavities are within 10-20 s of pulse initiation.

ation (Fig. 3.6), high speed cavitation appears to produce enough crack tips to facilitate propagation in several radial directions from the needle.

3.5.3 Relating Number of Cracks to Fracture Energy

To use the predictive model in Section 3.3 for extracting material properties, we need quantitative validation of its applicability. After observing the first evidence given by an increase in number of cavity lobes formed at high rates as opposed to the previous quasi-static experiments,[76] we chose to explore the size-dependence predicted in Eqn. 4.3. For sufficiently high wall velocity, increasing needle size should produce more cracks if correlation length rather than geometric similarity governs their formation. Furthermore, since only a handful of cracks are typically visible at the smallest needle size used, decreasing cavity wall velocity by lowering the reservoir pressure provides less experimental range for exploration.

In Figure 3.9a, representative crack initiation images for the three needle sizes (178 μm,

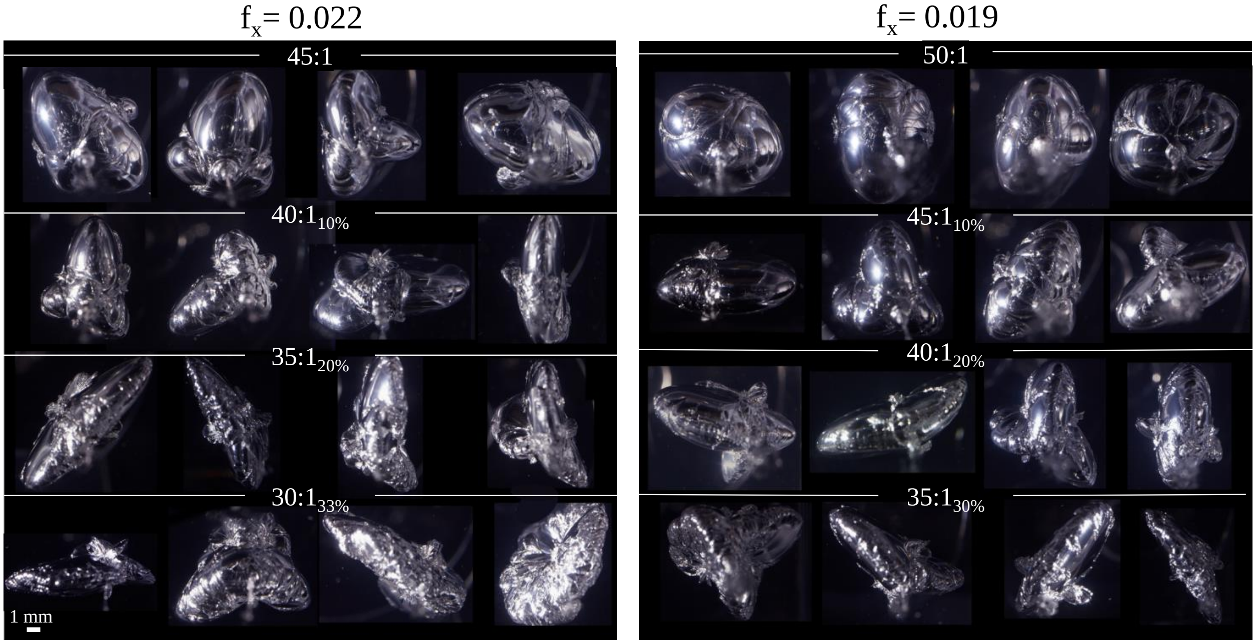

Figure 3.8 Final cavity morphology. Optical images of cavities from four samples at each oil mass fraction composition from the two crosslinker mass fractions tested ($f_x = 0.022$, left, and $f_x = 0.019$, right) illustrate more and more pronounced crack lobe formation within increasing oil content. Cavities are approximately 6 min after pulse initiation.

496 μm, and 788 μm) illustrate the trend of decreasing number of cracks with decreasing needle radius approximately. Figure 3.9b plots the experimentally determined number of cracks (squares) for the three needle sizes and provides the accompanying theoretical predictions (lines) for the accompanying wall velocity, V. A single fit value $\Gamma_0 = 0.6$ J/m2, where Γ_0 is the quasi-static modulus, brings all three theoretical predictions into alignment with the data. (We use the strain rate dependence of Sylgard 184 from Figure 3.3a, but scaled so that the initial modulus corresponds with the $35{:}1_{20\%}$ formulation PDMS formulation used as shown in Eqn. 3.10. μ_0 = 3.3 kPa.)[2] Taking the strain rate dependence of the modulus into account and using the assumption of linear scaling between Γ and μ ($n = 1$), $\Gamma = 2.9$, 1.5, and 1.2 J/m^2 at wall velocities of 5.6, 2.3, and 1.2 m/s, respectively ($\dot{\lambda} = 3.1 \times 10^4$, 4.6×10^3, and 1.5×10^3 1/s).

---

[2] Fitting was performed using all combinations of $n = 1$, 0.5 and both the PDMS and Gelatin strain rate dependencies. The fit value reported is the best by an order of magnitude according to the sum of the square of the differences (SSD).

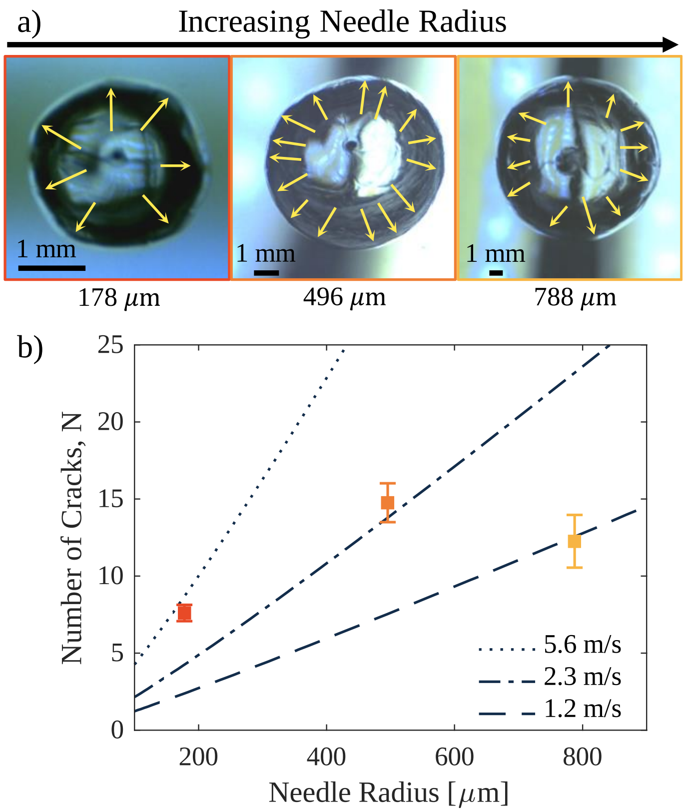

Figure 3.9 Cavitations performed in 35:1$_{20\%}$ silicone for three needle sizes yield a $\Gamma_0 = 0.6$ J/m^2 when fit to the correlation length model. a) Representative images of the expanding cavities at the three needle radii. b) The fit model (three lines) for the measured expansion rates at each needle size shows good agreement with the experimental values (squares). (Needle sizes and measured wall velocities: 178 μm, 5.6±1.4 m/s; 496 μm, 2.3±0.3 m/s; 788 μm, 1.2±0.4 m/s.)

This estimate for an effective, quasi-static fracture energy value is somewhat low when compared with related quasi-static work. The fracture energy of a similar, diluted-PDMS material system[77] having on average an order of magnitude larger modulus was found to be around 100 J/m^2. Similarly, for cavity-cracks induced by fluid injected via embedded needles,[5] effective fracture energies of 25 - 250 J/m^2 were reported for shear moduli of 25 - 246 kPa. These results suggest that an effective fracture energy of $\sim$ 3 J/m^2 might be more reasonable for the $\mu = 3.3$ kPa materials in Figure 3.3. One possibility for the discrepancy might be the definition of the initial cavity radius. In their work on volume-controlled, quasi-static needle expansion, Raayai-Ardakani, et al. suggest that the initial cavity radius that results from needle insertion is actually a factor of 3-4 times higher than the needle outer diameter.[5] Additionally, we performed 2, 4, and 6 mm extractions of the 178, 496, and 788 μm needles after insertion, following recent work by Barney, et al.,[93] which would further increase our initial cavity size. Using the needle extraction values as an upper limit for the initial cavity radii yields $\Gamma_0 = 7$ J/m^2 and $\Gamma = 16$, 12, and 10 J/m^2 at wall velocities of 5.6, 2.3, and 1.2 m/s, respectively ($\dot{\lambda} = 2.8 \times 10^3$, 5.8×10^2, and 1.9×10^2 1/s). The quality of the fit was reduced by an order of magnitude as determined by SSD. We conclude that before the quantitative values can be definitively stated, further study into the effect of the needle insertion and needle radius on the number of cracks produced is needed.

As reported in the previous section, more cracks initiate at the cavity surface as the material's toughness is reduced for a constant modulus formulation. This finding holds for sets of data taken at two sets of formulations in which the crosslinker mass fraction, $f_x = 0.019$ and 0.022, is held constant ($\mu_0 = 6.5$ kPa and 11.5 kPa, respectively). Wall velocity is considered constant for each set, 6.9 ± 1.0 m/s and 5.6 ± 1.4 m/s, because the model is not sensitive to the variation observed, *i.e.*, N changes by a fractional amount. Rearranging Eqn. (3.9) and determining μ via Eqn. (3.10), we obtain Γ (and Γ_0) for each formulation. These results are shown in Figure 3.10a.

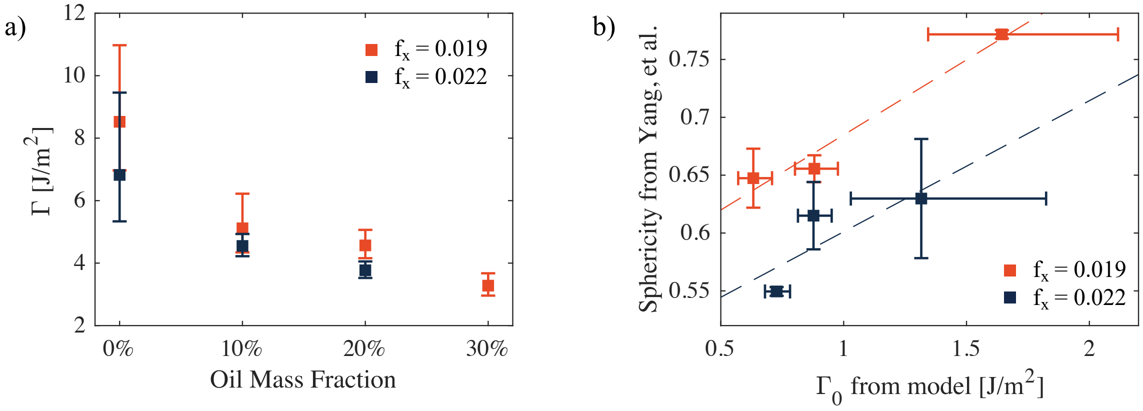

Figure 3.10 Fracture energy predictions. a) Fracture energy as a function of oil mass fraction at $V = 6.25$ m/s (the average wall velocity) for cross linker mass fractions, f_x = 0.019 (dark blue squares) and 0.022 (orange squares). Error bars arise from fits made using the standard deviation of the observed crack number, N. b) A comparison of the quasi-static fracture energy, Γ_0 with crack sphericity of identical silicone formulations obtained from previous quasi-static cavitation results.[76]

To provide some context for the trend in these results, we compare to previous quasi-static findings on this identical material system.[76] In that work, formulations with identical moduli (or equivalently mass fraction of cross-linker) but decreasing oil content were found to have increasing sphericity of the penny-shaped cracks. This increasing sphericity was interpreted to correspond to higher fracture energy, consistent with the findings in Mrozek, et al.[77] Sphericity arises from a balance between the elastic modulus (increasing modulus lowers sphericity) and the fracture energy (increasing fracture energy increases the sphericity). Thus for materials having the same sphericity, but different moduli, the higher moduli material should exhibit a higher fracture energy. Figure 3.10b illustrates this shift to higher Γ using two linear fits of the sphericity versus Γ values at lower (orange) and higher (dark blue) moduli.

When the most brittle materials are tested, crack *lobes* form in orientations other than parallel with the needle appear (*i.e.*, propagating radially outward perpendicular to the needle axis). Examples of this crack formation can be found in the SI Figure3.20. In addition to being uncountable from the bottom view, non-parallel cracks obscure the observation of other cracks. Thus, the technique we present here applies to a limited range of material behaviors, with brittle materials failing to conform to the geometry required for observation and tougher materials producing only a penny-shaped crack.

We observed one example of the latter limitation when performing tests on 20% ballistic gelatin. These materials always produce penny-shaped cracks, which we categorize here as having two cracks (SI Figure 3.24). Only in lower modulus and less tough 10% ballistic gelatin formulations were 3 cracks observed.

This observation held for cavitation pressures of 4, 8, and 16 MPa using the SBC device (producing wall velocities from 1.7 ± 0.1 m/s, 2.2 ± 0.4 m/s, and 4.9 ± 1.2 m/s, respectively). In the ballistic gelatin, all of these cavities produce three crack lobes in the final state (SI Figure 3.21). Crack branching and merging were nearly absent, potentially due to the low number of cracks formed or material behavior (gelatin is less viscous) or both. Applying the same needle-size-variation approach used for the silicone formulations (Figure 3.11), we determine a quasi-static fracture energy of the 10% ballistic gelatin of 0.3 J/m^2. As in the silicone formulation, this value is low relative to other measurements of fracture energy at quasistatic rates which can range from 1.1 J/m^2[94] to 6.8 J/m^2.[95] The same issues relating to the definition of initial cavity size apply here as well. Nevertheless, the replication of the size-dependence in crack number for another material system provides further evidence for the proposed model.

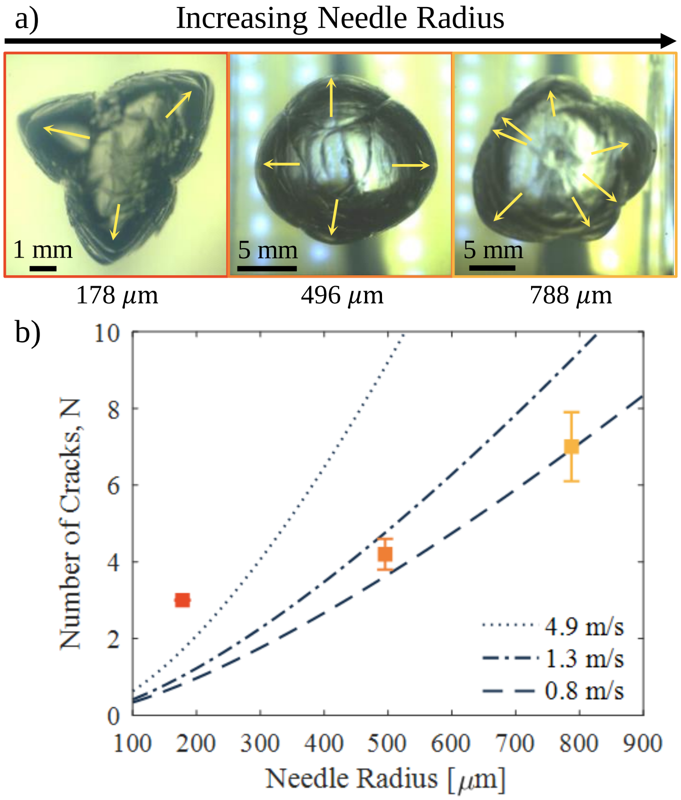

Figure 3.11 Cavitations performed in 10% ballistic gelatin for three needle sizes yield a $\Gamma_0 = 0.3$ J/m^2 when fit to the correlation length model. a) Representative images of the expanding cavities at the three needle radii. b) The fit model (three lines) for the measured expansion rates at each needle size shows good agreement with the experimental values (squares). (Needle sizes and measured wall velocities: 178 μm, 4.9±1.2 m/s; 496 μm, 1.3±0.2 m/s; 788 μm, 0.8±0.2 m/s.)

3.6 Conclusion

Adopting previous work by Grady and Kipp[45,46,48] and Grady,[80,81] we have provided evidence for an acoustoelastic-wave-speed-determined fracture correlation length scale in soft solids at moderately high deformation velocities using cavity expansion. We use a simplified model to establish the onset of failure using a balance of elastic and surface energy (Griffith criteria), with the correlation length then determining the number of cracks created at failure onset. Combined, these elements describe the observed variation in cracks formed early in the cavity expansion process in two materials systems at high rates: silicone+oil and ballistic gelatin.

Soft solids possess several unique features that make their failure at high rate unique from that of hard materials. The first is the the rate at which considerations of the acoustoelastic-wave-speed become important. Material wave speed in soft materials ranges from 1 – 10 m/s, but in typical structural materials is on the order of 1000 m/s. This means that correlation length considerations become important at much lower deformation velocities. We have shown that the damage morphology resulting from moderately high rates of expansion in cavities are qualitatively similar to the fragmentation observed at much higher rates in hard materials.[81] An approximate linear material failure model finds good agreement between fracture responses for experiments performed at different length scales and at different rates. Variations in predicted fracture energy, though somewhat low, replicate trends observed in similar material systems under quasi-static conditions.[76,77] Second, our model predicts that the strain rate sensitivity of moduli in soft materials may produce a non-monotonic dependence of the length scale governing fracture as a function of strain rate, a feature that is not possible for hard materials that have rate-independent moduli. More broadly, the morphological differences we observe in cavities expanded at different rates and having different formulations (material properties) suggest that simulated damage assessment using existing tissue-mimicking materials likely reflects only a few behaviors observed in soft tissues and that direct experimental comparison is needed.

3.7 Acknowledgements

The authors thank the Visualization Laboratory from the Beckman Institute Imaging Technology Group for use of the high speed camera and Microscopy Suite and the MicroCT. We acknowledge start-up funding provided by the Mechanical Science and Engineering Depart-

ment at UIUC.

3.8 Supplementary Information

In this supplementary material we have attempted to provide a complete set of the samples used to support the conclusions drawn in the main articles. High speed images of the silicon formulations used are shown in Figures 3.17-3.18 (for different formulations), 3.19 (for different needle sizes), and 3.20 (for very brittle samples). High resolution images of intermediate and final cavity morphology are shown in Figures 3.13-3.14 and Figures 3.15-3.16, respectively. High speed cavitation images in gelatin are provided in Figures 3.21-3.24.

The mesoscale ballistic cavitation device used to perform large needle cavity expansions is illustrated by a schematic in Figure 3.12.

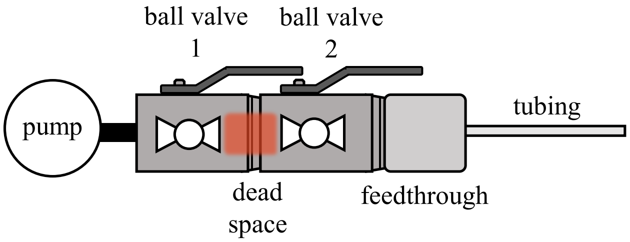

Figure 3.12 Mesoscale ballistic cavitation device. Valve (1) nearest the pump is initially opened so that the line can be pressurized, while the other valve (2) remains closed. Valve 1 is then closed, sealing air in the space between the valves (orange, 'dead space'). A pulse of air is delivered by opening valve 2, releasing the pressurized air through a tubing 'needle' mounted to an interchangeable passthrough.

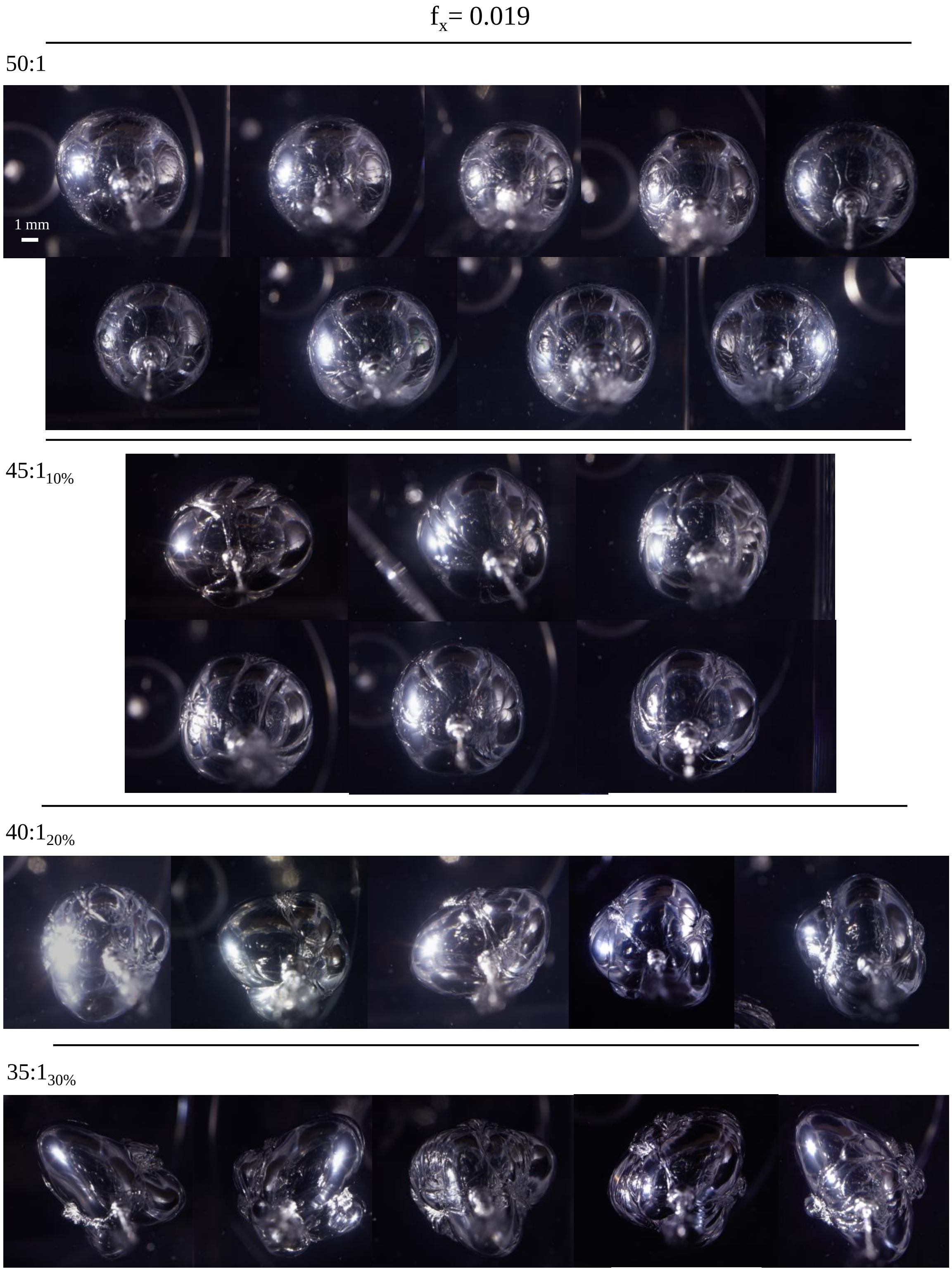

Figure 3.13 Intermediate time-scale cavity morphology. Optical images of cavities in silicone (crosslinker mass fraction, $f_x = 0.019$). Higher oil content leads to earlier lobe formation. Cavities are within 10-20 s of pulse initiation.

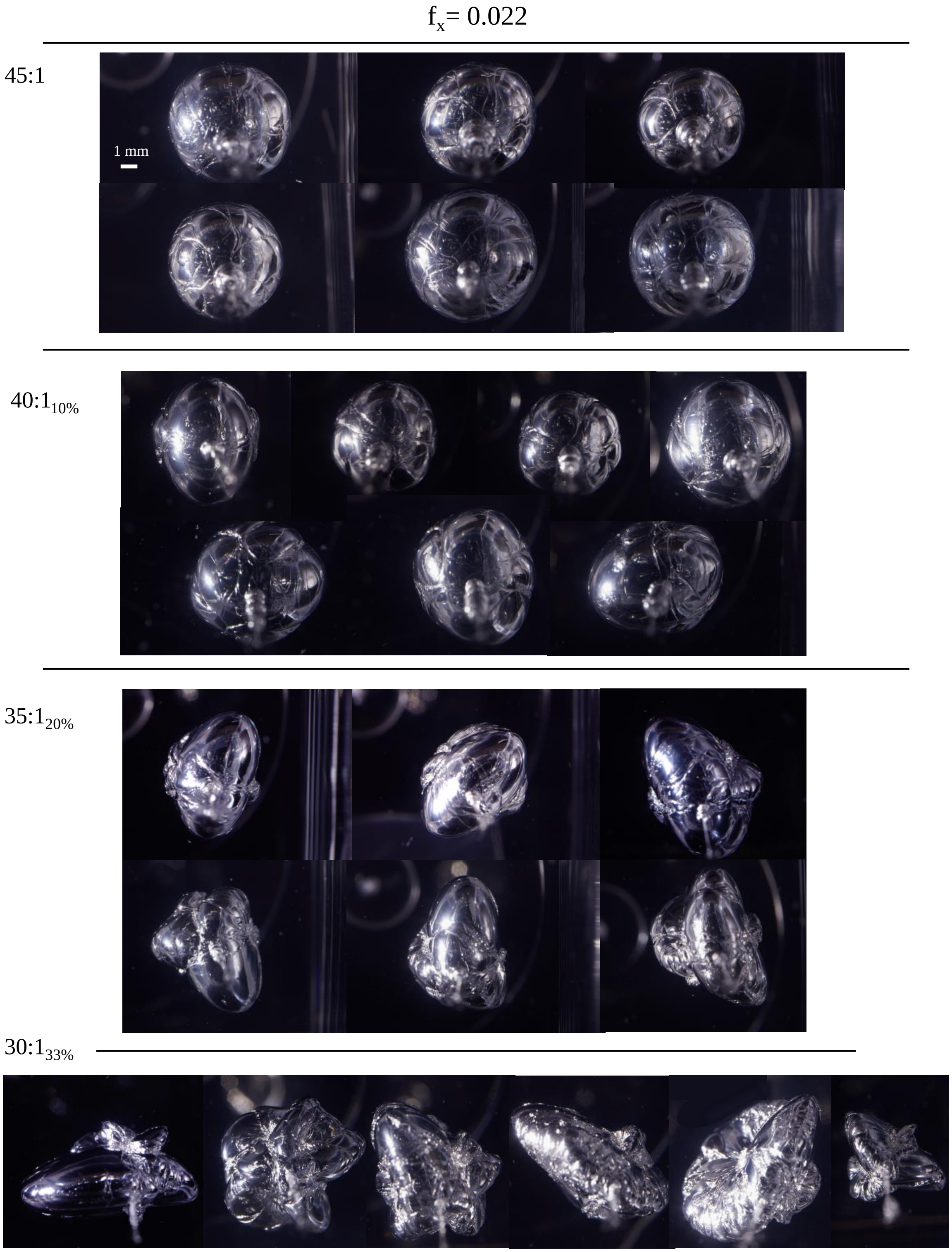

Figure 3.14 Intermediate time-scale cavity morphology. Optical images of cavities in silicone (crosslinker mass fraction, $f_x = 0.022$). Higher oil content leads to earlier lobe formation. Cavities are within 10-20 s of pulse initiation.

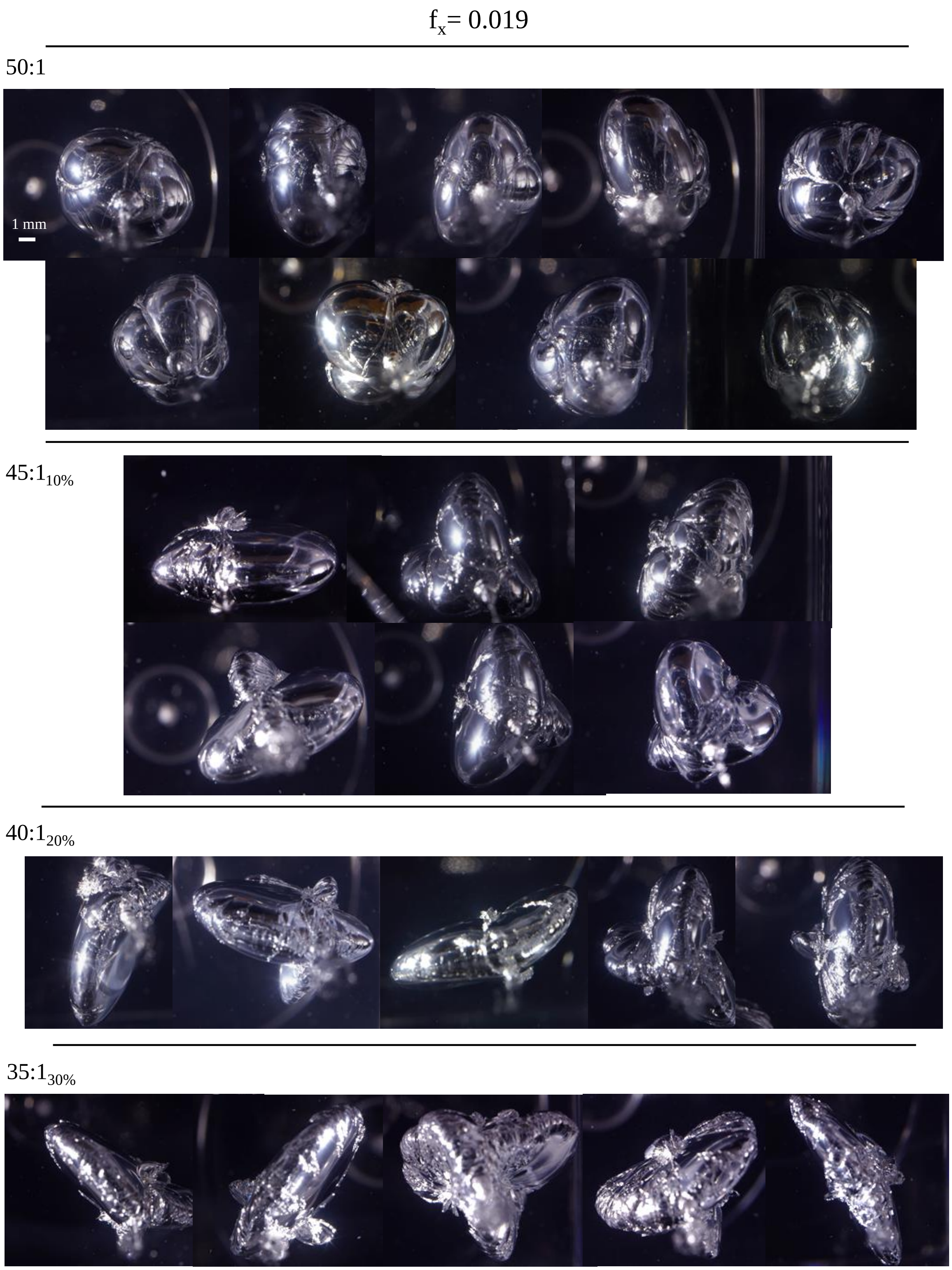

Figure 3.15 Final cavity morphology. Optical images of cavities in silicone (crosslinker mass fraction, $f_x = 0.019$) that illustrate more pronounced crack lobe formation with increasing oil content. Cavities are approximately 6 min after pulse initiation.

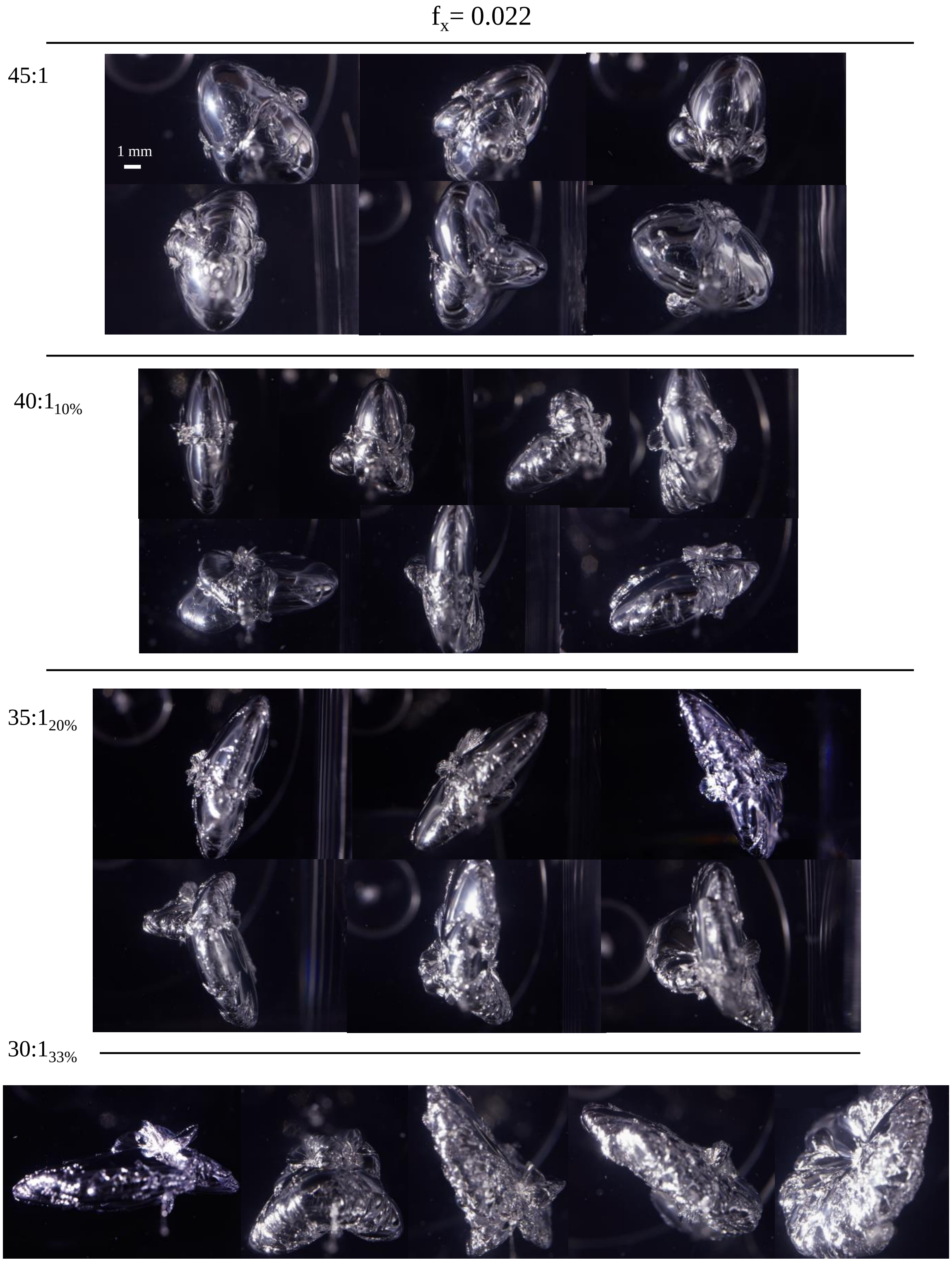

Figure 3.16 Final cavity morphology. Optical images of cavities in silicone (crosslinker mass fraction, $f_x = 0.022$) that illustrate more pronounced crack lobe formation with increasing oil content. Cavities are approximately 6 min after pulse initiation.

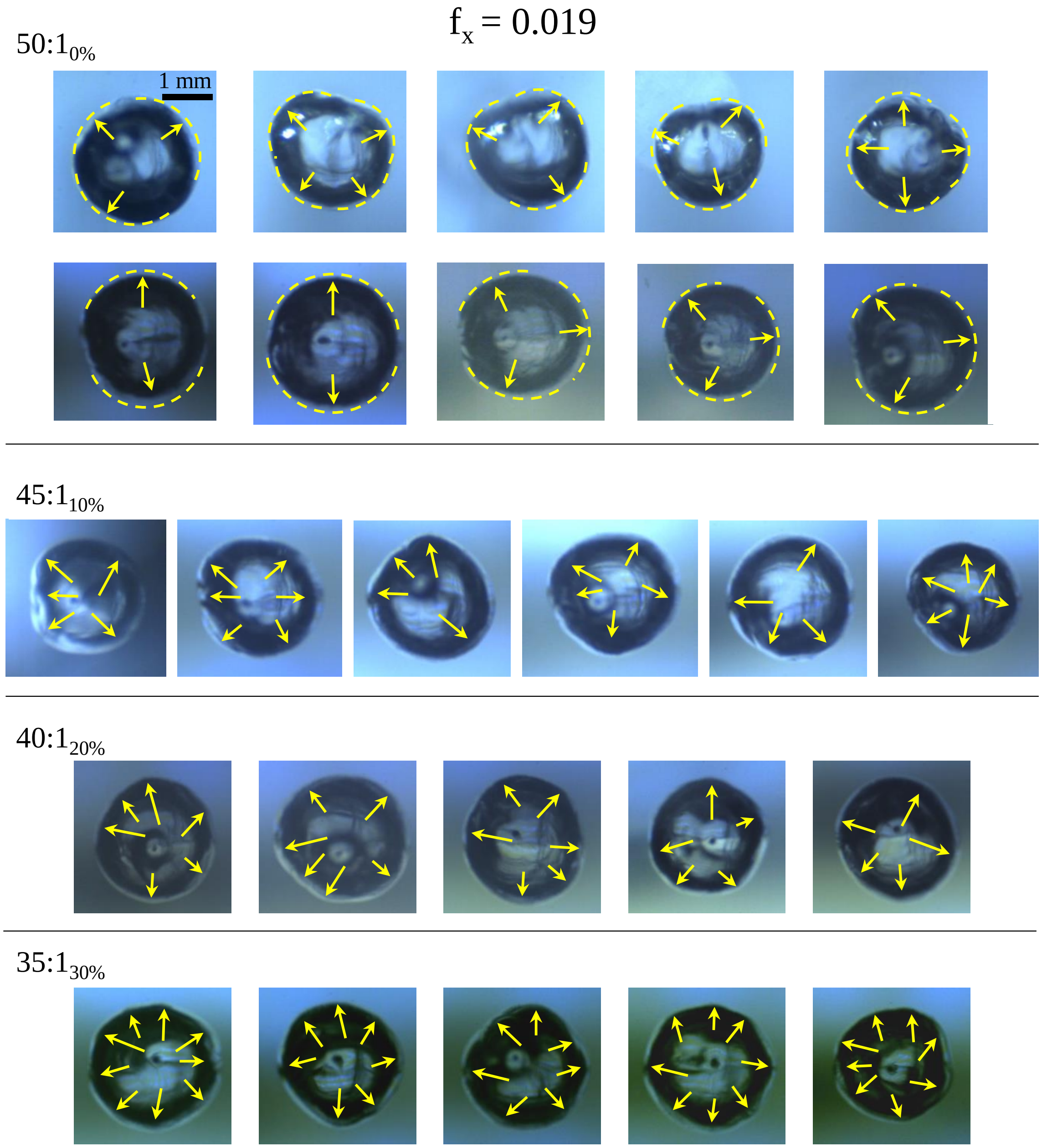

Figure 3.17 High rate cavity morphology. High speed images of cavities in silicone (crosslinker mass fraction, $f_x = 0.019$) at $\Lambda = 7$ illustrate more crack formation with increasing oil content.

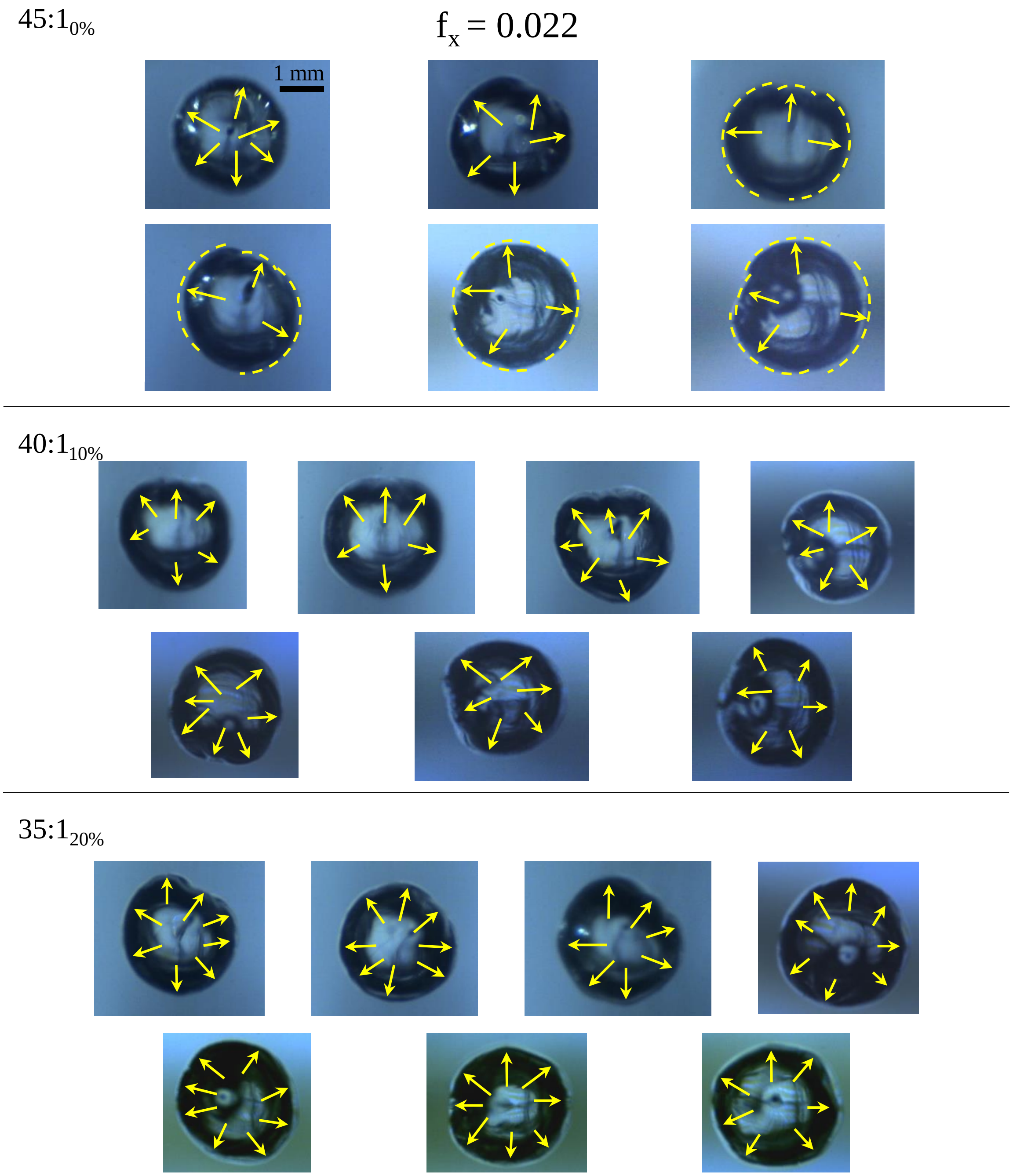

Figure 3.18 High rate cavity morphology. High speed images of cavities in silicone (crosslinker mass fraction, $f_x = 0.022$) at $\Lambda = 7$ illustrate more crack formation within increasing oil content.

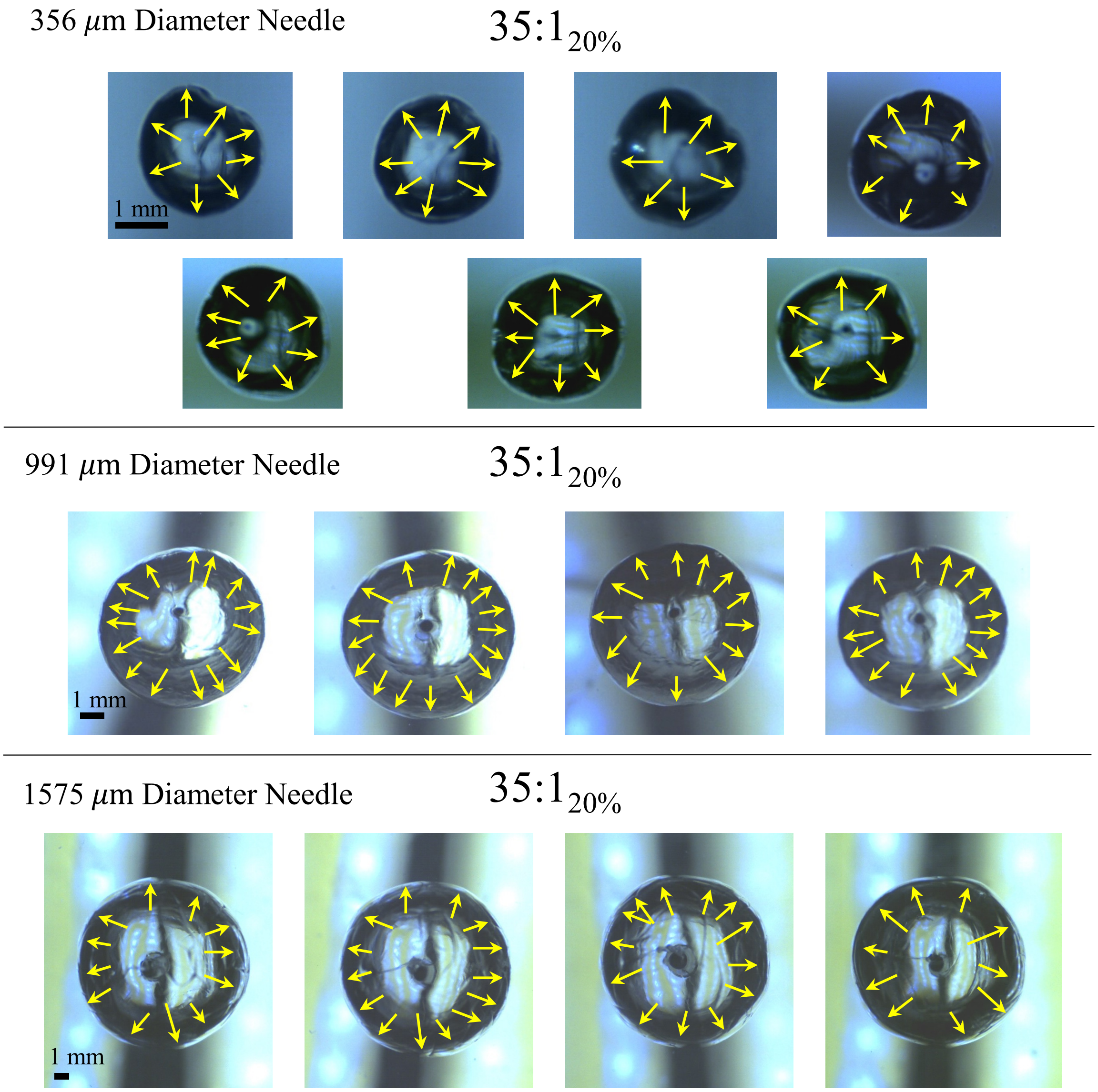

356 μm Diameter Needle $35{:}1_{20\%}$

991 μm Diameter Needle $35{:}1_{20\%}$

1575 μm Diameter Needle $35{:}1_{20\%}$

Figure 3.19 High rate cavity morphology from the same material formulation at different needle sizes. High speed images of cavities from $35 : 1_{20\%}$ PDMS at $\Lambda = 7$ illustrating increased crack formation depends on both needle size and wall velocity.

$25:1_{43\%}$ $40\mu s$ between frames

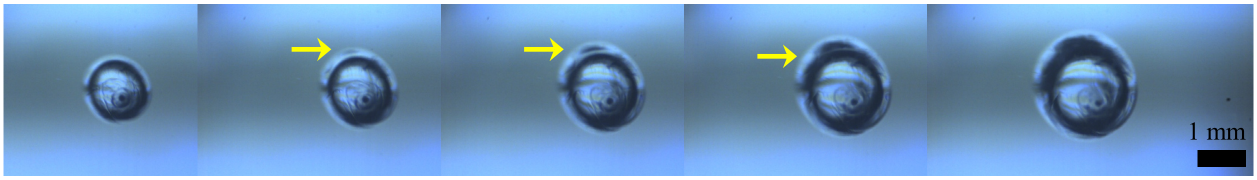

$30:1_{32\%}$ $40\mu s$ between frames

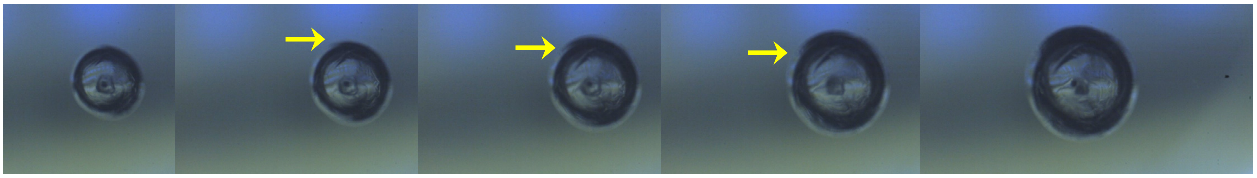

$30:1_{40\%}$ $25\mu s$ between frames

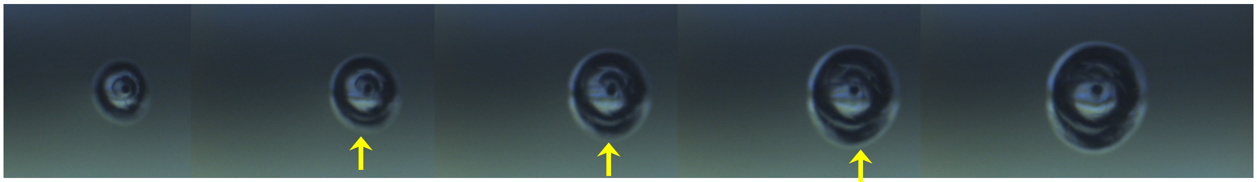

$32.5:1_{34.7\%}$ $40\mu s$ between frames

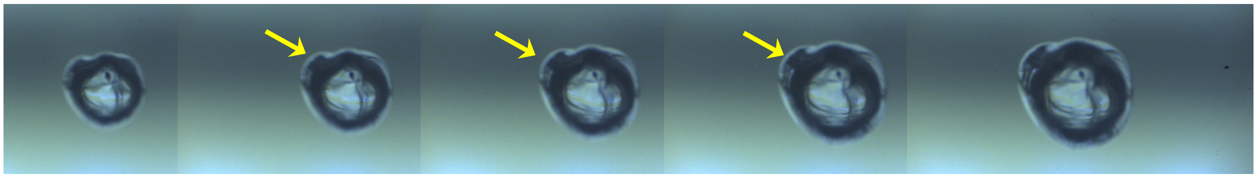

Figure 3.20 Formation of crack lines that are non-parallel with the needle for the most brittle PDMS formulations. Arrows indicate crack formation from sequential high speed images from various brittle formulations.

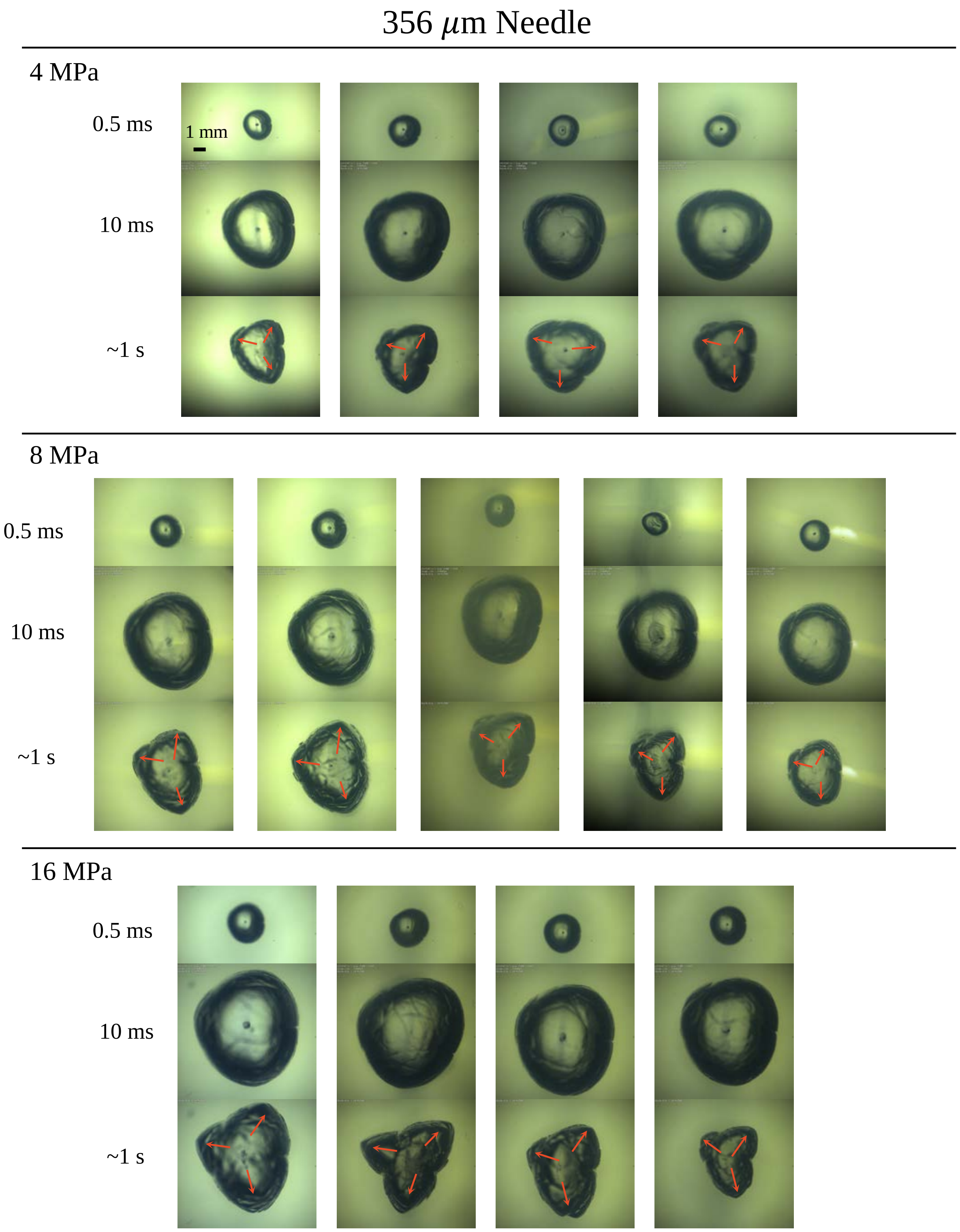

Figure 3.21 Cavitation images in gelatin. High speed images are shown at 0.5 ms, 10 ms, and 1 s at pressures of 4, 8, and 16 MPa reservoir pressures. A 178 μm radius needle is used. Three crack lobes always form.

991 μm Needle

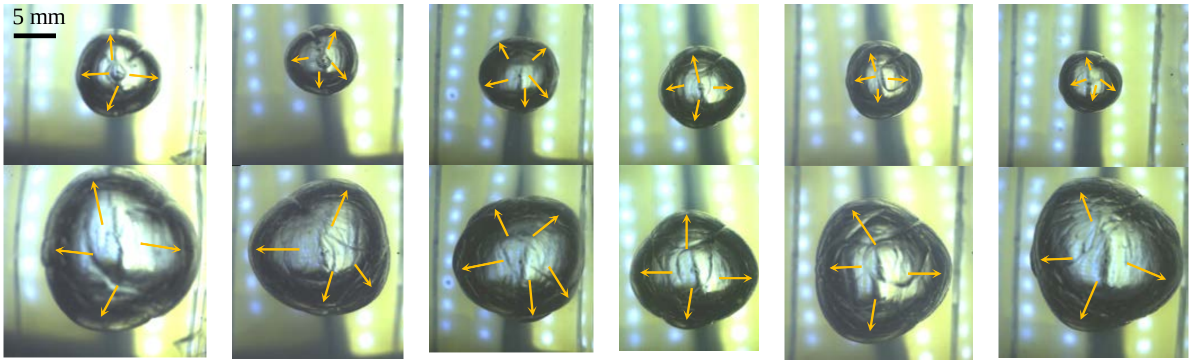

Figure 3.22 Cavitation images in gelatin. High speed images are shown for six samples at early and later times from the start of expansion. A 496 μm radius needle is used and four or five crack lobes.

1575 μm Needle

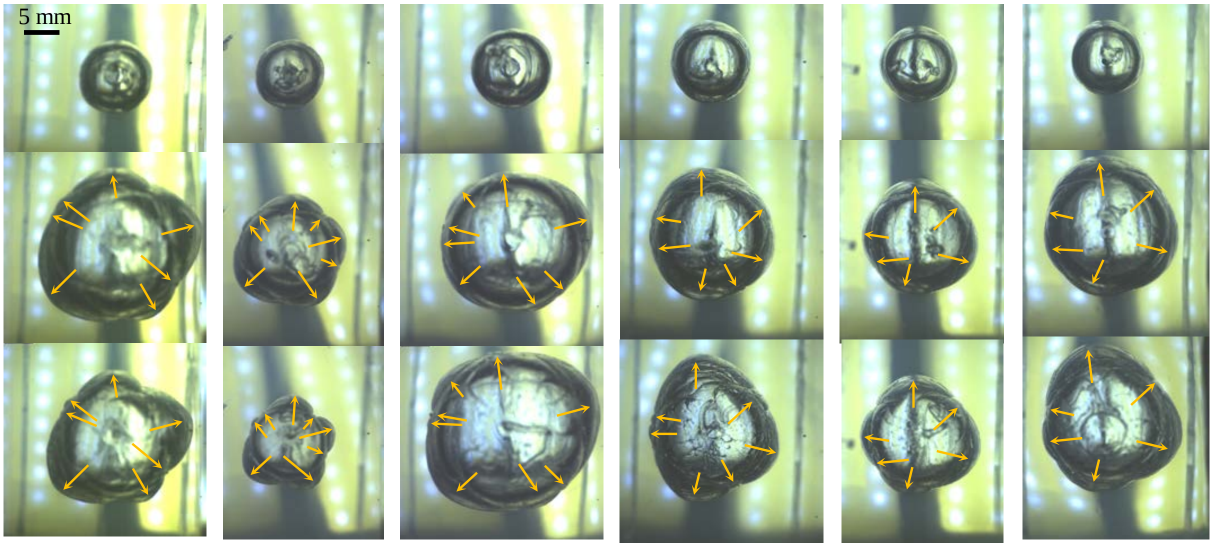

Figure 3.23 Cavitation images in gelatin. High speed images are shown for six samples at early, middle, and late times from the start of expansion from. A 788 μm radius needle is used and four or five crack lobes form.

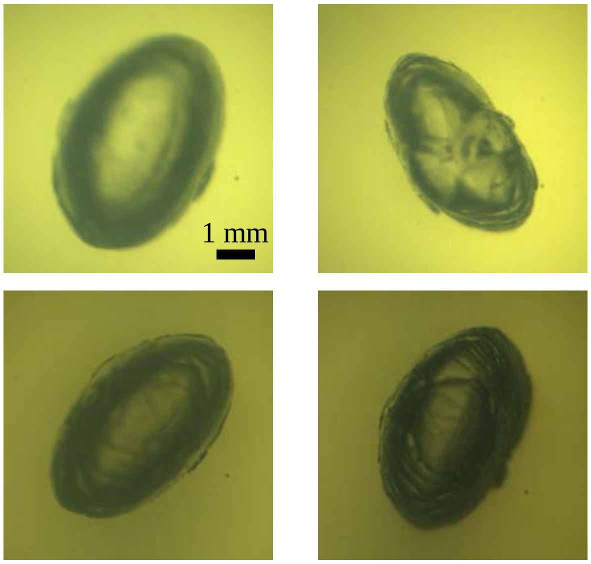

Figure 3.24 Cavitations in 20% gelatin from a 178 μm needle. Only two crack lobes form, indicating an upper bound of modulus and fracture energy on correlation length-based fracture characterization since multiple cracks cannot be induced.

Chapter 4

The effect of material non-linearity on dynamic fracture length scale

4.1 Overview

The localized deformations in the fracture response of the soft-solid formulations investigated in Chapter 3 are well characterized by with a linear constitutive response; however, alternative constitutive responses may be required for tougher materials that fracture at higher strains. In this Chapter, we discuss the implications of the soft-solid correlation length fracture theory for nonlinear and tougher soft-solids that undergo finite deformations before failure and may be investigated in the future. The fracture theory is adapted for a nonlinear Gent hyperelastic model. In addition to previously discussed rate dependent effect of modulus on wavespeed, another phenomenon, acoustoelasticity, must be accounted for when using a nonlinear constitutive response. This contributes a stretch dependence to the wavespeed. We find a similar increase in number of cracks with increasing rate of expansion, but that the stiffening response will produce a measurable crack number difference in only very tough materials, such as in double-network gels.

4.2 Introduction

Low elastic moduli, time-dependent behavior, and finite deformations characterize soft solids. Combined, these features make the prediction of soft solid failure under the variety of loading conditions they encounter challenging. Practical difficulties further complicate dynamic rate testing and damage modeling. In these cases, it is important to know when one can simplify soft solid behavior during analysis. This work explores the effect of material non-linearity, encountered at large deformations, on the density of cracks that form in the surface dynamically-expanding, spherical cavities.

Earlier, we reported on the preferential formation of radially initiated cracks in high-pressure air-driven cavity growth [Chapter 3]. These observations share similarities with the radial cracks that accompany the expansion of 'temporary cavities' that form during terminal ballistics testing. Quantification methods for these ballistic failure morphologies include post-mortem measurement of the number of cracks formed, their lengths, and the area enclosed by cracks.[21,24,32,62,68,78] Similarly, in our lab-scale pressure-driven experiments, the number of radial cracks formed was found to correlate with the toughness of the material. We interpreted these results by adapting a linear, acousto-elastic correlation length model originally developed for metal and ceramics testing[45,46] and drilled borehole detonation.[47,48] For those experiments on relatively brittle materials, linear deformation appears to capture the behavior. However, for tougher materials capable of reaching finite stretches before the onset of failure, a linear model is unreasonable. In this work, we explore when the treatment of nonlinear constitutive behavior becomes necessary and compare analytical predictions for a solid following a Gent model with those for the linear model.

4.3 Modeling Number of Cracks Formed

With hard materials including metals, ceramics, and rock in mind, Grady[45,46,48,80,81] postulated a model for the number of fragments formed following the dynamic loading of an elastic body. This model combines Griffith-type fracture criteria with an elastic-wave-speed-dependent correlation horizon between cracks. We extend this model to dynamically expanding cavities in soft solids by considering the effects of finite deformation on elastic energy and wave-speed.

4.3.1 Crack Correlation Length

Within Grady's correlation horizon two cracks can elastically-interact. As an upper bound, this distance, L, is given by the product of the elastic wave speed and the time available for travel, *e.g.*, the time until the onset of failure, t_f. Since the elastic wave propagates in both directions, Grady argued that the number of cracks in a 2-D ring is approximately the ring circumference divided by $2L$ (See Chapter 3, Figure 3.2). During ballistic testing, tube-like temporary cavities lead to cracks formation and propagation that radiates outward from the projectile trajectory. Similarly, recent experimental observations [Chapter 3], find that cracks grow radially outward when biased by an embedded needle. Thus, following Grady's example we assume that the number of cracks in an expanding cavity of radius, a, may be approximated as the cavity circumference divided by $2L$. For brittle materials, only small deformations occur before fracture so that the cavity circumference at failure is well approximated by the initial circumference. In the following calculations accounting for the finite deformations typical of many soft materials, we use the deformed cavity circumference, $2\pi a$, to predict the number of cracks,

$$N = \frac{2\pi a}{2L} = \frac{\pi \lambda_f A_0}{c_f t_f}, \tag{4.1}$$

where λ_f is the cavity stretch at failure, a/A_0, with A_0 being the initial, undeformed cavity radius. This might correspond to a projectile length scale or the needle diameter[5], depending on the system being probed. We determine λ_f using Griffith fracture criteria in Section 4.3.2. For the linear theory, $a = A_0$. Time-to-failure, t_f, varies with the deformation prior to failure (determined by λ_f) and rate at which that deformation occurs (determined by the cavity wall velocity, V). Defining a 'stretch-rate' for the cavity expansion, $\dot{\lambda} = V/A_0$, we express t_f as,

$$t_f = (a – A_0)/V = \frac{\lambda_f - 1}{\dot{\lambda}}. \tag{4.2}$$

The shear wavespeed, c, in linear elastic materials, is a function of the shear modulus, μ, and the density, ρ, and is given by $\sqrt{\mu/\rho}$. However, changes in instantaneous modulus, μ', accompany non-linear, finite deformations, which leads to a deformation dependent elastic wavespeed, $\sqrt{\mu'/\rho}$.[96–99] Thus, relative to the initial wavespeed, the normalized wavespeed due to deformation, $\tilde{c} = c/\sqrt{\mu/\rho}$, varies as a function of stretch as shown in Figure 4.1c (SI). Since the instantaneous modulus at fracture is a function of the deformation at fracture, λ_f, the wave-speed in Eqn. (4.1) is as well, $\tilde{c}_f = \tilde{c}(\lambda_f)$. Combining Eqns. (4.1) and (4.2) yields the number of cracks that form in a dynamically expanding cavity when finite deformations are considered,

$$N = \pi \frac{\dot{\lambda} A_0}{\sqrt{\mu/\rho}} \underbrace{\frac{1}{\tilde{c}(\lambda_f)} \frac{\lambda_f - 1}{\lambda_f}}_{f(\Gamma/\mu A_0)} . \tag{4.3}$$

$\dot{\lambda}$, A_0, ρ, and μ form one dimensionless group proportional to crack number. $\tilde{c}$ and λ_f both depend on the onset of fracture. As the next section shows, these parameters are only a function of $\Gamma/(\mu A_0)$ and, for the nonlinear model we are considering, the Gent constitutive model parameter J_{lim}. Γ is a fracture energy parameter. As can be seen from Eqn. (4.3), N is linear in $\dot{\lambda} A_0/\sqrt{\mu/\rho}$ (or alternatively V/c) and is a non-linear function of $\Gamma/(\mu A_0)$.

4.3.2 Onset of fracture

We model the soft solids as homogeneous, isotropic, incompressible non-linear elastic materials using the Gent free energy.

$$W = -\frac{\mu J_{\text{lim}}}{2} \log\left(1 - \frac{I-3}{J_{\text{lim}}}\right), \tag{4.4}$$

where I is the first invariant of the Cauchy-Green deformation tensor.[1] Using the same Griffith-like approach as in Chapter 3, fracture occurs when the energy required to create a new surfaces via growth of an infinitesimal length crack, δ, equals the elastic energy released during that same growth. As previously mentioned, this derivation was shown for a spherical cavity by multiple authors.[3,86–88] For the so-called 'spherical crack,' the energy released when a cavity grows from the undeformed configuration, initial radius of A_0, to a new radius, $A = A_0 + \delta$, is

$$\Delta U_F \approx \Gamma(4\pi A^2 – 4\pi A_0^2) \approx 8\pi\Gamma A_0 \delta, \tag{4.5}$$

---

[1] For the deformation considered here, $I = 2\lambda^2 + \lambda^{-4}$. λ is the radial stretch, r/R, with r and R being the deformed and undeformed coordinate positions, respectively.

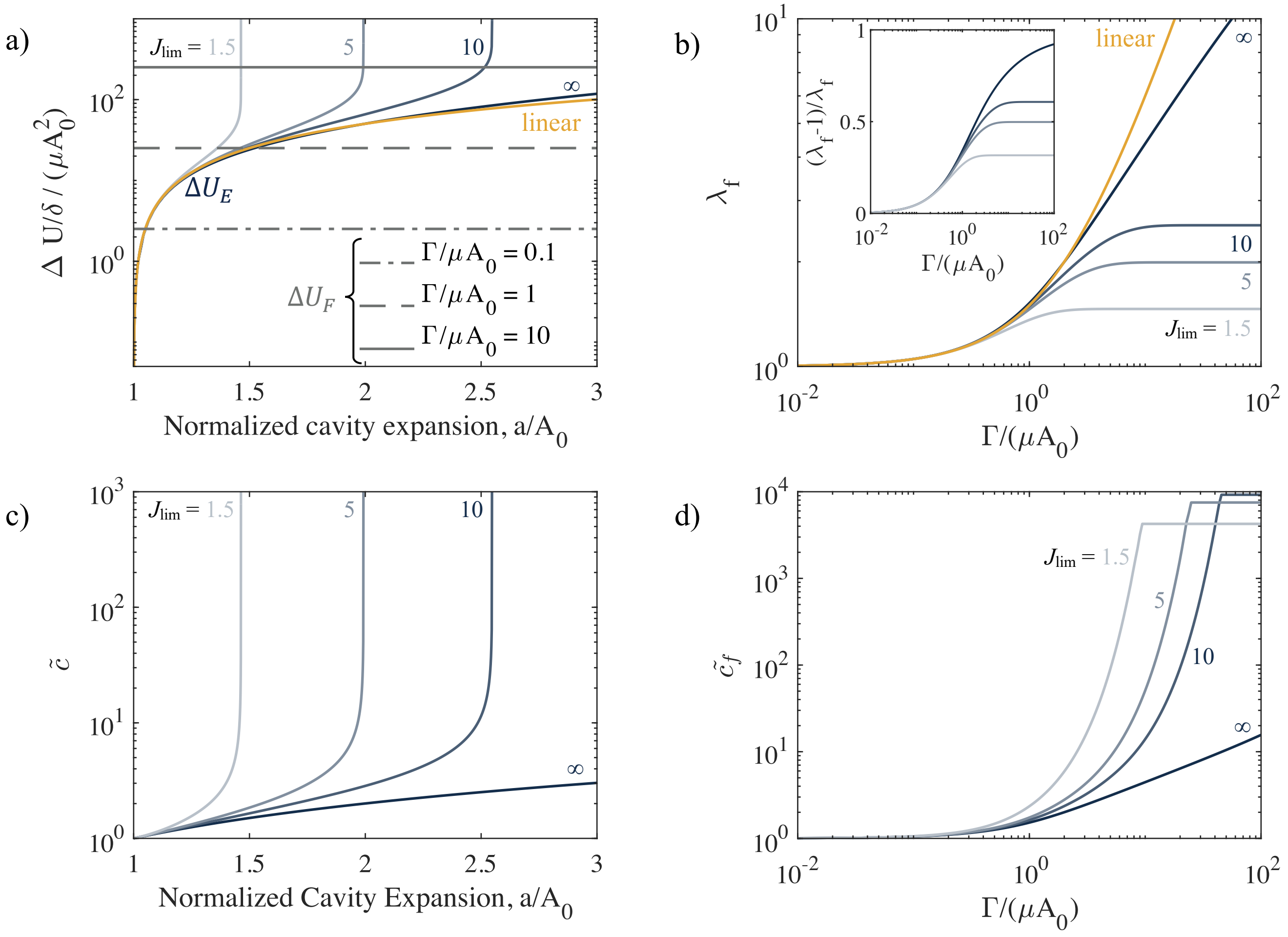

Figure 4.1 Failure onset dependence on the elasto-fracture parameter $\Gamma/\mu A_0$. All plots demonstrate the effect of the Gent model parameter for $J_{\rm lim} = 1.5$, 5, 10, and ∞ (neo-Hookean) using colors of increasing saturation in comparison to a small deformation theory in orange. a) Variation in fracture (gray horizontal lines) and elastic (blue curves) energy components as a function of cavity expansion. The linear theory (orange) approximates the neo-Hookean model closely for the range of stretch values plotted. The intersection of the fracture and energy curves determines the stretch at fracture, λ_f. b) Stretch at fracture versus the elasto-fracture parameter. Inset: Stretch at fracture in the form it takes in Eqn. (4.3). c) Normalized wavespeed variation with stretch-induced changes in effective modulus. d) Normalized wavespeed at the onset of fracture.

to first order in δ. The elastic energy of an expanding spherical cavity of initial radius A' to a deformed radius of a within an infinite elastic solid is given by[89]

$$U_E(a,A') = 4\pi(a^3 – A'^3)\int_1^{a/A'} \frac{\lambda^2 W(\lambda)}{(\lambda^3 – 1)^2} d\lambda. \tag{4.6}$$

The change in elastic energy, ΔU_E, is then determined by the difference

$$\Delta U_E = U_E(a,A) – U_E(a,A_0) = U_E(a,A_0+\delta) – U_E(a,A_0). \tag{4.7}$$

Terms higher than first order in δ are eliminated to yield,

$$\Delta U_E\left(\frac{a}{A_0}\right) \approx 4\pi A_0^2 \left[\frac{\left(\frac{a}{A_0}\right) W\left(\frac{a}{A_0}\right)}{\left(\frac{a}{A_0}\right)^3 - 1} + 3\int_1^{a/A_0} \frac{\lambda^2 W(\lambda)}{(\lambda^3-1)^2} d\lambda\right]\delta. \tag{4.8}$$

As introduced in Chapter 3, this equation can be linearized for small deformations, becoming

$$\Delta U_{E,\text{lin}}(a/A_0) \approx 16\pi A_0^2 \mu (a/A_0 - 1)\delta. \tag{4.9}$$

Figure 4.1a provides a comparison of Eqn. (4.8) evaluated for Gent and neo-Hookean behaviors with the linear behavior given by Eqn. (4.9).

Equating the energy changes per crack length, $\Delta U/\delta$ enables determination of cavity deformation at fracture, $\lambda_f = a/A_0$, where a is now the deformed radius at fracture.

$$\frac{\Delta U_E/\delta}{\mu A_0^2} = \frac{\Delta U_F/\delta}{\mu A_0^2} = 8\pi\frac{\Gamma}{\mu A_0} \tag{4.10}$$

The resulting λ_f is found at the intersection of the fracture and elastic energy curves as illustrated graphically in Figure 4.1a and varies with both J_{lim} and $\Gamma/(\mu A_0)$ as shown in Figure 4.1b. These equations must be solved numerically for the nonlinear behavior. Once we determine the stretch at failure in this way, the elastic wavespeed at fracture, $\tilde{c}_f$, can be calculated (SI), resulting in Fig. 4.1d. Both λ_f and $\tilde{c}_f$ are then substituted into Eqn. (4.3) to yield the predicted number of cracks. This process is greatly simplified for the linear response, which produces the following closed expression for the number of cracks:

$$N = \pi \frac{\dot{\lambda} A_0}{\sqrt{\mu/\rho}} \left(\frac{1}{2} \frac{\Gamma}{\mu A_0} \right)^{-1}. \tag{4.11}$$

4.4 Comparing Linear and Non-linear Predictions

The predictions for number of cracks are shown in Figure 4.2. Despite the somewhat complex set of equations, only two dimensionless groups, $\dot{\lambda} A_0 \sqrt{\rho/\mu}$ and $\Gamma/(\mu A_0)$, and one dimensionless parameter, J_{lim}, are required to describe the predictions as long as the material properties at the appropriate rate are used to calculate them (as opposed to the quasi-static properties). Plots are generated for three orders of magnitude of $\dot{\lambda} A_0 \sqrt{\rho/\mu}$, from 0.1 to 10, and four orders of magnitude of $\Gamma/(\mu A_0)$, 10^{-2} to 10. We expect these parameters to encompass all physically-realizable dynamic fracture scenarios.

It is clear from Figure 4.2 that J_{lim} plays a negligible role in determining N unless $\frac{\Gamma}{\mu A_0} > 1$. This is due to the fact that changes in the term $(\lambda_f - 1)/\lambda_f$ (Fig. 4.1b-inset) associated with increasing $\Gamma/(\mu A_0)$ are almost exactly compensated for by the changes associated with varying J_{lim} for $\tilde{c_f}$ (Fig. 4.1d). The result is a negligible overall change in N. It is only at $\frac{\Gamma}{\mu A_0} > 1$, that changes in $\tilde{c_f}$ associated with varying J_{lim} become orders of magnitude larger than $(\lambda_f - 1)/\lambda_f$, which is bounded by 1.

As indicated in Eqn. (4.3), N is linearly proportional to $\dot{\lambda} A_0/\sqrt{\mu/\rho}$. Figure 4.2b, generated for the neo-Hookean case, $J_{\mathbf{lim}} = \infty$, clearly shows this linearity. The linear curve for $\Gamma/(\mu A_0)$ is unphysical and therefore not included because λ_f clearly falls outside of the small deformation limit (Fig. 4.1a). As might be expected from Fig. 4.2a, only small deviations between the linear and non-linear cases at higher J_{lim} so these plots are not provided.

4.5 Conclusions

Nonlinear modifications to the multiple fracturing theory developed in Chapter 3 were implemented, by incorporating a strain stiffening constitutive response and a stretch dependent wavespeed, based on acoustoelasticity. It was shown that only for materials with a

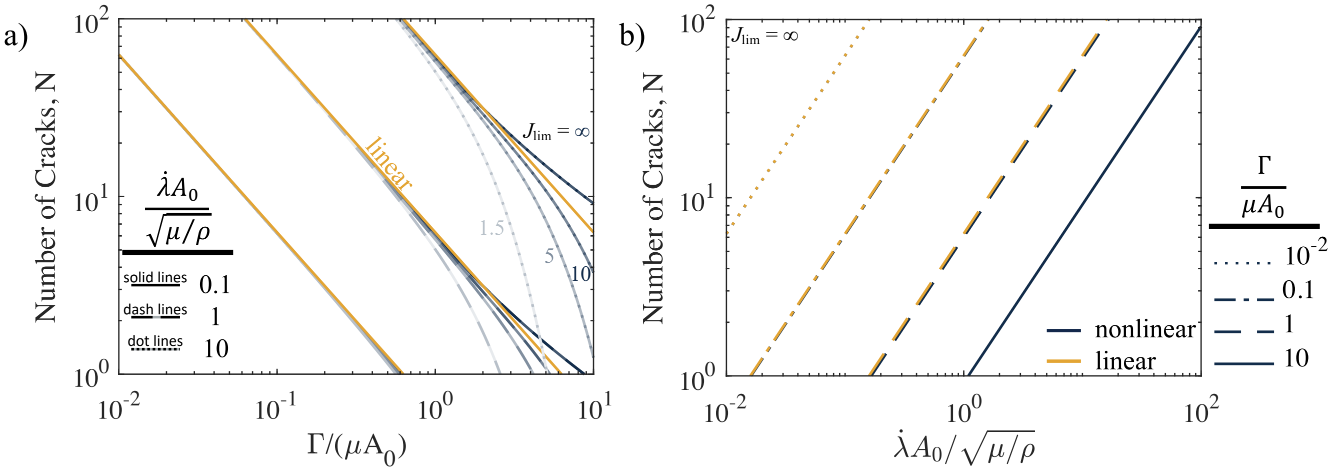

Figure 4.2 Predictions for the number of cracks formed in expanding spherical cavities. a) Dependence of N on $\Gamma/(\mu A_0)$ for $\dot{\lambda}A_0/\sqrt{\mu/\rho}$ = 0.1 (solids lines), 1 (dashed lines), and 10 (dotted lines). The effect of the Gent model parameter $J_{\text{lim}} = 1.5$, 5, 10, and ∞ (neo-Hookean) is shown in both cases using colors of increasing saturation. Linear model predictions for each $\dot{\lambda}A_0/\sqrt{\mu/\rho}$ are given by orange lines. b) Dependence of N on $\dot{\lambda}A_0/\sqrt{\mu/\rho}$ for $\Gamma/(\mu A_0)$ equal to 10^{-2} (dotted), 0.1 (dash-dot), 1 (dash), and 10 (solid). Linear predictions are shown in orange.

a high fracture energy and a consequent larger stretch to failure will the modifications be required. While current methods of high rate experimentation do not report constitutive nonlinearities, these effects may be present in high rate fracture phenomenon of tough soft solids. This could provide a method to interpret the effects of nonlinear stiffening, when they cannot be directly measured. Terminal ballistics will generate deformation rates high enough to induce multiple fracturing, especially with the range of toughness present in biological tissues, nonlinear constitutive response could predict the damage from those impacts.

4.6 Supplementary Information: Instantaneous Wavespeed

Expression for deformation dependent wavespeed, Gent model, with derivation following Ogden.[96] The elasticity tensor, $\boldsymbol{\mathcal{A}}$, specifically for the stiffness in the 1-2 direction is,

$$J\,\mathscr{A}_{01212} = \frac{J_{lim}\ \lambda^6\ \mu}{-1+(3+J_{lim})\,\lambda^4-\ \lambda^6}. \tag{4.12}$$

with $J=1$, defined as the determinant of the deformation gradient tensor, $J=\det\mathbf{F}=1$, since we consider incompressible materials. The stretch dependent shear wave speed is given by,

$$c_{12} = \sqrt{\frac{\mathscr{A}_{01212}}{\rho}}. \tag{4.13}$$

Chapter 5

Multi-crack formation in ballistic impacts

5.1 Overview

I analyze ballistic impacts of 6 different types of non-deforming handgun and rifle projectiles in a soft-solid tissue simulant, 10% ballistic gelatin, using the material properties and fracture theory developed in Chapter 3. Ballistic impacts with soft-solids generate cavitations due to the transfer of the bullet's kinetic energy to the soft-solid. Post-mortem analysis of damage from bullets has traditionally used several different types of methods (see Chapter 3) to characterize the final fractured surfaces; however, no consistent method has been found to standardize different types of projectiles. While the crack analysis of impacts from one type of projectile may be provide consistent crack analysis when varying kinetic energy with the same projectile, comparison to another projectile finds a different fit, implying that the material is responding differently. The mechanical properties should respond consistently. Using the physics that describe cavitation, it is possible to standardize damage from any type of projectile. I propose a new method of accounting for cavitation damage that can be used for future analysis and incorporate rate dependent material response.

5.2 Methods and Materials

5.2.1 Ballistic Gelatin Preparation

Ballistic gelatin preparation follows the proposed standardization method from Jussila,[92] where half of the required water is heated to 70°C and the other half remains room temperature (20°C). The entire amount of gelatin powder is mixed into the room temperature water until the solution is uniform and allowed to swell for at least two minutes before the heated water is added to the solution, which equilibrates to 45°C. This temperature is maintained and gently stirred to dissolve all gelatin particles while minimize foaming. Foam is skimmed from the surface, then the solution is poured into the mold. Any air bubbles that form are suctioned out with a pipette. Molds are covered with plastic to prevent evaporation and the solution is cooled at 5°C for 48 hours. Cubic molds with sides of 15.24 cm are used for ballistic testing.

5.2.2 Ballistic Impacts

Ballistic tests were carried out at the University of Illinois at Urbana-Champaign Police Training Institute Tactical Training Center with the test set up shown in Figure 5.1. Five handgun projectiles and one rifle projectile were fired into 10% ballistic gelatin while using high-speed imaging (30,000 – 50,000 fps) to record the deformation. Each projectile was fired 3.5 m from the gelatin with a chronograph (Caldwell) measuring the projectile velocity immediately prior to impact. All projectiles had full metal jackets and did not deform on impact. Full specifications on each projectile are shown in Table 5.1.

5.3 Experimental Results and Discussion

5.3.1 Overview of Experimental Results

Like the cavitations formed by the SBC device, ballistic impacts generate large expansions behind the bullet. Visual analysis of cavitations viewed perpendicular to the bullet path reveal localized deviations from circularity. These deviations are crack tips forming and growing. Similar to SBC cavitations multiple cracks appear circumferentially around the cavity; however, cracks also form at various longitudinal locations along the projectile's trajectory. I show that consideration of projectile energy *and* shape accounts for the damage created. Although the multiple fracture theory shown in Chapter 3 could be used to estimate fracture energy of gelatin, I lack experimental evidence to define an initial radius of expansion, instead I provide bounding values of radii that should be considered.

Bullet Caliber	Diameter ± 0.05 [mm]	Velocity [m/s]	Kinetic Energy [J]	Form Factor[100]	Image
.22	5.70	1046 ± 122	132	1	
.223	5.71	2718 ± 32	1219	0.4	
.38	9.10	756 ± 10	225	1.6	
.357	9.04	1089 ± 51	565	1.6	
.40	10.14	1064 ± 17	560	1.6	
.45	11.43	767 ± 13	405	1	

Table 5.1 Bullet and ballistic impact characteristics for the six bullets used. Velocity and kinetic energy estimates are averages of at least two trials. One of three form factors are chosen based on comparison of bullet shapes to published values.[100] Round nose, flat nose, and spitzer type bullets are used. A smaller form factor correlates to a more streamline design.

Figure 5.1 Firing range at Police Training Institute Tactical Training Center. The high speed camera captures images orthogonal to the projectile trajectory, with backlighting to enhance contrast. A chronograph (Caldwell) measures the projectile velocity just before impact with the gelatin

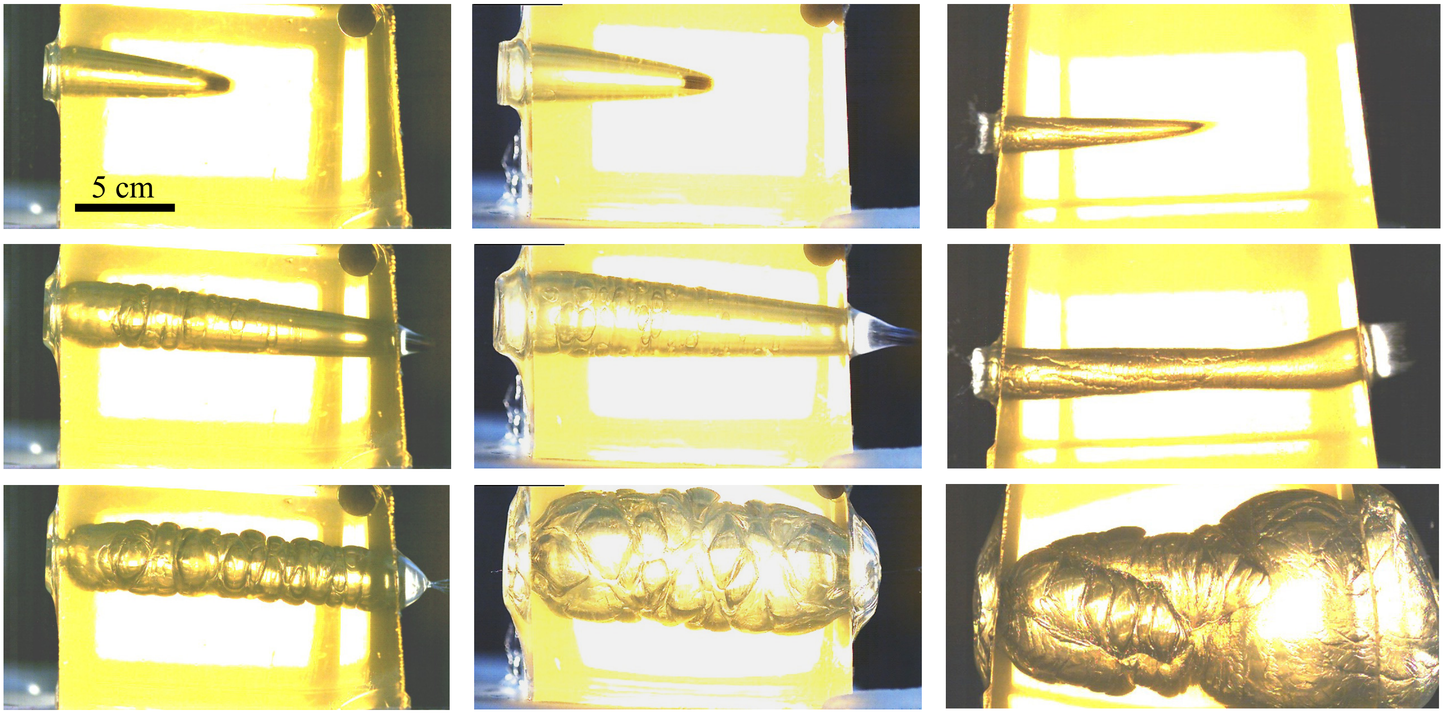

.38 caliber
D = 9.10 mm
KE = 225 J

.357 caliber
D = 9.04 mm
KE = 565 J

.223 caliber
D = 5.71 mm
KE = 1219 J

Figure 5.2 Temporary cavity expansion images of three ballistic impacts from .38, .357, .223 caliber impacts. Image sequence shows the bullet halfway through the sample, the bullet exiting the sample, and when the maximum temporary cavity is reached. Note that the .223 bullet yawed halfway through the sample leading to a difference in temporary cavity shape.

5.3.2 Multiple Crack Formation in Ballistic impacts

Multiple cracks form in ballistic impacts with ballistic gelatin when temporary cavities form. Figure 5.2 shows three representative impacts. In the .38 and .357 caliber impacts, first the projectile causes a smooth cavity to form behind the bullet, then tearing can be observed along this cavity. In the .223 caliber impact, cracks are immediately observable. This difference is attributable to the nose shape of the bullets (see Table 5.1), the .38 and .357 caliber projectiles have a larger flat nose (meplat) than the streamline nose of the .223 caliber projectile. The streamline nose of the .223 bullet allows expansion to begin at a much smaller radius than the other two projectiles, so the criticial radial stretch to induce cracking is attained at a smaller relative cavity size. When flat nose bullets generate cavities, with a larger apparent initial radius, several tears appear along and around cavities when the critical stretch is reached at a larger relative cavity size. Lack of full views around the cavity prevent an accurate count of number of cracks initiated. An estimate from this single view would predict anywhere from 3-6 initiated cracks for all flat nose impacts. Cracks do not appear to coalesce during expansion, as in SBC cavitations of gelatin, (*cf.* middle and bottom rows of images in Fig.5.2, suggesting that post-mortem inspection could be used to count cracks and use then apply those numbers in the multiple fracture theory of Chapter 3. Post-mortem inspection of all impacts were made by slicing samples perpendicular to the bullet path. Typically slices have 3-4 cracks, but no more than 5, maximum post-mortem crack counts of each of the 6 bullet types are shown in Figure 5.4a. Increasing impact energy increases the number of cracks. However, the effective projectile radius is undetermined, so it cannot be directly applied to the multiple fracture theory for material characterization, but is certainly affected by the projectile shape. Nonetheless, the crack formation genearated by the temporary cavitations is similar in behavior to the cavitations shown in Chapter 3. Temporary cavity crack formation should be treated as a fracture phenomenon, and accounting for projectile shape is essential for post-mortem crack analysis.

5.3.3 Energy Effects on Damage Formation

Temporary cavity size is frequently correlated to bullet energy,[21,62,68] but a more appropriate consideration is comparing ballistic impact energy to the damage that persists after the temporary cavity. It has previously been shown that there is a linear relationship between cavity or damaged volume and the energy transferred by the projectile,[21] $V = \mu E_{tr}$. While this linear relation fits well when comparing bullets of the same type[62,68] the linear constant μ, is different for different bullet types.[62,68] Note that this linear constant, μ, with units of [cm^3/J], is not the shear modulus, but I will preserve the notation used by Kneubehul, et. al. As I have alluded to, damage from a bullet depends on its shape and these high rate expansions should be treated as a fracture phenomenon. Surprisingly, Kneubuehl, et al.[21]

have already shown how this difference in bullet shape is accounted for in the energy transfer equation, but this dependence has not been implemented in analysis.[62,68] Rewriting the above equation to account for energy transferred per slice thickness, Δs, along the bullet path gives,

$$V = \mu \sum E'_{tr} \Delta s. \tag{5.1}$$

Where the energy transferred per thickness is defined as, $E'_{tr} = 2\mathscr{R}E$. Here, E, is the instantaneous kinetic energy of the projectile. This introduces the dependence of the bullet size and shape on the change in energy, included within the retardation coefficient,

$$\mathscr{R} = \frac{C_D \rho A_p}{2m_p}. \tag{5.2}$$

The retardation coefficient includes, the area of the projectile, A_p, the mass of the projectile, m_p, the drag coefficient, C_D, and ρ, the density of the target. We use bullet form factors[100] as approximations for the drag coefficient. Utilizing the above expressions and dividing through by Δs provides the appropriate relation for damaged area and instantaneous projectile energy for a given slice,

$$A_{crack} = \mu\, 2\mathscr{R}E. \tag{5.3}$$

This relation allows for different bullet types to be compared if accounted for with $\mathscr{R}$, which could change during penetration if a deforming bullet is used or if the bullet tumbles. While many post-mortem crack analyses have been used: Fissure Surface Area, Total Crack Length Method, Wound Profile Method, Maximum Radius, and others,[21,24,32,62,68,78] some of which have arbitrary constants, we propose a simple method, the Total Crack Area (TCA), which accounts for all free surfaces (cracks and holes) created by an impact. Although this method seems similar to the methods, it does not selectively choose only a couple cracks, nor does it relate cracks to circumference of the temporary cavity, among many other relations (see Jussila[24] for summary of equations). It accounts for the area of the permanent cavity, πr_{pc}^2, treating it as a circular hole, as well as the *surface area* of the radial cracks.

$$TCA = 2\delta_i \sum_i l_i + \pi r_{pc}^2 \tag{5.4}$$

The factor of 2 accounts for the fact that 2 surfaces are created by any number, i, of radial cracks of length, l. The factor δ_i has dimensions of length but magnitude of 1 for radial cracks that are present but where both sides are touching. This is to maintain dimensional congruity with the permanent cavity's dimensions of area while accounting for radial crack areas of zero thickness. If a radial crack does not have zero thickness, then the area of that crack should be accounted for in the equation. Examples of crack measurements are shown in Figure 5.3. Although there are some cracks that appear to be unaccounted for, these cracks are not on the surface of the slice and are within its thickness. The TCA versus $2\mathscr{R}E$ for 6 different bullet types and 14 individual impacts are plotted as filled circles in Figure 5.4a, all of these measurements were made at a slice depth of 2.5 cm. An additional

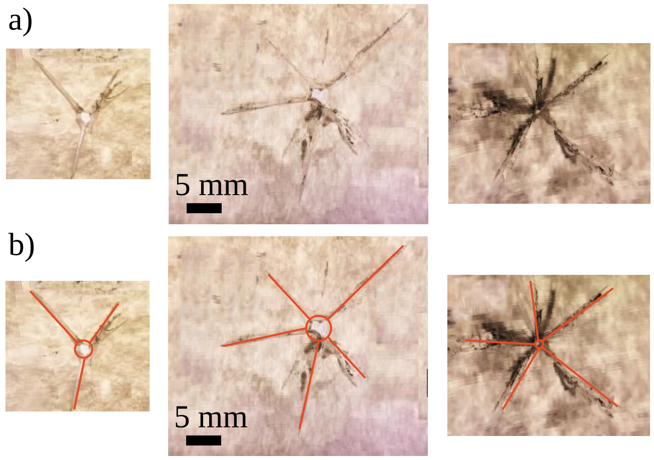

.38 caliber .223 caliber .357 caliber

Figure 5.3 Total Crack Area (TCA) measurements from slices of ballistic gelatin (thickness$\approx$ 1 cm) at a depth of 2.5 cm from the point of impact. (a) Images of damage in slices from the .38, .223, and .357 caliber impacts shown in Fig. 5.2. (b) Same slices as in (a), but with crack measurements overlaid. The permanent channel in the center of the damage is approximated with a circle, while radial cracks are measured with lines. Although some cracks appear to be uncounted they are within the thickness of the slice. Only crack area that is exposed to the surface of the slice should be counted.

10 measurements were made using 4 of the bullet types at depths of 4 and 6 cm and are shown as open circles. The instantaneous kinetic energy of all projectiles was estimated using the velocity measured from high speed imaging, which is relatively constant throughout the penetration. The dashed line is a linear fit of the data, showing that different bullet types can be compared together when accounting for the damaging potential (or retardation coefficient), $\mathscr{R}$. The curved solid line will be discussed in 5.3.4. In Figure 5.4b the same TCA versus bullet kinetic energy, as has traditionally been done, is plotted. It shows large scatter and no discernible pattern. Therefore, bullet shape must be affects damage and can be accounted for with the form factor and area in $\mathscr{R}$.

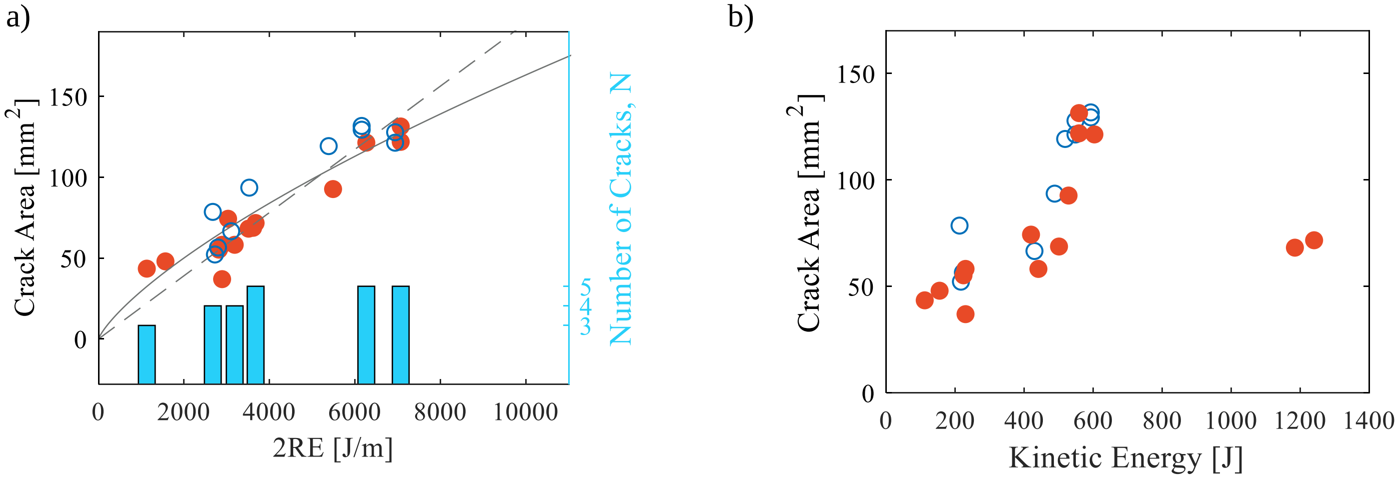

Figure 5.4 Ballistic impact analysis: TCA results vs. $2\mathscr{R}E$ and kinetic energy of impacts vs. wall velocity. (a) A plot of TCA vs. $2\mathscr{R}E$ for all 6 bullets at several depths shows that the data collapses together. (b) A plot of TCA vs. kinetic energy for the same data in (a). There is no correlation in the data. The two data points grouped to the right are from the .223 caliber bullets

5.3.4 Rate Effects on Damage Formation

A linear fit of the form, $V = \mu E_{tr}$, assumes that the material is not rate dependent, but we have shown in Chapter 3 that ballistic gelatin fracture energy does depend on the rate of deformation. The variable, μ, can be considered similar to the inverse of the fracture energy. It is inversely proportional to the energy required to open a cavity volume, while fracture energy relates the energy required to create surface area. Since volume and area are correlated, I propose a strain rate dependent modification to the linear relation in Equation 5.3, where $\mu(\dot{\varepsilon})$, and $\dot{\varepsilon} \propto \sqrt{E}$. The term, $\sqrt{E}$, can be used as a proxy for strain rate. In Figure 5.5, the square root of the average kinetic energy and average wall velocity are plotted, for the six bullet types a linear fit shows good agreement implying that $\sqrt{E} \propto v \propto \dot{\varepsilon}$. The rate dependent fracture energy can be expressed as, $\gamma = (\gamma_0 \exp\left[q_1 \dot{\lambda}^{q_2}\right])^n$. Where, q_1 and q_2 are as defined in Chapter 3 and $n = -1$ is the power law relationship used in Chapter 3. Using these modifications, the rate dependent relation is,

$$A_{crack} = \gamma_0^{-1} \exp\left[q_1 \dot{\lambda}^{q_2}\right]^{-n} 2\mathscr{R}E. \tag{5.5}$$

In the range of energies tested there is not much difference in assuming either a linear fit

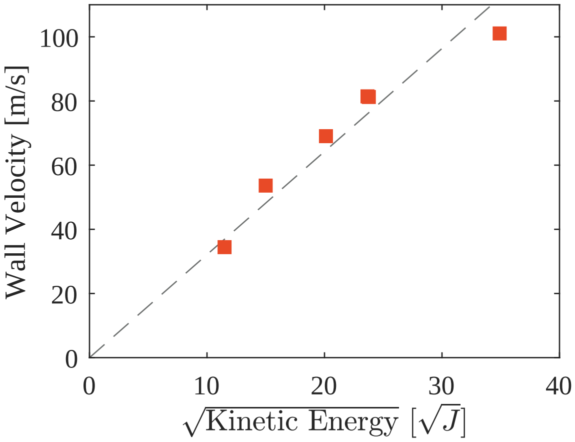

Figure 5.5 Bullet kinetic energy and cavity wall velocity. The square root of the kinetic energy and the resulting cavity wall velocity shows an approximately linear proportionality, fit shown. Therefore the square root of the kinetic energy can be used as a proxy for strain rate.

(dashed line) or a rate dependent modification (solid line) in Figure 5.4. However, rate dependent effects could become more important for impacts of higher energy. This implies that there will be a diminishing increase in crack area as more damage inducing bullet geometries are implemented (greater $\mathscr{R}$) or higher energy projectiles are used as gelatin toughness increases at higher strain rates.

5.3.5 Multiple Fracture Theory Applied to Ballistic Impacts

Since cracks do not appear to coalesce and the peri- and post-mortem crack counts are similar (both $\sim$3-6), the post-mortem crack numbers are used to estimate multiple fracture response. The appropriate radius of expansion is unknown for projectile impacts and this initial radius value was shown in Chapter 3 to have an influence on the predicted fracture energy. Figure 5.6 plots the maximum, post-mortem crack numbers for each of the six bullet types as a function of wall velocity. In Fig. 5.6a the quasi-static fracture energy, determined from SBC tests, is used to plot estimated crack numbers and two bounding radii are shown. These bounds show a narrow range, 0.15 to 0.30 mm, of expected initial radii that bounds all results. In Fig. 5.6b an average fracture energy from previously published results[94,95] is similarly used to bound the data with radii estimates of 0.70 to 1.4 mm. In both of these plots, in regions above $\sim$40 m/s, the crack number prediction curves are relatively flat, indicating that the initial radius is a dominating factor in determining how many cracks occur. This could potentially be exploited in fracture energy determination characterization by firing identically shaped projectiles within a narrow range of radii and measuring the number of resulting cracks. The initial radii generated by bullet impact is likely related to the form factor and the size of the bullet's meplat. The spitzer bullet (.223 caliber) has a meplat radius of approximately 0.5 mm and the flatnose bullets have a meplat radii of: 2.4 mm (.38 caliber), 3 mm (.357 caliber), and 3.6 mm (.40 caliber). Note that the radii of the permanent cavity, r_{pc}, also scale closely, but smaller than, the meplat: 0.25-0.4 mm (.223), 0.9-1.35 mm (.38), 1.6-2.0 mm (.357), and 1.8-2.0 mm (.40). These smaller sizes could be indicative of the initial radii to assume and are promisingly near the range of bounds predicted by the multiple fracture theory.

5.4 Conclusion

I have provided a method to analyze ballistic impact damage, the Total Crack Area method, which allows for bullets of different types to be analyzed systematically and consistent with fracture phenomenon. Considering a bullet's form factor allows its damage potential to be

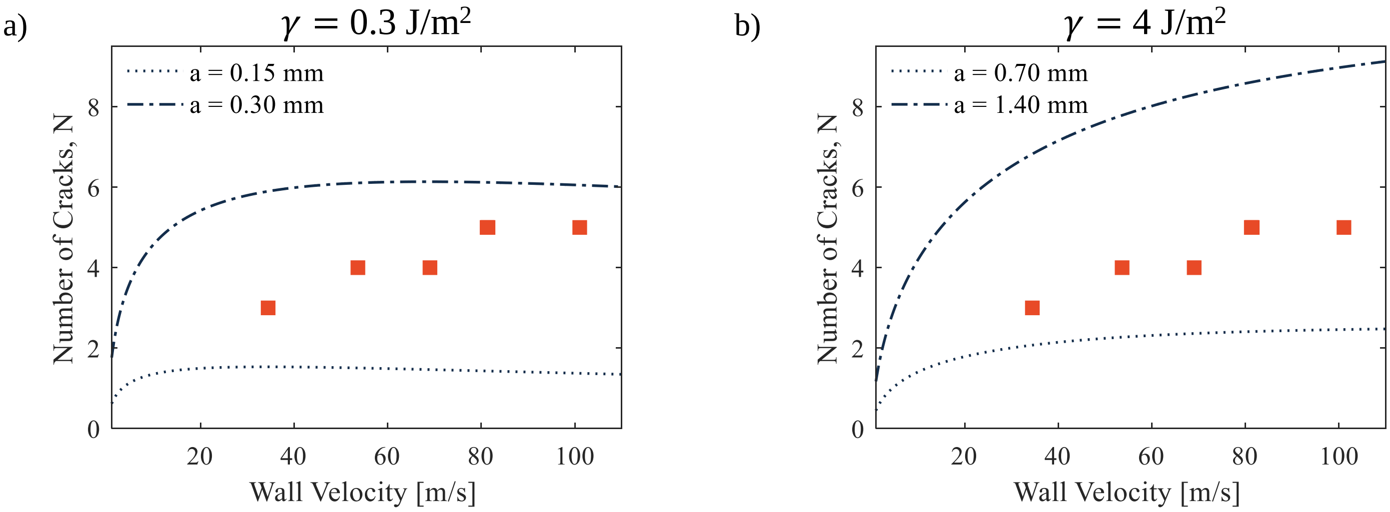

Figure 5.6 Bullet size estimates for multiple fracture theory. (a) A plot of TCA vs. $2\mathscr{R}E$ for all 6 bullets at several depths.

combined with its kinetic energy to find a better correlation with measured damage than just using bullet kinetic energy alone. Incorporating the strain rate effect on fracture toughness may become a more important consideration as higher kinetic energy impacts are studied. Counting the number of radial cracks induced during a ballistic impact may be a simple method to characterize a material's fracture energy; however, more work needs to be done on defining the initial radius of expansion caused by the projectile.

5.5 Acknowledgements

I would like to express many thanks to the University of Illinois at Urbana-Champaign Police Training Institute Tactical Training Center for use of the firing range as well as for use of a handgun.

Chapter 6

Creasing in evaporation-driven cavity collapse

6.1 Overview

In this Chapter we shift the focus of localized deformations to spherical cavities undergoing quasi-static contractions, instead of high-rate expansions, finding that creases can be used to analyze nonlinear stiffening response. We report on crease morphology and evolution at the surface of contracting cavities embedded within elastomeric solids of varying composition (Sylgard 184: pre-polymer to crosslinker mixing ratios of 10:1, 12:1, 17.5:1, and 25:1). Cavity contraction is achieved through evaporation of an embedded 10 μL liquid droplet. In validation of recent theoretical predictions, strain-stiffening modeled via the Gent constitutive relation [Jin and Suo, *JMPS*, 2015, **74**, 68-79] is found to govern both crease onset and crease density. Specifically, crease onset matches prediction using only experimentally-measured parameters. Neo-Hookean solids are found to prefer initiating creasing with many short creases that join to form a collapsed state with only a few creases, whereas creasing in Gent solids initiates with a few creases that propagate across the cavity surface. These experimental observations are explained by energy minimization using finite element simulation of a cylindrical crease geometry.

6.2 Introduction

The range of known geometric and material parameters governing creasing[101–103] highlight deformation as a means for controlling the surface topology of soft solids. Like the related phenomena of wrinkling and folding, crease-like deformation has been leveraged by technology[104–106] and nature[107,108] alike. Because these phenomena are primarily found on surfaces, most observations have been on planar[102,103,109,110] or convex geometries.[108] Recently, creasing on the inner surface of everted cylinders has been observed cross-sectionally,[111] here we describe creasing on the inner surface of a spherical cavity within an elastomeric solid.

This study was motivated by both theoretical predictions for osmosis-driven collapse[49] as well as an aim toward understanding biological structural changes due to fluid loss from an enclosed cavity. For example, in the animal kingdom, the female reproductivity cycle involves regression of the post-egg-release corpus luteum (a fluid filled transient endocrine gland essential to fertility) to corpus albicans before eventual re-absorption.[112] In the plant kingdom, structures in organ-based plants couple water flux to geometric changes in order to achieve motion without muscle.[113,114] The latter coupling is found in hygromorphs[115,116]; surface tension propulsion[117]; and drying-associated, hydrostatic-pressure-driven energy storage that precedes failure[118] or cavitation[114,119] events. As a result of the large deformations in these soft systems, creases are observed at the inner liquid-solid interface. We begin to explore the formation of these creases in a spherically symmetric geometry by embedding the droplet within a large elastomeric solid.

Briefly, creasing in soft solids is due to the application of a globally compressive strain that, after reaching a critical value, results in the onset of localized, self-contacting deformations on the solid's surface.[101] An overview of the extensive creasing literature is available in a number of important publications.[101,102,120] Here we will focus on three key findings most relevant to describing our observations of creasing in spherical cavities within elastomeric solids. First, recent theory finds that hyperelastic strain-stiffening delays the onset of creasing as a function of applied strain.[50] For reference, incompressible, neo-Hookean elastomers, which exhibit no strain-stiffening, crease at a uniaxial plane-strain of 0.35.[101,102] This behavior has been validated by experimental observation in several soft materials.[102,110] Crease onset occurs at the same strain value, regardless of the material's shear modulus, μ. To our knowledge, most creasing experiments are performed with constant composition materials, i.e., constant modulus, with one notable exception finding a dependence of crease-onset-strain on cross-linker in polyacrylamide gels.[110] These authors

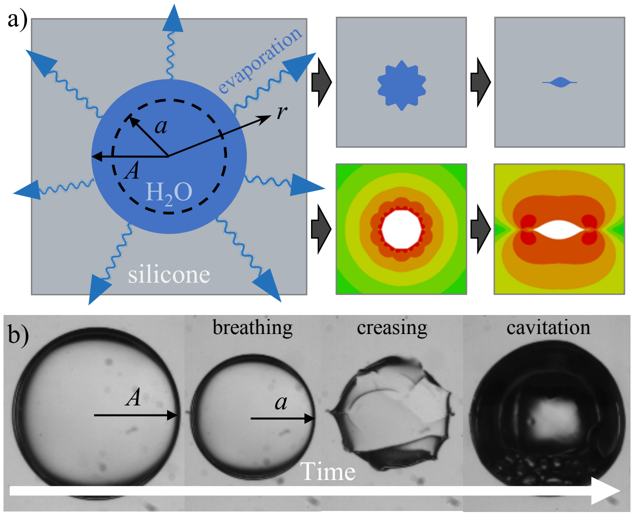

Figure 6.1 Overview of experimental system. a) Schematic of an embedded water droplet contracting via evaporation through the silicone elastomer. Contraction leads to surface creasing (top right). Bottom right: Results from finite element simulation of deformation within a cylindrical cavity. b) Progression of a cavity during evaporation: breathing mode, creasing at the liquid solid interface, and eventual cavitation of the liquid droplet within.

attributed this observation to possible variation in compressibility with changes in the gel composition; verification was left for future study. More recently however, Jin and Suo[50] calculated that for a strain-stiffening Gent material,[121] a larger strain is required to induce creasing for materials with earlier onset of strain-stiffening. This behavior is predicted to result in crease suppression for materials with early onset of strain-stiffening ($J_{lim} = 3.1$, where J_{lim} determines the onset of strain-stiffening and is the first strain invariant minus 3 evaluated at the limiting stretch state). The second key finding is that after creasing has occurred, crease density decreases with the increasing application of strain. Quantitative predictions of crease density, dependent on geometry,[49,102,122] are based on energetic arguments comparing strain energy between finite element models of differing crease number or number density. Third, creasing behavior can be altered by surface energy, γ, which may act as an energy barrier similar to that found in nucleation theory. Chen et al.[103] showed that creases, which nucleate from pre-existing defects then grow via channeling,[109] can be induced to grow/channel further when surface energy is decreased. This phenomenon was shown to relate to a film-thickness-normalized elastocapillary number, $\gamma/\mu t$, where t is the thickness of the creased film. The results presented here validate and build upon each of these three findings for a spherical geometry.

Our observations of evaporating liquid droplets embedded within elastomeric solids of varying composition experimentally verify Jin and Suo's prediction of strain-stiffening governed crease onset. We also find, in agreement with the second characteristic described above, that increasing deformation leads to a decrease in crease density for neo-Hookean materials. However, this crease density dependence breaks down for strain-stiffening materials. We qualitatively describe this phenomena using finite element simulation of a cylindrical cavity. Further, we find that the morphology of surface creases is largely unaffected by decreased surface energy at large deformations, but near crease onset, surface energy plays a small role. For the macroscale cavities ($\sim$ 1 mm) studied here, this suggests that at low strains an elastocapillary number, $\gamma/\mu L$, that uses crease size as L rather than system geometry (cavity size) is more appropriate in the deformation regime near crease onset.

This article is organized as follows. We outline the materials used and describe methods for sample fabrication and finite element simulation. Contraction of the liquid-filled cavity in the breathing mode,[49] during which the cavity remains spherical, is modeled using mass transport. Dependence of cavity deformation at the onset of creasing is demonstrated to have quantitative agreement with Jin and Suo[50]'s predictions via independent characterization of the elastomer's constitutive behavior. We then show results for crease morphology evolution as a function of decreasing cavity volume, drawing parallels with a simulated cylindrical geometry. All creasing results are interpreted assuming a biaxial compressive state at the liquid/cavity interface as in Cai et al.[49] We show evidence for a small surface energy dependence of crease morphology near onset. Finally, we touch on cavitation of the embedded liquid droplet.

6.3 Methods

6.3.1 Cavity Sample Fabrication and Testing

Embedded-water-droplet samples are created using polydimethylsiloxane elastomer base and curing agent (Sylgard 184, Dow Corning). Four different base-to-curing agent weight ratios are used: 10:1, 12:1, 17.5:1, and 25:1. After thorough mixing, the uncured polymer is degassed then poured between four supported poly-methylmethacrylate (PMMA) sheets. The PMMA provides an undistorted exterior surface for viewing upon release. 10 μL of reverse osmosis water (Millipore) is pipetted into the bottom of the uncured PDMS. The mold is cured at 80°C for 75 minutes. During curing, buoyant forces drive the water droplet into the middle of the sample. The same technique is used to embed surfactant droplets within PDMS. We use surfactant 3-[hydro(polyethyleneoxy) propyl] heptamethyltrisiloxane (Gelest) at a concentration of 0.5 mg/mL.

Upon curing, samples are placed either in front of the camera for observation or in a sealed container containing an open water source. During observation, a hotplate maintains a temperature of 60°C via constant heat output (Figure 6.2a). Images are taken at 30 minute intervals over the course of evaporation ($\sim$ 3 days) until cavitation occurs. Radii are determined using ImageJ. Images of post-creased droplets are characterized manually, using Matlab to record data (ESI†).

6.3.2 Compression Sample Fabrication and Testing

Compression samples are obtained using cylindrical aluminum molds under curing conditions identical to those above. Two molds are used to mitigate issues of barreling and stability during testing: 12.7 diameter, 15.88 mm height (10:1 and 12:1 mixing ratios) and 20.05 mm diameter, 19.05 mm height (17.5:1 and 25:1). Two testing conditions were used: room temperature and after overnight immersion in a 60 °C water bath. The results are compared in Table S1 ESI†. A test stand (Mark-10 ESM 301) displaces the cylindrical specimens at an engineering strain rate of 10^{-3} 1/s while acquiring loading data. Silicon grease reduces friction at the loading platens.

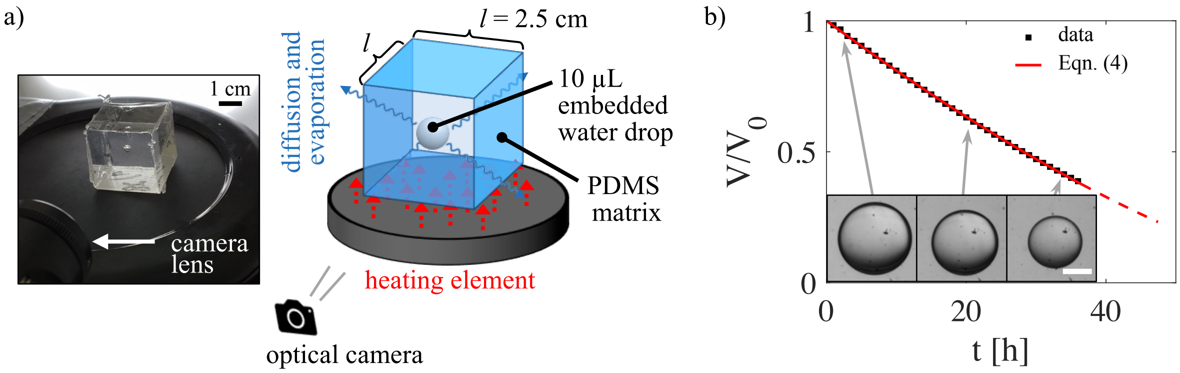

Figure 6.2 Droplet evaporation. a) A photograph of the experimental setup for scale (left) and a schematic (right) showing the 2.5 cm cubic elastomer with embedded droplet. The heating element increases evaporative flux. b) Modeling of breathing mode deformation dynamics using quasi-steady state diffusive transport (red line, Eqn. 6.4. The scale bar in the inset images is 1 mm.

6.3.3 Finite element simulation

The finite element software, ABAQUS, was used to model creasing of a cylindrical cavity of radius A in a cylindrical solid of radius $B = 10A$ under plane-strain conditions. Creases were initiated by the addition of a small defect on one of the periodic boundaries[50,102,107] with the number of creases present, N, being set by modeling a radial section of the cylinder with periodic boundaries on the section edges. The depth of the defect is $1/100^{\text{th}}$ the cavity radius (See ESI†). The angle of inclusion within the section is given by $180°/N$. The mesh is refined around the defect so that element size is approximately $1/100^{\text{th}}$ the size of defect. (See ESI†for further detail.) The outer cylinder surface is traction free and a negative pressure load is applied to the inner surface. The material is incompressible and follows either the built-in neo-Hookean, hyperelastic material model or Jin and Suo's user-defined subroutine (UMAT) implementation of the Gent model.[50]

6.4 Results and Discussion

As the droplet within the PDMS evaporates, the spherical cavity within the polymer contracts, eventually forming creases at the surface if deformation surpasses critical strain criteria. The cohesive strength and surface energy of water enable the cavity's quasi-static collapse. In most cases, after creasing occurs the water droplet cavitates, allowing the elastomer to relax to an unloaded state. We document the breathing and creasing behavior optically and describe them using mass transport,[123] continuum mechanics,[49,50] and energetic models.[102,103] In particular, we draw upon recent theory predicting the effect of strain-stiffening on creasing.[50]

6.4.1 Evaporation During Breathing Mode

During breathing mode deformation, the cavity volume decreases while maintaining the cavity's spherical shape [inset, Figure 6.2b]. Following Rice and Do's[123] solution for the diffusive loss of mass from a sphere in an infinite, stagnant medium, changes in the water droplet are predicted using a mass balance at the droplet surface. For water having density ρ_W comprising a droplet of radius a, a mass balance yields

$$\rho_W \left(\frac{4}{3}\pi\right) \frac{da}{dt} = -4\pi a^2(t) N|_{r=a}, \tag{6.1}$$

where the diffusive flux at the droplet surface, $N|_{r=a}$, is given by Fick's Law,

$$N|_{r=a} = -\frac{D_{WP}}{1 - {}^{C^*}\!/\!_{\rho}} \frac{\partial C}{\partial r}. \tag{6.2}$$

Here D_{WP} is the diffusivity of water through the polymer and C is the mass concentration of water such that ${}^{C^*}\!/\!_{\rho}$ is the mass fraction of water at the fluid-solid interface. An approximate solution to this expression arises from the assumption of quasi-steady state in the water concentration profile as determined by

$$D_{WP} \nabla C \overset{\text{r symm.}}{=} \frac{D_{WP}}{r^2} \frac{\partial}{\partial r} \left(r^2 \frac{\partial C}{\partial r} \right) = \frac{\partial C}{\partial t} \approx 0. \tag{6.3}$$

The solution to this differential equation is

$$\left(\frac{a}{A}\right)^2 = \left(\frac{V}{V_0}\right)^{2/3} = 1 - \frac{2SD_{WP}}{A^2} t \tag{6.4}$$

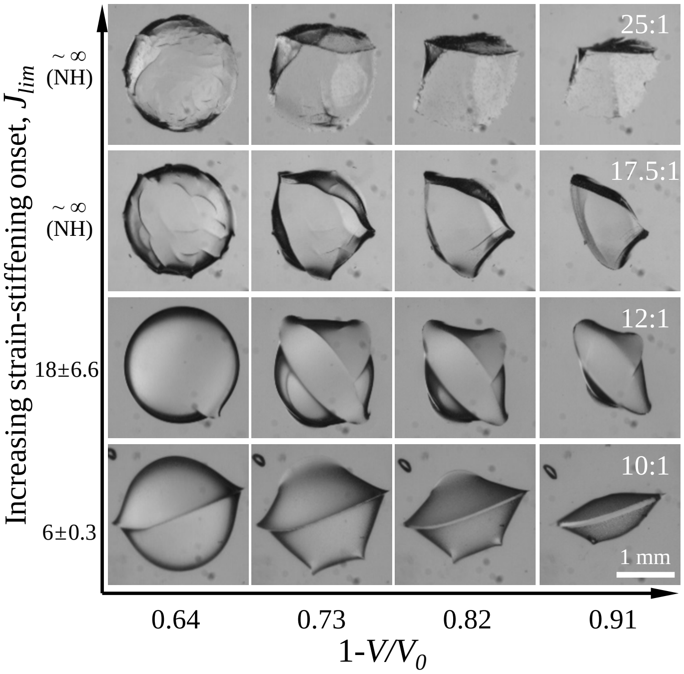

Figure 6.3 Cavity morphology evolution for varying elastomer composition. Top row: Stiffest, earliest strain-stiffening onset (10:1 mixing ratio), Bottom row: Softest, approximately neo-Hookean behavior (25:1). Images along each row correspond to normalized cavity volume losses ($1-V/V_0$) ranging from 0.64 to 0.91. The axes of abscissas relates to time as determined in section 6.4.1.

where the solubility factor, S, which accounts for initial and boundary conditions, is given by $S = (C^* - C_0)/[\rho_W(1 - C^*/\rho)]$.[123] Initially, water concentration within the polymer is taken to be a uniform value, C_0, and the droplet has an initial radius, A. Boundary conditions are: 1) fixed concentration C^* at the droplet surface, as determined by solubility of water in Sylgard 184 ($C^*/\rho = 7.5 \times 10^{-4}$ from Randall and Doyle[124]) and 2) fixed concentration far from the droplet surface, C_0, for which we use literature values of water solubility in Sylgard 184 ($C_0/\rho = 2.6 \times 10^{-5}$ from Harley et al.[125], relative humidity: 40%, Henry's law constant: 0.082 cm^3 STP/g at 60°C). Given the low solubility of water in Sylgard, the density ρ, is approximated as that of Sylgard 965 kg/m^3 as per manufacturer data.

The droplet dynamics modeled by Eqn. 6.4 accurately describe the breathing mode deformation observed experimentally. Radii extracted from time-lapse images of the droplet are fit using a solubility value of $S = 7.1 \times 10^{-4}$ (as described above) keeping A and D_{WP} as fitting parameters. Figure 6.2b shows a representative fit converted to normalized droplet volume versus time, $V/V_0 = (a/A)^3$. Fitted values for A differ less than 0.15±0.3% from initial radius values taken from final, unloaded cavities, illustrating consistency between the fit and experiments. Diffusivity did not show a trend as a function of mixing ratio; the mean diffusivity across all samples was $4.9\times10^{-9} \pm 1.3 \times 10^{-9}\mathrm{m}^2/\mathrm{s}$, within the range of previously measured values.[124,126] Given the close description of the change in droplet size via Eqn. 6.4 we use an extrapolation of this fit in order to calculate the magnitude of applied deformation, i.e., decrease in cavity volume, to creased cavities that can no longer be assumed to be spherical.

6.4.2 Crease Onset

After a period of breathing mode deformation, creases begin to form at the cavity-liquid interface.[3] Figure 6.3 illustrates the evolution of this crease-governed deformation over time due to water evaporation. Cavity volume lost, $V_0 - V$, taken to be proportional to the droplet mass under the assumption of incompressibility, is determined through extrapolation of the fit described in the previous section. Figure 6.3 compares morphology across mixing ratios, but at identical normalized cavity volume changes, $(V_0 - V)/V_0 = 1 - V/V_0$. In the higher mixing ratio samples (17.5:1, 25:1), the morphology of crease onset is generally characterized by many short creases. In contrast, for the lower mixing ratio samples (10:1, 12:1), one or two longer creases are present near onset. After significant water loss ($1 - V/V_0 > 0.8$), the cavities become highly deformed and the number of creases becomes similar across all mixing ratios. Both crease onset and evolution compare favorably with modified plane-strain theories for crease formation and behavior as we will discuss.

For an incompressible neo-Hookean material, creasing has been predicted[101] and observed[110,127] to occur under a uniaxial plane strain of $\varepsilon = 0.354$, independent of modulus. Following the parallel made by Cai et al. between uniaxial plane strain and deformation at the surface of a spherical cavity,[49] we relate the uniaxial strain, ε to the cavity stretch ratio,

---

[3] Water within a few samples cavitated prior to crease onset, see ESI.†

a/A, as

$$\frac{a}{A} = (1-\varepsilon)^{2/3} \tag{6.5}$$

(SI 6.7.1). The predicted cavity stretch ratio for crease onset, $a/A|_c = 0.75$, resulting from this relation fails to capture the composition dependence of crease onset shown in Figure 6.4 (dashed line).

Mixing ratio is often oversimplified to a change in linear shear modulus, μ, for Sylgard 184 under the assumption of neo-Hookean behavior at all compositions.[128,129] However, changes in modulus for a neo-Hookean solid would have no effect on crease onset or morphology,[101] failing to describe the composition dependence we observe in Fig. 6.3. We show that this composition dependence is primarily due to strain-stiffening, in validation of Jin and Suo's predictions.[50] These results illustrate the importance of accounting for material constitutive behavior in creasing systems.

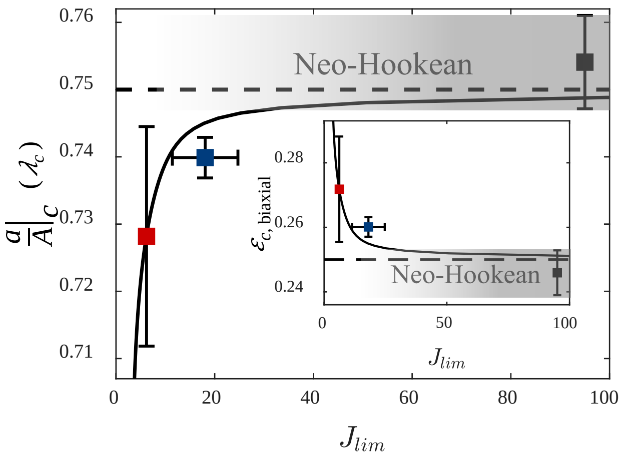

Figure 6.4 Verification of delayed crease onset due to early onset of strain-stiffening as quantified by J_{lim}. The y-axis is the normalized cavity radius, a/A, at crease onset, which is equivalent to the critical biaxial stretch ratio at the cavity surface, λ_c. Red, blue, and black symbols correspond to mixing ratios of 10:1, 12:1, and combined 17.5:1 and 25:1 data, respectively. Error bars are the standard deviation from five or more samples. The black curve corresponds to Gent model creasing onset predicted by Jin and Suo[50], modified for a spherical geometry using Eqn. 6.5. The dashed curve represents crease onset for neo-Hookean behavior. For measured values of $J_{lim} >\sim 40$ strain stiffening occurs at such a high stretch that the behavior is indistinguishable from neo-Hookean behavior, as depicted in the gradient region. Inset: Results re-plotted as critical biaxial strain, ε_c, versus J_{lim}.

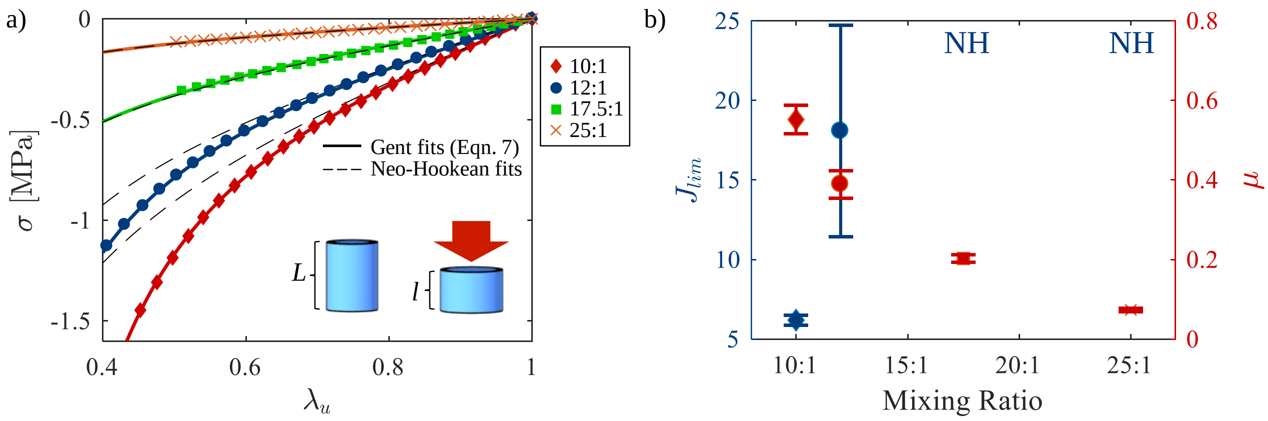

Figure 6.5 Strain-stiffening material behavior of hydrated Sylgard 184 at 60 °C. a) Selected uniaxial compression curves for 10:1 (red diamonds), 12:1 (blue circles), 17.5:1 (green squares), and 25:1 (orange ×'s) mixing ratios. Gent model (Eqn. 6.7) fits are given with solid lines. Black, dashed curves denote Neo-Hookean fits to the initial loading data ($0.9 \leq \lambda_u \leq 1$). b) Gent model fit parameters, J_{lim} and μ determined from a). J_{lim} and experimentally determined crease onset values comprise the experimental data in Fig. 6.4.

Strain-Stiffening Material Behavior

Validating Jin and Suo's[50] predictions requires evaluation of each composition as a strain-stiffening, Gent hyperelastic solid.[121] The strain energy function for the Gent model is given by

$$W = \frac{\mu J_{lim}}{2} \ln(1 - J/J_{lim}), \tag{6.6}$$

where μ is the small strain shear modulus, $J = I - 3$ (I is the first strain invariant of the Cauchy-Green strain tensor), and J_{lim} determines the stretch value at which the strain energy asymptotes to infinity. We experimentally determine J_{lim} from uniaxial compression tests as shown in Figure 6.5a. True stress (assuming incompressibility) under uniaxial load, σ, and stretch, $\lambda_u = l/L$ (Fig. 6.5a), data are fit to the Gent hyperelastic model under uniaxial loading:

$$\sigma = \left(\lambda_u^2 - \frac{1}{\lambda_u}\right) \frac{\mu J_{lim}}{J_{lim} - \lambda_u^2 - \frac{2}{\lambda_u} + 3}. \tag{6.7}$$

Four representative compression curves and their corresponding fits are shown in Fig. 6.5a. For the lowest mixing ratios (10:1 and 12:1), Fig. 6.5 illustrates the improved fit of the

Gent model (solid lines) in comparison to a Neo-Hookean model fit using the low stretch response (thin dashed lines). For the largest mixing ratios used (17.5:1 and 25:1), behavior is indistinguishable from neo-Hookean within the limitations of this testing geometry. Resulting fit parameters μ and J_{lim}, plotted in Fig. 6.5b, quantify the increase in J_{lim} with increasing mixing ratio. Characterization under two environmental conditions, hydrated at 60 °C and room temperature (Table S1 ESI†), revealed a weak dependence of J_{lim} and a moderate dependence of μ on environment. We conclude from these findings that gradients in either temperature or water concentration within the polymer have negligible effect on J_{lim} and therefore no effect on the interpretation to follow.

Effect of Strain-Stiffening on Crease Onset

Jin and Suo[50] predict that decreased J_{lim} delays the onset of creasing for a plane strain geometry. Numerical interpolation of these predictions yields a relation between J_{lim} and the critical strain, ε_c. (ESI†. Equation S1 is used for interpolation.) The latter is converted to a critical radius $a/A|_c$ using Eqn. (6.5). The resulting prediction of $a/A|_c$ as a function of J_{lim} (solid black line, Figure 6.4) describes the experimentally-measured dependence of crease onset on experimentally-determined J_{lim} well, with no fitting parameters. Notably, the measured J_{lim} of the 10:1 ratio falls near the asymptotic region ($J_{lim} = 3.1$) and the scatter in the crease onset measurements reflect this behavior.

6.4.3 Crease Morphology and Evolution

We find that differences in crease morphology are primarily due to the strain-stiffening material response. As summarized at the beginning of section 6.4.2 and illustrated in Figure 6.3, the number of creases near onset increases with increased mixing ratio. We observe that lower modulus, neo-Hookean samples (17.5:1 and 25:1) initially produce short creases distributed across the cavity surface (Fig. 6.3, top two rows). Conversely, high modulus, strain-stiffening samples (12:1 and 10:1) crease in one to three locations (Fig. 6.3, bottom two rows). All compositions tend toward similar creased shape at greater losses of cavity volume, $1 - V/V_0$. However, the mechanism by which these final shapes form differs with composition as well. The short initial creases join together as they increase in density (with

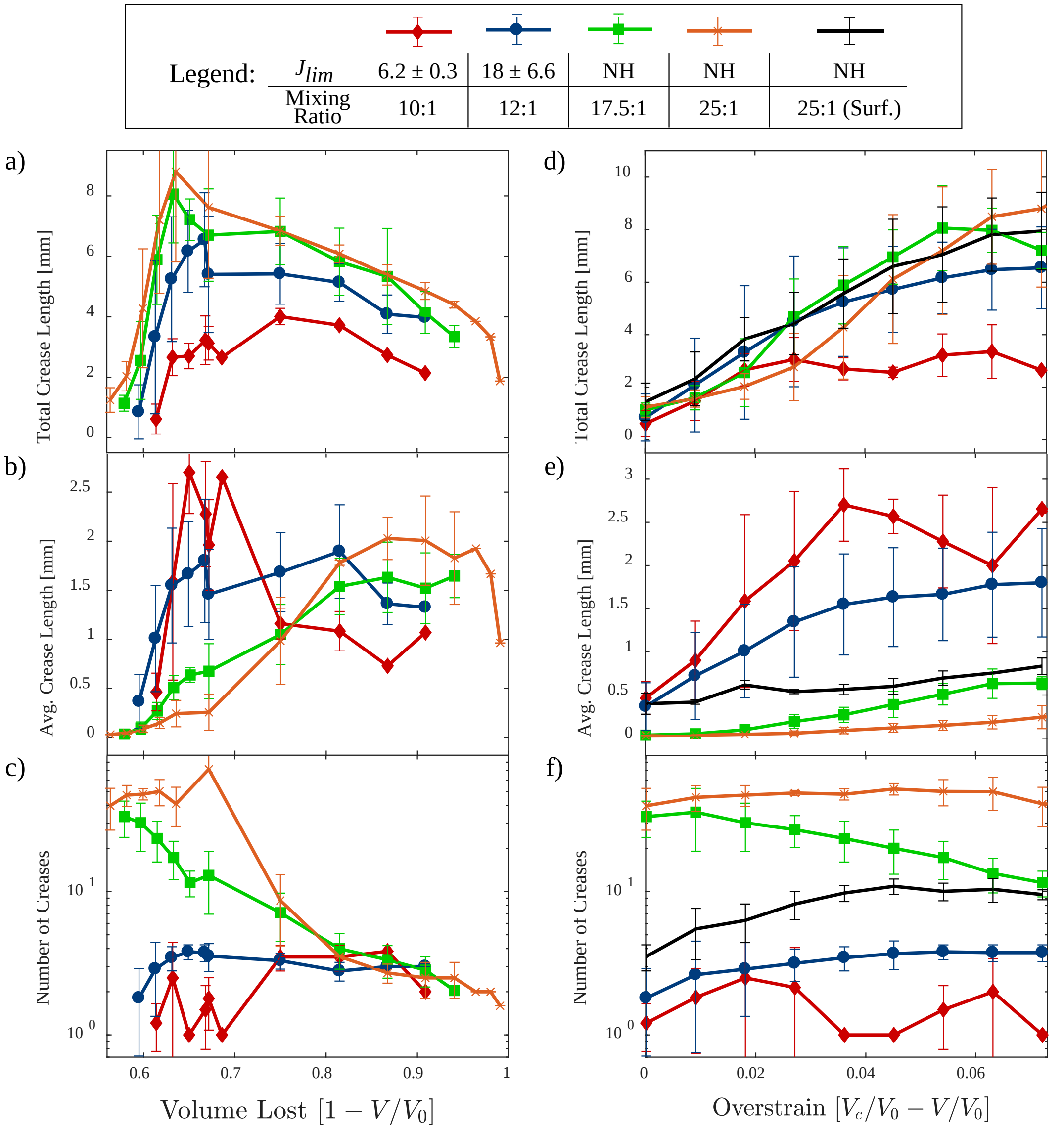

Figure 6.6 Quantified crease morphology evolution. Quantities are plotted as a function of normalized cavity volume loss $(1 - V/V_0)$ and overstrain as calculated using the average of the experimentally observed point of crease onset. Each curve corresponds to an averaging across five or more cavity deformations. Total crease length, a) and d), is the sum of all measured crease lengths. Average crease length, b) and e) is determined on a per cavity basis before averaging across droplets. Number of Creases, c) and f), is a simple counting of the number of crease lengths measured. Crease measurements are extrapolated to the entire cavity surface based on measurements of half of the surface. Data is given for the following mixing ratios: 10:1 (red diamonds), 12:1 (blue circles), 17.5:1 (green squares), and 25:1 (orange ×'s). The right column, d) - f), includes crease data for a surfactant droplet within a 25:1 mixing ratio elastomer and illustrates the minimal influence of decreased surface energy at low overstrain.

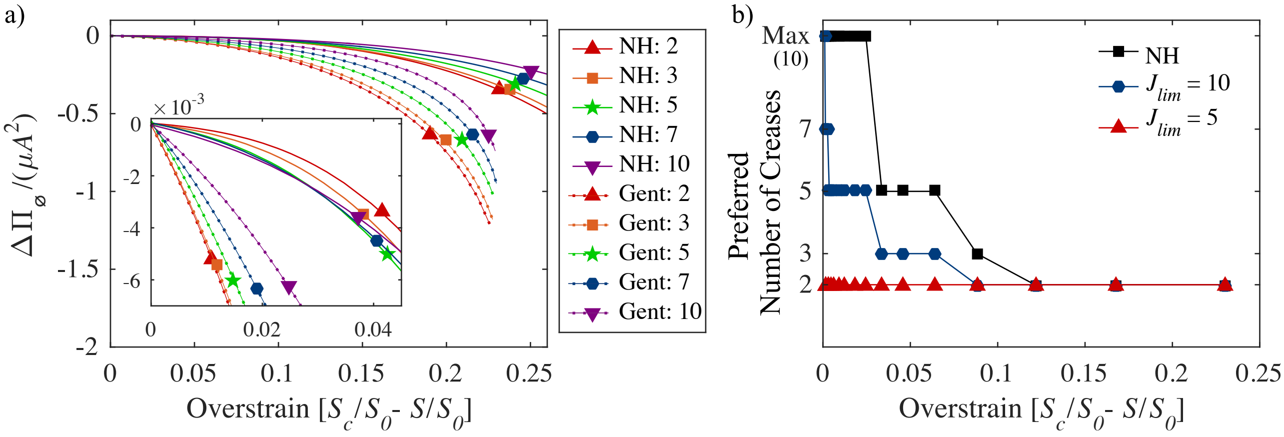

Figure 6.7 Simulated results for crease number trends for a cylindrical tube. a) $f(S - S_c)$ from Eqns. (6.8) and (6.9) as a function of normalized cylindrical overstrain, $S_c/S_0 - S/S_0$ where $S_0 = \pi A^2$, for neo-Hookean (solid lines) and Gent ($J_{lim} = 5$, dotted lines) material behaviors. The inset illustrates that near crease onset, $S_c - S = 0$, a free energetic preference for the largest number of creases simulated (10) exists for a neo-Hookean response. This is in opposition to a preference for the fewest number of creases simulated (2) for the $J_{lim} = 5$ response. At high overstrain, both behaviors prefer the fewest number of creases. b) The progression of free energetically-preferred crease number among those simulated for neo-Hookean (black squares), $J_{lim} = 10$ (blue circles), and $J_{lim} = 5$ (red triangles). These trends for the cylindrical geometry match those observed in spherical cavities (Figs. 6.3 and 6.6).

only small increases in length), eventually giving rise to a few creases that nearly span the cavity's surface. The fewer, longer creases channel across the cavity's surface (Fig. 6.3, bottom two rows). (Time-lapse videos illustrating these dynamics for each composition are available in the SI†.) The plots in Figure 6.6 quantify this morphology variation with sample composition. Data is obtained via human-eye, automated in Matlab; each crease is digitally traced on one half of the cavity (SI†). We note that this quantification technique fails to account exactly for increases in length due to surface curvature and encounters difficulty in resolving the smallest creases near crease onset. The former issue will not change our results as the error in using the 2-D projection is expected to be on the order of $2/\pi - 1 \approx 40\%$, whereas the scatter in our length data is on the order of 100%. The latter issue only applies to the first $1 - V/V_0$ value. This data is essential to performing a comparison with simulated crease morphologies.

A trend toward decreasing number of creases (decreased density) accompanying an increase in applied strain has been both predicted[49] and observed[49,102] for cylindrical and planar geometries in neo-Hookean materials. A similar trend is followed in the spherical geometry characterized here for the low modulus, neo-Hookean materials as shown in Fig. 6.6c. In contrast, strain-stiffening elastomers initiate few creases at low applied deformation and those creases channel across the surface with increasing deformation. Visually, the strain-stiffening creases appear deeper than those in the neo-Hookean materials. This supposition is supported by the observation that the total length of all creases combined is lower in strain-stiffening solids versus neo-Hookean solids under the same deformation, $1 - V/V_0$ (Fig. 6.6a). The strain must be accommodated through increased crease depth. To compare 'near-onset' effects we use an overstrain term, $V_c/V_0 - V/V_0$, similar to that in Chen et al.[103] (Fig. 6.6e-f). Doing so, we observe that creases in 25:1 samples initiate approximately ten times more frequently with around one tenth the length of creases in 10:1 samples (Fig. 6.6e-f). The mechanism leading to these crease morphology changes with increasing strain-stiffening will be explained through a combination of existing models of crease evolution.

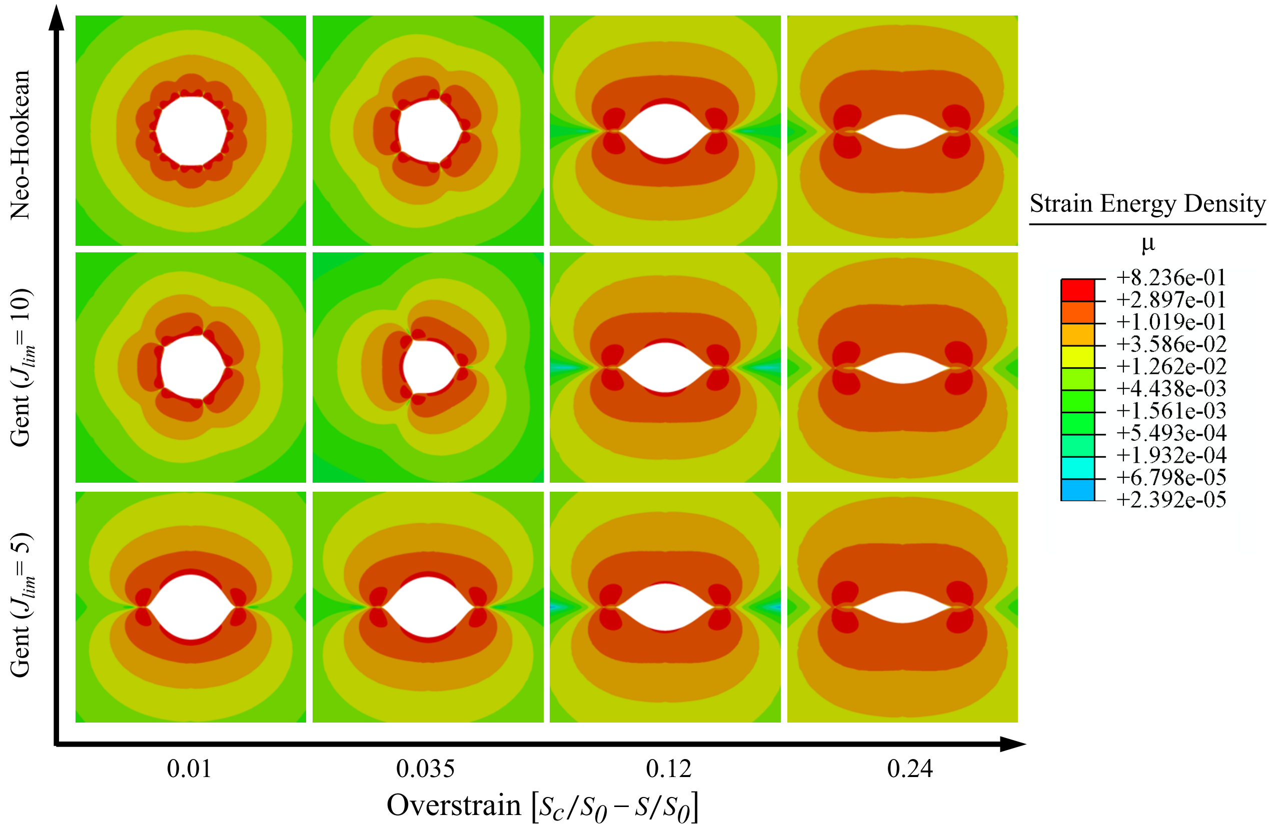

Figure 6.8 Cavities in neo-Hookean (top row), $J_{lim} = 10$ (middle row), and $J_{lim} = 5$ (bottom row) materials undergoing increasing deformation. Strain energy density contours are plotted for energetically-preferred crease number at each overstrain value.

Crease Spacing in Gent and Neo-Hookean Materials

Finite element analysis has been used previously to predict crease onset and model crease morphology in planar[101,102] and radially symmetric geometries.[49,107] Here, we show qualitative similarity between the energetically preferred number of creases in a simulated cylindrical cavity and our experimental observations as a function of material behavior. These calculations provide evidence that the observed morphological variation is primarily due to the material's strain-stiffening response.

We performed finite element simulations of cylindrical cavities in ABAQUS using neo-Hookean and Gent[50] constitutive models in order to calculate strain energy. This cylindrical cavity approximation provides a qualitative description of the observed phenomena while avoiding complexity associated with fully three-dimensional crease simulation[108,130] or the selection of experimentally inapplicable boundary conditions associated with a planar simulation (ratio of film width to height). The energetically preferred number of creases is determined by finding the minimum strain energy among simulations containing periodically-spaced numbers of creases ranging from 2 to 10. Creases are initiated at small geometric defects. Following Cai et al.,[49,102] the strain energy per unit thickness of the creased state relative to a homogeneously deformed uncreased state undergoing the same outer surface displacement (Eqn. (6.19)) takes the form

$$\Delta\Pi = \mu A^2 f(S), \tag{6.8}$$

where A in this case refers to the initial cylindrical cavity radius and S is the cylindrical cavity's area. $f(S)$ is obtained from subtracting the analytically obtained strain energy of homogeneous deformation (SI 6.7.2) from the strain energy calculated in ABAQUS. Figure 6.7a compares $f(S)$ between a neo-Hookean and Gent material behavior ($J_{lim} = 5$) plotted as a function of the cylindrical overstrain, i.e., the departure from the area at which crease onset occurs, $S_c - S$. Neo-Hookean results agree qualitatively with earlier simulations by Cai et al.[49] (who used a different ratio of outer to inner boundary radii). Gent curves are cut-off at high overstrains due to an exponential increase in the homogeneous strain energy as the limiting stretch is approached; this leads to imaginary values of $\Delta\Pi$ at overstrains available to the creased state, but unavailable to the homogeneous state. The inset in Figure 6.7a illustrates an energetic preference for the maximum number of creases simulated in neo-Hookean materials (purple inverted-triangle, solid line). In contrast, for a Gent material having $J_{lim} = 5$, the preferred number of creases is two just after onset. Note that in order to construct this comparison, the strain energy at crease onset is set to zero via

$$\Delta\Pi_{\o} = \Delta\Pi - \Delta\Pi\left(\frac{a}{A}\bigg|_c\right). \tag{6.9}$$

Crease onset in the cylindrical geometry is determined using previously calculated critical strains for plane strain[50,101] (Eqn. (6.12)), following Cai et al.[49] (SI 6.7.1). Without performing this zeroing operation, small numerical errors due to the presence of an initial defect lead to crease-number-related error near crease onset. This numerical error originates prior to creasing due to the presence of the defect and becomes similar in magnitude to free energy differences due just after crease onset. This numerical variation would be eliminated for an infinitesimally small initial defect. (SI†. Figure 6.15 demonstrates the trend toward zero $\Delta\Pi$ at crease onset for decreasing defect size.) Figure 6.7b summarizes the preferred number of creases among those values simulated (2, 3, 5, 7, 10) for a neo-Hookean solid (black squares), Gent material with $J_{lim} = 10$ (blue circles), and Gent materials with $J_{lim} = 5$. In agreement with experimental observation of spherical cavities, materials initiate creasing with fewer number of creases the earlier onset of strain-stiffening occurs, i.e., lower J_{lim}. This result is visualized in Figure 6.8. Given the lengthy deformation zone in which the maximum number of creases simulated is energetically preferred for the neo-Hookean solid, we believe an energetic minimum likely occurs at an even larger number of creases.

Limited Role of Surface Energy

Crease growth via channeling has been previously shown to arrest or propagate based on elastocapillary control.[103] Low elastocapillary numbers, $\gamma/\mu L$, and therefore creases that more readily channel are achieved with either high moduli or low surface energies. Estimation of the elastocapillary number for this system, where the relevant length scale L is taken to be the initial cavity radius, $A = 1.5$ mm, yields a range from 4.1×10^{-5} (10:1) to 3.7×10^{-4} (25:1). Within this regime, surface energy should play a negligible role and surface energy should provide no barrier to channeling. However, we observe little channeling in the softest compositions. Even an order of magnitude change in surface energy should have no effect. To test the assumption that initial cavity radius, A, was the appropriate length scale, we changed the surface energy while keeping composition constant, similar to Chen et al.[103]

Liquid drops embedded in 25:1 Sylgard were altered through the addition of the surfactant 3-[hydro(polyethyleneoxy) propyl] heptamethyltrisiloxane (Gelest) above its critical micelle concentration.[131,4] Interestingly, as reported by Chen et al.,[103] creases formed un-

---

[4] Concerns of surfactant migration into the uncured necessitated an increase in curing temperature and reduc-

der the effect of surfactant channeled further than those in non-surfactant cavities at low overstrain (Figures 6.6e-f and Figure 6.9). The morphology of these 25:1/surfactant systems more closely resembles that in the 10:1 and 12:1 mixing ratios immediately after crease onset. To understand this effect, we estimate the elastocapillary length scales for 25:1/water, 25:1/surfactant, and 10:1/water as 550 nm, 6.5 nm, and 61 nm, respectively ($\mu_{10:1} = 0.65 \pm 0.04$ MPa, $\mu_{25:1} = 0.073 \pm 0.004$ MPa, $\gamma_{H_2O} = 40$ mN/m, $\gamma_{\mathrm{surf}} = 0.5$ mN/m[103]). It appears that this length scale in the surfactant cavity approaches that of the 10:1/water system, mirroring the approach of surfactant cavity morphology to that of the 10:1 cavity.[5] This result indicates that crease size, as opposed to system geometry, may be the governing length scale for calculation of the elastocapillary number in the initial stages of creasing. Using previously determined experimental values for the crease depth ($d \sim 20$ μm from Cai et al.[102]) as as estimate for the length scale, L, the elastocapillary numbers for 25:1/water, 25:1/surfactant, and 10:1/water systems are 0.07, 9×10^{-4}, and 5×10^{-3}, respectively. The elastocapillary number for the 25:1/water system is within the range reported by Chen et al.[103] as having elastocapillary governed channeling. Therefore, while surface energy does not predominately account for the morphology differences observed here, it is interesting to note its role in a system for which it would typically be considered negligible.

6.4.4 Cavitation and Surface 'Bubble' Formation

All cavities expand to an unloaded state upon cavitation of the embedded liquid. Upon cavitation, the sudden release of load at the cavity surface is accompanied by rapid oscillatory deformation (see video in SI†) until the final unloaded state is reached. We observe a higher proportion of cavities achieving large, creased deformation in the lower modulus formulations as opposed to the highest modulus formulation (Table 6.2†). The reason for early onset of cavitation in the stiffest mixing ratio (10:1) is likely that for the same loss of droplet volume, a stiffer material will produce a higher hydrostatic tension in the droplet. This higher tension leads to a higher probability of cavitation.[132] A few, statistically in-

---

tion in curing time, 150°C and 10 min. As a control, pure water cavities in rapidly cured 25:1 polymer behaved identically to those created using the slower curing conditions reported above.

[5] Large deformations in surfactant cavities were not observed, likely due to early cavitation facilitated by the presence of surfactant.

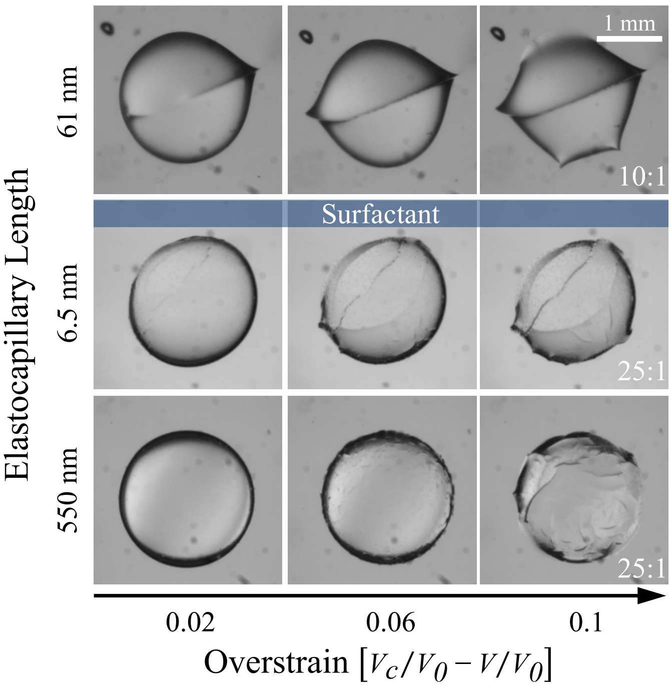

Figure 6.9 Surface Energy Effects. The reduction of surface energy due to the addition of surfactant (middle row) within droplets embedded in low modulus materials (middle and bottom rows) enabled more channeling, similar to the highest modulus, strain-stiffening materials (top row). Columns compare cavity deformation at identical values of overstrain.

significant, cavities within the softest formulation (25:1) cavitated early. The reason for this remains unclear, though it may be due to the increased number of creases or silicone 'microbubbles' (see next paragraph) in those cavities that lead to more sites for heterogeneous nucleation. The cavitation behavior of this system is left for future study.

Another phenomena observed during cavity contraction is the formation of 'microbubbles' at the PDMS-water interface (Fig. 6.13†). These structures grow in size as deformation increases, eventually appearing to coalesce, and are more prominent in the stiffer elastomer formulations. Such microbubbles would lead to cavitation if they were water vapor or would require any gas within them to be under tension if they were air. We therefore suggest that they might be formed from squeezing small volumes of un-crosslinked silicone[133] out of the bulk of the PDMS. Similarly, silicone nanobubbles have been observed to coalesce in PDMS-water mixtures.[134] Given our primarily continuum mechanics, negligible surface energy description of the observed creasing phenomena, these fluid bubbles are expected to have minimal effect on the results reported herein.

6.5 Conclusions

We observe the contraction, creasing, and cavitation of a liquid-filled spherical cavity within an elastomer. Deformation is driven by evaporation. For elastomer compositions that exhibit strain-stiffening as modeled by the Gent relation, the onset of creasing follows recent theoretical predictions, namely that strain-stiffening at lower stretch values increases the compressive strain required to initiate creasing. After crease onset, increasing deformation is quantified by extrapolating the results of a diffusive mass transport model for the liquid within the cavity. This assumption establishes a basis of cavity volume with which to compare crease morphologies between compositions. We then qualitatively describe differences in the time-evolution of crease morphology by drawing a parallel with plane strain creasing of a simulated cylindrical cavity. In both simulation and experiment:

- The deformation at which crease onset occurs depends on strain-stiffening.
- Neo-Hookean solids have an energetic preference for many creases near crease onset.

- The number of creases near onset decreases with decreasing J_{lim}. (In the Gent model, J_{lim} characterizes strain at onset of stiffening.)
- All material behaviors tend toward similar crease numbers at large overstrain.

These results experimentally validate the important role that strain-stiffening plays in determining crease morphology in this contracting cavity system. It follows that strain-stiffening may be a critical consideration in predicting biologically relevant crease morphologies in other geometries.[107,108,112]

6.6 Acknowledgments

The authors would like to acknowledge Shenqiang Cai for his helpful insight of creasing behavior and Abe Stroock for his thoughtful suggestions relating to fluids under tension. Matt and Shelby also acknowledge start-up funding provided by the Mechanical Science and Engineering Department at UIUC.

6.7 Supplementary Information

6.7.1 Crease Onset

The critical condition for the onset of creasing in a planar sample under plane strain conditions is calculated by Hong et al.[101] who wrote it more generally as

$$\frac{\lambda_3}{\lambda_1} = (1-\varepsilon_c)^{-2}, \tag{6.10}$$

where ε_c refers to the critical strain value, λ_1 is the stretch parallel to the applied deformation and λ_3 is the stretch perpendicular to the applied deformation. In a spherical geometry the principal circumferential stretches are given by $\lambda_1 = \lambda_2 = r/R$. r and R are the deformed and undeformed coordinates within the material. For an incompressible solid, $\lambda_1\lambda_2\lambda_3 = 1$, then $\lambda_3 = (R/r)^2$. At the surface of the cavity, $r = a$ and $R = A$. Applying these definitions of stretch to (6.10), a/A at crease onset is given by

$$\left.\frac{a}{A}\right|_c = (1-\varepsilon_c)^{2/3}. \tag{6.11}$$

Similarly, in a cylindrical geometry under plane strain conditions, the principal stretches are $\lambda_1 = r/R$, the circumferential stretch, $\lambda_2 = 1$, the longitudinal stretch, and $\lambda_3 = R/r$, the radial stretch. Following the same procedure as above, a/A at crease onset in the cylindrical geometry is

$$\left.\frac{a}{A}\right|_c = (1-\varepsilon_c). \tag{6.12}$$

6.7.2 Homogeneous Cylinder Deformation

The strain energy per unit thickness associated with the homogeneous contraction of a cylindrical cavity of initial inner radius, A, within a cylinder having outer radius, B is determined by integrating the strain energy density, W, over the entire solid region.

$$\Pi = \int_0^{2\pi}\int_a^b W(r)rdrd\theta, \tag{6.13}$$

where a is the deformed cavity radius, b is the deformed outer radius, and r and θ define the deformed coordinate system within the solid. Under the assumptions of incompressibility and plane strain ($\lambda_z = 1$), the area within any annulus of undeformed material $R^2 - A^2$ must equal the area within that deformed annulus, $r^2 - a^2$.

$$r^2 - a^2 = R^2 - A^2 \tag{6.14}$$

When the radii of the initial and deformed void are known, the field of deformation is determined by this equality. The circumferential stretch, λ_θ is

$$\lambda_\theta = r/R = \lambda. \tag{6.15}$$

Here we introduce a dimensionless stretch parameter, λ. Incompressibility relates $\lambda_r\lambda_\theta\lambda_z = \lambda_r\lambda_\theta = 1$ such that

$$\lambda_r = R/r = 1/\lambda. \tag{6.16}$$

For the strain energy density as a function of J, J can then be written

$$J = \lambda^2 + \lambda^{-2} - 2 \tag{6.17}$$

Using Eqn. (6.14), r can be re-written as a function of λ,

$$r = (a^2 - A^2)^{1/2}(1 - \lambda^{-2})^{-1/2}. \tag{6.18}$$

Re-expressing the strain energy integral in Eqn. (6.13) in terms of λ, substituting Eqn. (6.17) for J, and integrating over θ yields.

$$\Pi = 2\pi(A^2 - a^2)\int_{a/A}^{b/B} \frac{\lambda W(\lambda)}{(1-\lambda^2)^2} d\lambda. \tag{6.19}$$

Eqn. (6.19) is solved analytically for a neo-Hookean strain energy function and numerically for the Gent strain energy function (Eqn. (6.6)).

6.7.3 Characterization of Sylgard 184 at Room Temperature and Hydrated at 60 °C

Constitutive model parameters for Sylgard 184 under heated (60 °C), hydrated conditions are compared to those at room temperature in Table 6.1. For all mixing ratios the shear modulus is higher in the heated and hydrated sample. Of the J_{lim} values determined, only the 10:1 mixing ratio showed a statistically significant variation with environment (single factor, ANOVA, $F_{ratio} > 1$). However, the variation was small, only decreasing by 11%.

6.7.4 Quantification of Crease Morphology

Crease data is gathered from a time series of optical images. Creases in cavity surfaces were digitally traced by hand via a series of line segments using a routine written in Matlab.

Table 6.1 Shear moduli (μ) and strain hardening (J_{lim}) fit parameters from Eqn. 7 are reported for Sylgard 184 hydrated at 60 °C (H) and at room temperature (RT). The F_{ratio} from single factor ANOVA is given for the 10:1 and 12:1 mixing ratios.

Mixing Ratio	$\mu_H\,[MPa]$	$\mu_{RT}\,[MPa]$	J_{lim_H}	$J_{lim_{RT}}$	$F_{ratio,J_{lim}}$
10:1	0.55 ± 0.036	0.44 ± 0.042	6.2 ± 0.32	7.0 ± 0.62	1.25
12:1	0.39 ± 0.035	0.31 ± 0.022	18.1 ± 6.6	17.8 ± 6.7	0.001
17.5:1	0.20 ± 0.009	0.11 ± 0.019	NH	NH	N/A
25:1	0.073 ± 0.004	0.028 ± 0.004	NH	NH	N/A

Examples of digitized creases are shown for 10:1 and 25:1 mixing ratios in Figure 6.10. Continuous segments were counted as a single crease having a total length equal to the sum of the segment lengths. For cavities having large numbers of creases (e.g., 25:1 in Fig. 6.10), only half of the visible surface is characterized and the total cavity statistics is determined by extrapolating to the remaining surface area (multiplying by 4). For all other cavities, the creases characterized on the one visible half are doubled to obtain the full cavity 'total crease length' and 'number of creases' plotted in Figure 6.

6.7.5 Cavitation Event Frequency

While rarely a cavity will deform to the point of becoming optically invisible (i.e., completely closed), not all cavities deform by large amounts. Occasionally, the liquid droplet cavitates before onset of creasing or shortly thereafter. Table 6.2 quantifies the frequency of early cavitation among the compositions tested. Droplets in the 10:1 mixing ratio have a relatively higher probability of cavitation shortly after creasing, which may be due to the higher pressure attained as compared to the droplets in the other mixing ratios.[132]

*One droplet completely closed.

6.7.6 Crease Onset Interpolation

The critical strain for creasing can only be obtained via simulation using very small defect size as performed previously by Jin and Suo.[50] Using the results from their work relating crease onset, ε_c, to J_{lim} (Fig. 6.11, black squares), we interpolated to determine crease onset

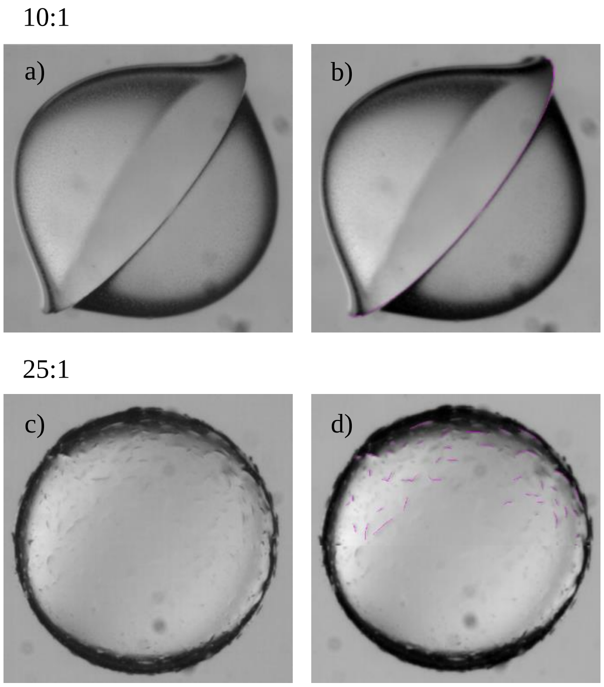

Figure 6.10 Example crease images for 10:1 (a) and 25:1 (c) mixing ratios. Digitized creases are highlighted with magenta lines for the entire single crease (b) and, in the case of high crease number density, the upper half of the visible surface (d).

strains for experimentally measured J_{lim} values. These simulation data are fit via:

$$J_{lim} = A\exp\left(Bx^4\right) + \frac{C}{(x-0.35)^2} + 3.1 \tag{6.20}$$

The form of equation 6.20 was selected due to its ability to capture the limiting behaviors previously observed. That is, it predicts a neo-Hookean crease onset value as $J_{lim} \rightarrow \infty$ and predicts crease suppression as $J_{lim} \rightarrow 3.1$. The fit parameters, determined via least squares, are: $A = 415.5$, $B = -246.3$, $C = 3.469 \times 10^{-4}$.

6.7.7 Strain Hardening

A given strain hardening parameter, J_{lim}, corresponds to a specific limiting deformation state, depending on the type of loading. The stretch at which strain hardening occurs under

Table 6.2 Number of droplets cavitating before creasing, shortly after creasing, or well after creasing for each observed mixing ratio. Droplets can take up to 48 hours to cavitate after creasing.

Mixing Ratio	Cavitation Before Creasing	Cavitation ≤ 4 hrs Post Crease	Cavitation > 4 hours Post Crease
10:1	3	4	2
12:1	1	0	5
17.5:1	0	0	8
25:1	1	2	4*

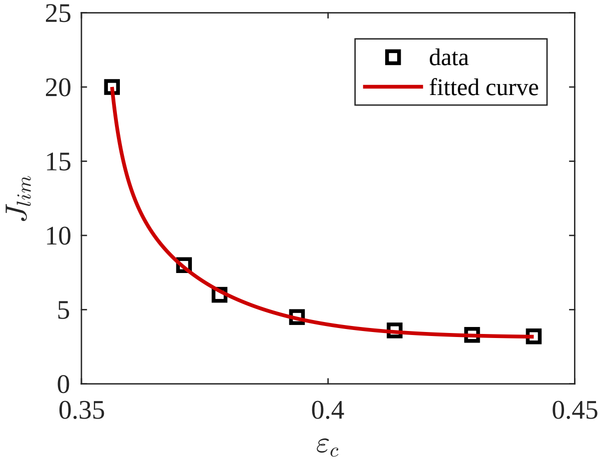

Figure 6.11 Data (black squares) of predicted crease onset from Jin and Suo[50] fit to Equation 6.21.

equi-biaxial deformation is shown in Figure 6.12 and given by the expression:

$$J_{lim} = 2\lambda_{lim}^2 + \lambda_{lim}^{-4} - 3 \tag{6.21}$$

6.7.8 ‘Microbubbles’ on Void Surface

Small ‘bubbles’ appear on the surface of the cavities shortly before creasing. Figure 6.13 provides typical close-up images of the ‘bubbles,’ thought to be un-crosslinked silicone polymer extracted from the bulk polymer due to the high tensile loads in the water and large compressive deformations at the cavity surface.

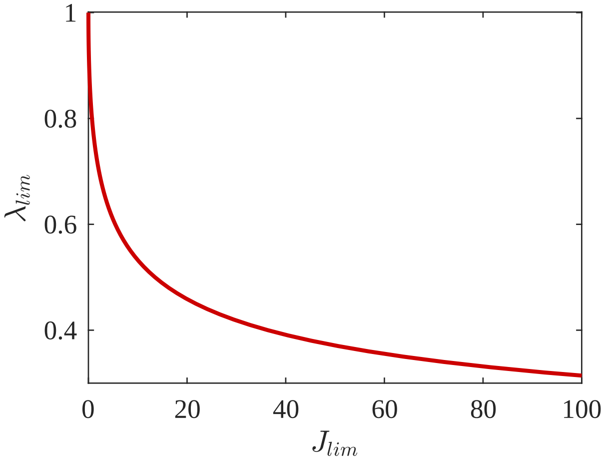

Figure 6.12 Corresponding limiting stretch value, λ_{lim} for a given J_{lim}.

6.7.9 Finite Element Simulation

A cavity of radius A within a cylinder of outer radius $B = 10A$ is used to approximate the deformation observed in liquid-filled cavities. The ratio $B/A = 10$ was selected because it approximates the experimental geometry. Figure 6.14 illustrates the full geometry, defect geometry, and typical mesh refinement used throughout the reported simulations. Element sizes varied from approximately $10^{-4}A$ near the defect to $0.5A$ at the outer, traction-free boundary. A mesh convergence study on a neo-Hookean material having two creases (Fig. 6.15a) demonstrates that near crease onset, error in the strain energy, $\Delta\Pi/(\mu A^2)$ is anticipated to be on the order of 1×10^{-5}. A stronger dependence on strain energy near crease onset is found for defect size (Fig. 6.15b). For ease of convergence, particularly in the case of the Gent material response, we use a defect size of $A/100$ throughout. We zero the strain energy by subtracting the small energy value at crease onset as described in section 3.3.1 in order to extract the energetic minimum as a function of crease number.

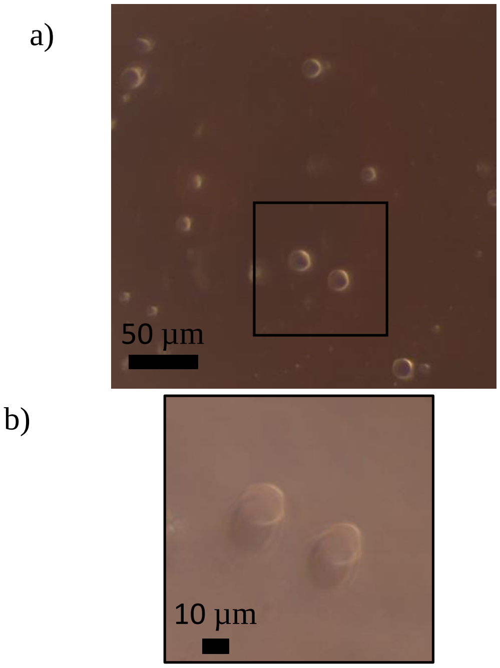

Figure 6.13 Optical micrographs of the ‘microbubbles’ at the surface of a cavity within a 10:1 sample. a) The bubbles appear on about 5% of the surface and the magnified region b) A close up of the micron-sized bubbles.

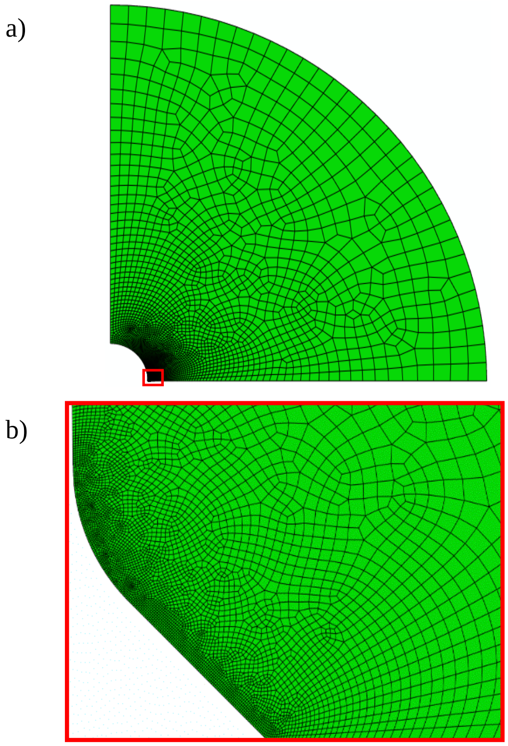

Figure 6.14 Typical meshing used in FE simulation. a) The meshed cylindrical annulus showing refinement near the cavity surface. b) A close-up of the $A/100$-sized defect, typical for all crease numbers simulated.

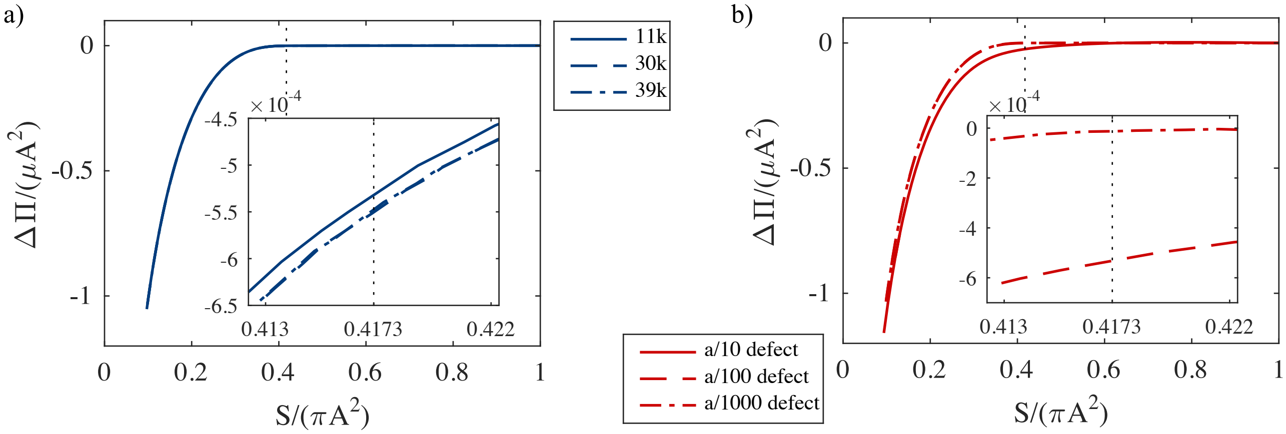

Figure 6.15 Results from convergence studies of mesh refinement (a) and defect size (b) for a two crease geometry having a neo-Hookean material model. Crease onset in both figures is denoted with a vertical dotted line. a) Calculations were performed with 11k (solid), 30k (dashed), and 39k (dash-dot) elements corresponding to approximate element sizes of $A \times 10^{-4}$, $8A \times 10^{-5}$, and $7A \times 10^{-5}$, respectively around the defect. An $A/100$ size defect was used. b) Calculations using decreasing defect size show a strong dependence of strain energy near crease onset (as determined by previous simulation[50,101]). Smaller defects approach a strain energy of zero at crease onset.

Chapter 7

Summary and Outlooks

This dissertation focused on the use of spherical deformations to study the characteristics of soft-solids that govern the onset of localized deformations in both high-rate expansions, leading to fracture, and in quasi-static contractions, leading to creases. By utilizing bubble-like deformations within the bulk of soft-solid samples, several difficulties in handling these low stiffness and fragile materials can be avoided. Conducting these experiments at high-rate required development of a new testing apparatus, the Small-scale Ballistic Cavitation device. This device addresses the ability to independently tune expansion rate, mass transfer, energy delivered, and initial defect size during a high rate cavitation; a degree of control that was lacking in other contemporary high rate cavitation techniques. Using this device and related pressure-driven cavity expansion methods, I provided evidence for a fracture theory explaining multiple crack onset. By simply counting the number of cracks around an expanding cavity, I have shown that fracture energies may be estimated if the modulus strain rate dependence of the material is known. The fracture response of low toughness PDMS and gelatin formulations were well approximated by a linear constitutive response and I reported fracture energies of these materials. I also provided a framework for the interpretation of crack formation in tougher materials that may require a nonlinear and strain stiffening constitutive response. Both theories incorporate the effects of acoustoelasticity as a function of strain rate, but the nonlinear theory additionally accounts for acoustoelastic changes as a function of strain. Ballistic impacts from several bullet types were analyzed using the reported strain rate dependent fracture energy trends and predictions on finding an appropriate radius of expansion to enable use of the multiple fracture phenomenon in future material characterization were shown. I proposed a method, consistent with fracture mechanics physics, to analyze damage generation by accounting for the Total Crack Area. Finally, I showed that localized deformations in spherical contractions can be used to analyze nonlinear stiffening by observing crease onset and morphology.

This work found self-consistent results for predicted values of the fracture energy in brittle soft-solids by observing the number of cracks forming around a high-rate expansion; however, both the effect of the needle size and amount of retraction were found to be important considerations in the exact magnitude of the fracture energies. While this is consistent with other published studies, the magnitude of the change in approximate initial cavity size needs to be further examined to understand the damage created by needle insertion. A potential method to avoid this difficulty would be to insert the SBC needle into embedded defects of predetermined sizes to perform the cavitation, due to the SBC device's tunable strain rate, different-sized defects may be expanded at similar rates. This would allow for a systematic study of initial cavity radius on crack numbers. There are some limitations to using the number of cracks as an observable for extracting fracture energy. The minimum number of cracks observable is two and the maximum depends on the experimental ability to observe crack tips around a needle. As the number of cracks measured increases, so to does the precision of the resulting fracture energy. It is also possible that as toughness is reduced cracks form in directions other than in the direction of the needle, which could block crack observation. Since crack counting The utility of crack counting is a simple method to characterize fracture energy; however, it relies on previously reported high-rate constitutive response information. Characterizing similar soft-solids will require continued adaptation of traditional techniques to measure the constitutive response. Alternatively, this work demonstrated the utility of spherical deformations and should therefore be explored further as a means of constitutive characterization. This would likely require high-rate, full-field strain measurements perhaps by using particle tracking velocimetry. The current high-rate imaging techniques are unable to provide the resolution required for these measurements.

In applying the multiple fracture characterization technique to other materials, crack-counting was only possible *in-situ*, due to the optically transparent nature of the materials. However, CT imaging of fractured surfaces, as was shown in this work, could be a viable avenue for characterization of cracks around the cavities, if the rate of expansion could be approximated. This would first require analysis of crack morphology throughout the entire expansion process, as crack numbers may change if they coalesce or branch. Alternatively, this could be avoided if the entire expansion is limited to small expansion ratios, just enough to initiate cracks and then cease driving forces. Experimentation and crack morphology analysis on stiffening, tough soft-solids will surely provide interesting results within the context of the nonlinear theory presented here. As the toughness increases, the number of cracks around an expanding cavity would decrease, which could be remedied by increasing the needle. However, there is a balance that will be made with increasing the needle size as doing so increases the chance of coring the sample and plugging the needle.

Analyzing ballistic impacts with an approach, the Total Crack Area method, consistent with the physics of cavity formation and fracture mechanics should rectify present discrepancies reported between different bullet types and damage. Damage should depend on the bullet type but the material's constitutive and fracture response should always be consistent, as demonstrated by the needle-mediated cavitations. My ballistic analysis results show consistency, but further work is needed with a systematic variation of projectile form factors to concretize the method. The next step would be to broaden experiments to deforming bullets. The radius of expansion for a given bullet for different bullet types needs investigation. The fracture theory presented here is sensitive to that radius. The rate dependence of the fracture response should also be investigated with very high kinetic energy magnum rounds (typical of hunting rifles); however, as the size of the cavitation increases, larger targets than the standard-sized ballistic gelatin are required to reduce boundary effects and maintain consistent results with lower kinetic energy impacts.

Chapter 8

Bibliography

[1] Jessica A. Zimberlin, Naomi Sanabria-DeLong, Gregory N. Tew, and Alfred J. Crosby. Cavitation rheology for soft materials. *Soft Matter*, 3(6):763, 2007. ISSN 1744-683X. doi: 10.1039/b617050a.

[2] Santanu Kundu and Alfred J. Crosby. Cavitation and fracture behavior of polyacrylamide hydrogels. *Soft Matter*, 5(20):3963–3968, 2009. ISSN 1744683X. doi: 10.1039/b909237d.

[3] Shelby B. Hutchens, Sami Fakhouri, and Alfred J. Crosby. Elastic cavitation and fracture via injection. *Soft Matter*, 12(9):2557–2566, 2016. ISSN 1744-683X. doi: 10.1039/C5SM02055G. URL `http://xlink.rsc.org/?DOI=C5SM02055G`.

[4] Shabnam Raayai-Ardakani, Zhantao Chen, Darla Rachelle Earl, and Tal Cohen. Volume-controlled cavity expansion for probing of local elastic properties in soft materials. *Soft Matter*, 15:381–392, 2019. doi: 10.1039/C8SM02142B. URL `http://dx.doi.org/10.1039/C8SM02142B`.

[5] Shabnam Raayai-Ardakani, Darla Rachelle Earl, and Tal Cohen. The intimate relationship between cavitation and fracture. *Soft Matter*, 15(25):4999–5005, 2019. ISSN 17446848. doi: 10.1039/c9sm00570f.

[6] Xavier Poulain, Oscar Lopez-Pamies, and K. Ravi-Chandar. Damage in elastomers: Healing of internally nucleated cavities and micro-cracks. *Soft Matter*, 14(22):4633–4640, 2018. ISSN 17446848. doi: 10.1039/c8sm00238j.

[7] Victor Lefèvre, K. Ravi-Chandar, and Oscar Lopez-Pamies. Cavitation in rubber: an elastic instability or a fracture phenomenon? *International Journal of Fracture*, 192 (1):1–23, 2015. ISSN 15732673. doi: 10.1007/s10704-014-9982-0.

[8] X. Poulain, V. Lefèvre, O. Lopez-Pamies, and K. Ravi-Chandar. Damage in elastomers: nucleation and growth of cavities, micro-cracks, and macro-cracks. *International Journal of Fracture*, 205(1):1–21, 2017. ISSN 15732673. doi: 10.1007/s10704-016-0176-9.

[9] Jonathan B. Estrada, Carlos Barajas, David L. Henann, Eric Johnsen, and Christian Franck. High strain-rate soft material characterization via inertial cavitation. *Journal of the Mechanics and Physics of Solids*, 112: 291–317, mar 2018. ISSN 00225096. doi: 10.1016/j.jmps.2017.12.006. URL `https://doi.org/10.1016/j.jmps.2017.12.006https://linkinghub.elsevier.com/retrieve/pii/S0022509617307585`.

[10] Pooya Movahed, Wayne Kreider, Adam D. Maxwell, Shelby B. Hutchens, and Jonathan B. Freund. Cavitation-induced damage of soft materials by focused ultrasound bursts: A fracture-based bubble dynamics model. *The Journal of the Acoustical Society of America*, 140(2):1374–1386, aug 2016. ISSN 0001-4966. doi: 10.1121/1.4961364. URL `http://asa.scitation.org/doi/10.1121/1.4961364`.

[11] R. Hill. Cavitation and the influence of headshape in attack of thick targets by non-deforming projectiles†. *Journal of the Mechanics and Physics of Solids*, 28(5-6):249–263, 1980. ISSN 00225096. doi: 10.1016/0022-5096(80)90019-8.

[12] Rodney Hill. *The Mathematical Theory of Plasticity*. Oxford University Press, London, 1950.

[13] R F Bishop, R Hill, and N F Mott. The theory of indentation and hardness tests. *Proceedings of the Physical Society*, 57(3):147–159, may 1945. ISSN 0959-5309. doi: 10.1088/0959-5309/57/3/301. URL `http://stacks.iop.org/0959-5309/57/i=3/a=301?key=crossref.87e4865e16cf2f942e3e1b4a03becad8`.

[14] M.J. Forrestal, B.S. Altman, J.D. Cargile, and S.J. Hanchak. An empirical equation for penetration depth of ogive-nose projectiles into concrete targets. *International Journal of Impact Engineering*, 15(4):395–405, aug 1994. ISSN 0734743X. doi: 10.1016/0734-743X(94)80024-4. URL `https://linkinghub.elsevier.com/retrieve/pii/0734743X94800244`.

[15] V. K. Luk, M. J. Forrestal, and D. E. Amos. Dynamic Spherical Cavity Expansion of Strain-Hardening Materials. *Journal of Applied Mechanics*, 58(1):1, 1991. ISSN 00218936. doi: 10.1115/1.2897150. URL `http://appliedmechanics.asmedigitalcollection.asme.org/article.aspx?articleid=1410291`.

[16] M. J. Forrestal and V. K. Luk. Dynamic Spherical Cavity-Expansion in a Compressible Elastic-Plastic Solid. *Journal of Applied Mechanics*, 55(2):275, 1988. ISSN 00218936. doi: 10.1115/1.3173672. URL `http://appliedmechanics.asmedigitalcollection.asme.org/article.aspx?articleid=1409232`.

[17] Zvi Rosenberg and Erez Dekel. *Terminal ballistics, second edition*. 2016. ISBN 9789811003950. doi: 10.1007/978-981-10-0395-0.

[18] J.N. Goodier. On the Mechanics of Indentation and Cratering in Solid Targets of Strain-Hardening Metal by Impact of Hard and Soft Spheres. In *Proceedings of the 7th Symposium on Hypervelocity Impact III*, 1965.

[19] Thomas L Warren and Mazen R Tabbara. Spherical Cavity-Expansion Forcing Function in PRONTO 3D for Application to Penetration Problems. (May), 1997.

[20] Duncan MacPherson. *Bullet Penetration: Modeling the Dynamics and the Incapacitation Resulting from Wound Trauma*. Ballistic Publications, El Segundo, 2 edition, 2005. ISBN 0-9643577-1-2.

[21] Beat P. Kneubuehl, Robin M. Coupland, Markus A. Rothschild, and Michael J. Thali. *Wound ballistics: Basics and Applications*. Springer-Verlag, Berlin, 3 edition, 2011. ISBN 9783642203558.

[22] Li Liu, Yurun Fan, Wei Li, and Hongwei Liu. Cavity dynamics and drag force of high-speed penetration of rigid spheres into 10wt% gelatin. *International Journal of Impact Engineering*, 50:68–75, 2012. ISSN 0734743X. doi: 10.1016/j.ijimpeng.2012.06.004. URL `http://dx.doi.org/10.1016/j.ijimpeng.2012.06.004`.

[23] Li Liu, Zhen Jia, Xiaolin Ma, Yurun Fan, Wei Li, and Hongwei Liu. A spherical cavity expansion model of large elastic deformation and its application to ballistic gelatin penetration problems. *International Journal of Impact Engineering*, 71:106–116, 2014. ISSN 0734743X. doi: 10.1016/j.ijimpeng.2014.04.007. URL `http://dx.doi.org/10.1016/j.ijimpeng.2014.04.007`.

[24] J Jussila. *Wound ballistic simulation: Assessment of the legitimacy of law enforcement firearms*. 2004. ISBN 9529180004. URL `http://www.gutenberg.org/etext/12128{%}5Cnpapers3://publication/uuid/4DD5A793-5E58-4316-A5AE-E1AAE454FBFC`.

[25] Matt P. Milner and Shelby B. Hutchens. A device to fracture soft solids at high speeds. *Extreme Mechanics Letters*, 28:69–75, apr 2019. ISSN 23524316. doi: 10.1016/j.eml.2019.02.007. URL `https://doi.org/10.1016/j.eml.2019.02.007https://linkinghub.elsevier.com/retrieve/pii/S2352431619300082`.

[26] J Winter and D Shifler. The material properties of gelatin gels. Technical report, 1975.

[27] Sung-ho Yoon and Clive R. Siviour. The Virtual Fields Method to Rubbers Under Medium Strain Rates. In *Conference Proceedings of the Society for Experimental Mechanics Series*, volume 3, pages 177–185. 2017. ISBN 978-3-319-63027-4. doi: 10.1007/978-3-319-41600-7_22. URL `http://link.springer.com/10.1007/978-3-319-63028-1http://link.springer.com/10.1007/978-3-319-41600-7{_}22`.

[28] S. Rao, V. P. W. Shim, and S. E. Quah. Dynamic mechanical properties of polyurethane elastomers using a nonmetallic Hopkinson bar. *Journal of Applied Polymer Science*, 66(4):619–631, 1997. ISSN 00218995. doi: 10.1002/(SICI)1097-4628(19971024)66:43.3.CO.

[29] D S Cronin, C P Salisbury, and C R Horst. High rate characterization of low impedance materials using a Polymeric Split Hopkinson Pressure Bar. *SEM Annual Conference and Exposition on Experimental and Applied Mechanics 2006, June 4, 2006 - June 7*, 1:314–322, 2006.

[30] Weinong W. Chen and Bo Song. Dynamic Characterization of Soft Materials. In *Dynamic Failure of Materials and Structures*, volume 1, pages 1–28. Springer US, Boston, MA, 2009. ISBN 9781441904454. doi: 10.1007/978-1-4419-0446-1_1. URL `http://link.springer.com/10.1007/978-1-4419-0446-1{_}1`.

[31] Gil Ho Yoon, Jun Su Mo, Ki Hyun Kim, Chung Hee Yoon, and Nam Hun Lim. Investigation of bullet penetration in ballistic gelatin via finite element simulation and experiment. *Journal of Mechanical Science and Technology*, 29(9):3747–3759, 2015. ISSN 1738494X. doi: 10.1007/s12206-015-0821-7.

[32] Stephan A. Bolliger, Michael J. Thali, Michael J. Bolliger, and Beat P. Kneubuehl. Gunshot energy transfer profile in ballistic gelatine, determined with computed tomography using the total crack length method. *International Journal of Legal Medicine*, 124 (6):613–616, 2010. ISSN 09379827. doi: 10.1007/s00414-010-0503-z.

[33] C. J. Shepherd, G. J. Appleby-Thomas, P. J. Hazell, and D. F. Allsop. The dynamic behaviour of ballistic gelatin. *AIP Conference Proceedings*, 1195:1399–1402, 2009. ISSN 0094243X. doi: 10.1063/1.3295071.

[34] Y. Toyoda and Y. M. Gupta. Shockless and shock wave compression of ballistic gel to 1.3 GPa. *Journal of Applied Physics*, 116(15), 2014. ISSN 10897550. doi: 10.1063/1.4898679. URL `http://dx.doi.org/10.1063/1.4898679`.

[35] Weinong Wayne Chen. Experimental Methods for Characterizing Dynamic Response of Soft Materials. *Journal of Dynamic Behavior of Materials*, 2(1):2–14, 2016. ISSN 21997454. doi: 10.1007/s40870-016-0047-5.

[36] B. Song, C. J. Syn, Chris L. Grupido, W. Chen, and W. Y. Lu. A Long Split Hopkinson Pressure Bar (LSHPB) for intermediate-rate characterization of soft materials. *Experimental Mechanics*, 48(6):809–815, 2008. ISSN 00144851. doi: 10.1007/s11340-007-9095-z.

[37] Srinivasan S. Naarayan and Ghatu Subhash. Wave propagation in ballistic gelatine. *Journal of the Mechanical Behavior of Biomedical Materials*, 68(October 2016):32–41, 2017. ISSN 18780180. doi: 10.1016/j.jmbbm.2017.01.030.

[38] L. Liu, Z. Jia, X. L. Ma, and Y. R. Fan. Analytical and experimental studies on the strain rate effects in penetration of 10wt % ballistic gelatin. *Journal of Physics: Conference Series*, 451(1), 2013. ISSN 17426596. doi: 10.1088/1742-6596/451/1/012035.

[39] C. R. Siviour, W. G. Proud, D. A. Salisbury, and R. E. Winter. High strain rate compressive behaviour of a Silicone elastomer. *Society for Experimental Mechanics - 11th International Congress and Exhibition on Experimental and Applied Mechanics 2008*, 1:407–413, 2008.

[40] K. Ravi-Chandar. *Dynamic fracture*. Academic Press, 2004. ISBN 9780080472553. doi: 10.1016/B978-008044352-2/50011-9. URL `http://dx.doi.org/10.1016/B978-0-12-443341-0.50071-5`.

[41] Matt P. Milner and Shelby B. Hutchens. Multi-crack formation in soft solids during high rate cavity expansion. *Mechanics of Materials*, (Under review), 2020.

[42] H. Zhang and K. Ravi-Chandar. *On the dynamics of necking and fragmentation - I. Real-time and post-mortem observations in Al 6061-O*, volume 142. 2006. ISBN 1070400690247. doi: 10.1007/s10704-006-9024-7.

[43] M. Z. Liang, X. Y. Li, J. G. Qin, and F. Y. Lu. Improved expanding ring technique for determining dynamic material properties. *Review of Scientific Instruments*, 84(6): 2–7, 2013. ISSN 00346748. doi: 10.1063/1.4811658.

[44] Nevill Francis Mott. Fragmentation of shell cases. *Proceedings of the Royal Society of London. Series A. Mathematical and Physical Sciences*, 189(1018):300–308,

may 1947. ISSN 2053-9169. doi: 10.1098/rspa.1947.0042. URL `http://www.royalsocietypublishing.org/doi/10.1098/rspa.1947.0042`.

[45] D. E. Grady. Local inertial effects in dynamic fragmentation. *Journal of Applied Physics*, 53(1):322–325, 1982. ISSN 00218979. doi: 10.1063/1.329934.

[46] D.E. Grady and M.E. Kipp. Mechanisms of dynamic fragmentation: Factors governing fragment size. *Mechanics of Materials*, 4(3-4):311–320, dec 1985. ISSN 01676636. doi: 10.1016/0167-6636(85)90028-6. URL `http://linkinghub.elsevier.com/retrieve/pii/0167663685900286`.

[47] Finn Ouchterlony. Fracture mechanics applied to rock blasting. *3rd Congr. of Int. Soc. for Rock Mechanics*, pages 1377–1382, 1974.

[48] D.E. Grady and M.E. Kipp. *Dynamic Rock Fragmentation*. 1987. ISBN 0-12-066265-5. doi: 10.1016/B978-0-12-066266-1.50015-6. URL `http://linkinghub.elsevier.com/retrieve/pii/B9780120662661500156`.

[49] Shengqiang Cai, Katia Bertoldi, Huiming Wang, and Zhigang Suo. Osmotic collapse of a void in an elastomer: Breathing, buckling and creasing. *Soft Matter*, 6(22): 5770–5777, 2010. ISSN 1744683X. doi: 10.1039/c0sm00451k.

[50] Lihua Jin and Zhigang Suo. Smoothening creases on surfaces of strain-stiffening materials. *Journal of the Mechanics and Physics of Solids*, 74: 68–79, 2015. ISSN 00225096. doi: 10.1016/j.jmps.2014.10.004. URL `http://dx.doi.org/10.1016/j.jmps.2014.10.004http://ac.els-cdn.com/S0022509614002026/1-s2.0-S0022509614002026-main.pdf?{_}tid=474b4cbc-75fc-11e6-a411-00000aab0f26{&}acdnat=1473363887{_}c56576b33f7d5b3b11169e5055179c1c`.

[51] Matt P. Milner, Lihua Jin, and Shelby B. Hutchens. Creasing in evaporation-driven cavity collapse. *Soft Matter*, 13:6894–6904, 2017. ISSN 1744-683X. doi: 10.1039/C7SM01258F. URL `http://xlink.rsc.org/?DOI=C7SM01258F`.

[52] James W Ward, L H Montgomery, and Sam L Clark. A Mechanism of Concussion: A Theory. *Science*, 107(2779):349–353, 1948. ISSN 00368075, 10959203. URL `http://www.jstor.org/stable/1674283`.

[53] David F Meaney and Douglas H Smith. Biomechanics of Concussion. *Clinics in Sports Medicine*, 30(1):19–31, 2011. ISSN 0278-5919. doi: j.csm.2010.08.009. URL `http://dx.doi.org/10.1016/j.csm.2010.08.009`.

[54] Eyal Bar-Kochba, Mark T Scimone, Jonathan B Estrada, and Christian Franck. Strain and rate-dependent neuronal injury in a 3D in vitro compression model of traumatic brain injury. *Sci. Rep*, 6(30550):1–11, 2016. doi: 10.1038/srep30550. URL `http://dx.doi.org/10.1038/srep30550`.

[55] M R Bailey, V A Khokhlova, O A Sapozhnikov, S G Kargl, and L A Crum. Physical Mechanisms of the Therapeutic Effect of Ultrasound (A Review). *Acoustical Physics*, 49(4):369–388, 2003.

[56] L Auren M Ancia, E L I V Laisavljevich, Z X U Hen, and E R I C J Ohnsen. PREDICTING TISSUE SUSCEPTIBILITY TO MECHANICAL CAVITATION DAMAGE IN THERAPEUTIC ULTRASOUND. *Ultrasound in Medicine & Biology*, 43(7):1421–1440, 2017. doi: j.ultrasmedbio.2017.02.020.

[57] B. Hopkinson. A Method of Measuring the Pressure Produced in the Detonation of High Explosives or by the Impact of Bullets. *Philosophical Transactions of the Royal Society A: Mathematical, Physical and Engineering Sciences*, 213(497-508): 437–456, jan 1914. ISSN 1364-503X. doi: 10.1098/rsta.1914.0010. URL `https://royalsocietypublishing.org/doi/pdf/10.1098/rsta.1914.0010http://rsta.royalsocietypublishing.org/cgi/doi/10.1098/rsta.1914.0010`.

[58] H. Kolsky. An Investigation of the Mechanical Properties of Materials at very High Rates of Loading. *Proceedings of the Physical Society. Section B*, 62 (11):676–700, nov 1949. ISSN 0370-1301. doi: 10.1088/0370-1301/62/11/302. URL `http://stacks.iop.org/0370-1301/62/i=11/a=302?key=crossref.84fee5d9bc50edaea3f7f9c83024c2cc`.

[59] W Chen, B Zhang, and M J Forrestal. A split Hopkinson bar technique for low-impedance materials. *Experimental Mechanics*, 39(2):81–85, jun 1999. ISSN 0014-4851. doi: 10.1007/BF02331109. URL `https://link.springer.com/content/pdf/10.1007{%}2FBF02331109.pdfhttp://link.springer.com/10.1007/BF02331109`.

[60] P. H. Mott, J. N. Twigg, D. F. Roland, H. S. Schrader, J. A. Pathak, and C. M. Roland. High-speed tensile test instrument. *Review of Scientific Instruments*, 78(4):045105, 2007. ISSN 00346748. doi: 10.1063/1.2719643. URL `http://scitation.aip.org/content/aip/journal/rsi/78/4/10.1063/1.2719643`.

[61] Michael J. Kendall, Daniel R. Drodge, Richard F. Froud, and Clive R. Siviour. Stress gage system for measuring very soft materials under high rates of deformation. *Measurement Science and Technology*, 25(7): 075603, jul 2014. ISSN 0957-0233. doi: 10.1088/0957-0233/25/7/075603. URL `http://stacks.iop.org/0957-0233/25/i=7/a=075603?key=crossref.3d53932f4df799fe4fadfd484cd3d22c`.

[62] C. Schyma and B. Madea. Evaluation of the temporary cavity in ordnance gelatine. *Forensic Science International*, 214(1-3):82–87, 2012. ISSN 03790738. doi: 10.1016/j.forsciint.2011.07.021. URL `http://dx.doi.org/10.1016/j.forsciint.2011.07.021`.

[63] Yaoke Wen, Cheng Xu, Yongxi Jin, and R. C. Batra. Rifle bullet penetration into ballistic gelatin. *Journal of the Mechanical Behavior of Biomedical Materials*, 67(June 2016):40–50, 2017. ISSN 18780180. doi: 10.1016/j.jmbbm.2016.11.021. URL `http://dx.doi.org/10.1016/j.jmbbm.2016.11.021`.

[64] Yaoke Wen, Cheng Xu, Haosheng Wang, Aijun Chen, and R.C. Batra. Impact of steel spheres on ballistic gelatin at moderate velocities. *International Journal of Impact Engineering*, 62:142–151, dec 2013. ISSN 0734743X. doi: 10.1016/j.ijimpeng.2013.07.002.

[65] Randy A. Mrozek, Brad Leighliter, Christopher S. Gold, Ian R. Beringer, Jian H. Yu, Mark R. VanLandingham, Paul Moy, Mark H. Foster, and Joseph L. Lenhart. The relationship between mechanical properties and ballistic penetration depth in a viscoelastic gel. *Journal of the Mechanical Behavior of Biomedical Materials*, 44:109–120, 2015. ISSN 18780180. doi: 10.1016/j.jmbbm.2015.01.001.

[66] Martin L. Fackler. Wound Ballistics. *JAMA*, 259(18):2730, may 1988. ISSN 0098-7484. doi: 10.1001/jama.1988.03720180056033. URL `http://jama.jamanetwork.com/article.aspx?doi=10.1001/jama.1988.03720180056033`.

[67] M. L. Fackler. Gunshot wound review. *Annals of Emergency Medicine*, 28(2):194–203, 1996. ISSN 01960644. doi: 10.1016/S0196-0644(96)70062-8.

[68] Jorma Jussila. Measurement of kinetic energy dissipation with gelatine fissure formation with special reference to gelatine validation. *Forensic Science International*, 150(1):53–62, 2005. ISSN 03790738. doi: 10.1016/j.forsciint.2004.06.038.

[69] Huajie Shi, Jos Sinke, and Rinze Benedictus. Surface modification of PEEK by UV irradiation for direct co-curing with carbon fibre reinforced epoxy prepregs. *International Journal of Adhesion and Adhesives*, 73(August 2016):51–57, 2017. ISSN 01437496. doi: 10.1016/j.ijadhadh.2016.07.017. URL `http://dx.doi.org/10.1016/j.ijadhadh.2016.07.017`.

[70] Harold A. Rothbart. *CAM Design Handbook*. McGraw-Hill, 2004. ISBN 9780071377577. URL `https://www.standardsmedia.com/Cam-Design-Handbook-1944-book.html`.

[71] Ascher H. Shapiro. *The Dynamics and Thermodynamics of Compressible Fluid Flow*. John Wiley & Sons, New York, 1953.

[72] Prabhata K. Swamee and Akalank K. Jain. Explicit equation for pipe flow problems. *Journal of the Hydraulics Division*, 102(5):657–664, 1976.

[73] J. J. Hollerman. Wound ballistics is a model of the pathophysiology of all blunt and penetrating trauma. *Emergency Radiology*, 5(5):279–288, 1998. ISSN 10703004. doi: 10.1007/BF02749084.

[74] P. K. Stefanopoulos, D. E. Pinialidis, G. F. Hadjigeorgiou, and K. N. Filippakis. Wound ballistics 101: the mechanisms of soft tissue wounding by bullets. *European Journal of Trauma and Emergency Surgery*, 43(5):579–586, 2017. ISSN 16153146. doi: 10.1007/s00068-015-0581-1.

[75] William J. Bruchey Jr. and Daniel E. Frank. *Police Handgun Ammunition : Incapacitation Effects Volume I: Evaluation*. U.S. DEPARTMENT OF JUSTICE, 1983.

[76] Steven Yang, Davin Bahk, Jiho Kim, Amrita Kataruka, Alison C. Dunn, and Shelby B. Hutchens. Hydraulic fracture geometry in ultrasoft polymer networks. *International Journal of Fracture*, 219(1):89–99, 2019. ISSN 15732673. doi: 10.1007/s10704-019-00380-y. URL `https://doi.org/10.1007/s10704-019-00380-y`.

[77] Randy A. Mrozek, Phillip J. Cole, Kathryn J. Otim, Kenneth R. Shull, and Joseph L. Lenhart. Influence of solvent size on the mechanical properties and rheology of polydimethylsiloxane-based polymeric gels. *Polymer*, 52(15):3422–3430, 2011. ISSN 00323861. doi: 10.1016/j.polymer.2011.05.021. URL `http://dx.doi.org/10.1016/j.polymer.2011.05.021`.

[78] B D Ragsdale and A Josselson. Predicting temporary cavity size from radial fissure measurements in ordnance gelatin. *The Journal of trauma*, 28:S5–S9, 1988. ISSN 0022-5282. doi: 10.1097/00005373-198801001-00003.

[79] Ericka K. Amborn, Karim H. Muci-Küchler, and Brandon J. Hinz. Experimental and numerical study of soft tissue surrogate behavior under ballistic loading. *ASME International Mechanical Engineering Congress and Exposition, Proceedings (IMECE)*, 2: 743–752, 2012. doi: 10.1115/IMECE2012-85724.

[80] D.E. Grady. The spall strength of condensed matter. *Journal of the Mechanics and Physics of Solids*, 36(3):353–384, jan 1988. ISSN 00225096. doi: 10.1016/0022-5096(88)90015-4. URL `https://linkinghub.elsevier.com/retrieve/pii/0022509688900154`.

[81] Dennis E. Grady. Length scales and size distributions in dynamic fragmentation. *International Journal of Fracture*, 163(1-2):85–99, 2010. ISSN 03769429. doi: 10.1007/s10704-009-9418-4.

[82] J. E. Field, S. M. Walley, W. G. Proud, H. T. Goldrein, and C. R. Siviour. *Review of experimental techniques for high rate deformation and shock studies*, volume 30. 2004. ISBN 4412233502. doi: 10.1016/j.ijimpeng.2004.03.005.

[83] Bo Song, Dan Casem, and Jamie Kimberley. Dynamic Behavior of Materials, Volume 1. In Bo Song, Dan Casem, and Jamie Kimberley, editors, *Proceedings of the 2013 Annual Conference on Experimental and Applied Mechanics*, volume 1 of *Conference Proceedings of the Society for Experimental Mechanics Series*, pages 1–477. Springer International Publishing, 2014. ISBN 978-3-319-00770-0. doi: 10.1007/978-3-319-00771-7. URL `http://link.springer.com/10.1007/978-3-319-00771-7{_}45http://link.springer.com/10.1007/978-3-319-00771-7`.

[84] Marc André Meyers. *Dynamic Behavior of Materials*. Wiley, sep 1994. ISBN 9780471582625. doi: 10.1002/9780470172278. URL `https://onlinelibrary.wiley.com/doi/book/10.1002/9780470172278`.

[85] Alan Arnold . A . Griffith. The phenomena of rupture and flow in solids. *Philosophical Transactions of the Royal Society of London.*, 221(582-593):163–198, jan 1920. ISSN 0264-3952. doi: 10.1098/rsta.1921.0006. URL `https://royalsocietypublishing.org/doi/10.1098/rsta.1921.0006`.

[86] M. L. Williams and R. A. Schapery. Spherical flaw instability in hydrostatic tension. *International Journal of Fracture Mechanics*, 1(1):64–72, 1965. ISSN 00207268. doi: 10.1007/BF00184154.

[87] Y. Y. Lin and C. Y. Hui. Cavity growth from crack-like defects in soft materials. *International Journal of Fracture*, 126(3):205–221, 2004. ISSN 03769429. doi: 10.1023/B:FRAC.0000026510.60747.3a.

[88] Oscar Lopez-Pamies, Martín I. Idiart, and Toshio Nakamura. Cavitation in elastomeric solids: I - A defect-growth theory. *Journal of the Mechanics and Physics of Solids*, 59 (8):1464–1487, 2011. ISSN 00225096. doi: 10.1016/j.jmps.2011.04.015.

[89] Jian Zhu, Tiefeng Li, Shengqiang Cai, and Zhigang Suo. Snap-through expansion of a gas bubble in an elastomer. *Journal of Adhesion*, 87(5):466–481, 2011. ISSN 00218464. doi: 10.1080/00218464.2011.575332.

[90] Jianyu Li, Zhigang Suo, and Joost J. Vlassak. Stiff, strong, and tough hydrogels with good chemical stability. *Journal of Materials Chemistry B*, 2(39):6708–6713, 2014. ISSN 2050750X. doi: 10.1039/c4tb01194e.

[91] Jianyu Li, Widusha R.K. Illeperuma, Zhigang Suo, and Joost J. Vlassak. Hybrid hydrogels with extremely high stiffness and toughness. *ACS Macro Letters*, 3(6):520–523, 2014. ISSN 21611653. doi: 10.1021/mz5002355.

[92] Jorma Jussila. Preparing ballistic gelatine - Review and proposal for a standard method. *Forensic Science International*, 141(2-3):91–98, 2004. ISSN 03790738. doi: 10.1016/j.forsciint.2003.11.036.

[93] Christopher W. Barney, Yue Zheng, Shuai Wu, Shengqiang Cai, and Alfred J. Crosby. Residual strain effects in needle-induced cavitation. *Soft Matter*, 15(37):7390–7397, 2019. ISSN 17446848. doi: 10.1039/c9sm01173k.

[94] A. E. Forte, F. D'Amico, M. N. Charalambides, D. Dini, and J. G. Williams. Modelling and experimental characterisation of the rate dependent fracture properties of gelatine gels. *Food Hydrocolloids*, 46:180–190, 2015. ISSN 0268005X. doi: 10.1016/j.foodhyd.2014.12.028. URL `http://dx.doi.org/10.1016/j.foodhyd.2014.12.028`.

[95] M Czerner, J Martucci, L A Fasce, R Ruseckaite, and P M Frontini. Mechanical and Fracture Behavior of Gelatin Gels. *13th International Conference on Fracture*, pages 1–10, 2013. ISSN 2283-995X. URL `http://ri.conicet.gov.ar/handle/11336/2617`.

[96] Ray W. Ogden. Incremental statics and dynamics of pre-stressed elastic materials. *CISM International Centre for Mechanical Sciences, Courses and Lectures*, 495:1–26, 2007. ISSN 23093706. doi: 10.1007/978-3-211-73572-5_1.

[97] M. Shams, M. Destrade, and R. W. Ogden. Initial stresses in elastic solids: Constitutive laws and acoustoelasticity. *Wave Motion*, 48(7):552–567, 2011. ISSN 01652125. doi: 10.1016/j.wavemoti.2011.04.004.

[98] Pavel I. Galich and Stephan Rudykh. Influence of stiffening on elastic wave propagation in extremely deformed soft matter: From nearly incompressible to auxetic materials. *Extreme Mechanics Letters*, 4:156–161, 2015. ISSN 23524316. doi: 10.1016/j.eml.2015.06.003. URL `http://dx.doi.org/10.1016/j.eml.2015.06.003`.

[99] Z. Abiza, M. Destrade, and R. W. Ogden. Large acoustoelastic effect. *Wave Motion*, 49(2):364–374, 2012. ISSN 01652125. doi: 10.1016/j.wavemoti.2011.12.002.

[100] Paul Weinacht, James F Newill, and Paul J Conroy. Conceptual Design Approach for Small-Caliber Aeroballistics With Application to 5 . 56-mm Ammunition. *Materials Research*, (September), 2005.

[101] Wei Hong, Xuanhe Zhao, and Zhigang Suo. Formation of creases on the surfaces of elastomers and gels. *Applied Physics Letters*, 95(11):111901, 2009. ISSN 00036951. doi: 10.1063/1.3211917. URL `http://scitation.aip.org/content/aip/journal/apl/95/11/10.1063/1.3211917`.

[102] Shengqiang Cai, Dayong Chen, Zhigang Suo, and Ryan C. Hayward. Creasing instability of elastomer films. *Soft Matter*, 8(5):1301, 2012. ISSN 1744-683X. doi: 10.1039/c2sm06844c.

[103] Dayong Chen, Shengqiang Cai, Zhigang Suo, and Ryan C Hayward. Surface Energy as a Barrier to Creasing of Elastomer Films: An Elastic Analogy to Classical Nucleation. *Physical Review Letters*, 109(3):038001, jul 2012. ISSN 0031-9007. doi: 10.1103/PhysRevLett.109.038001. URL `http://link.aps.org/doi/10.1103/PhysRevLett.109.038001`.

[104] Edwin P. Chan, Jeffrey M. Karp, and Robert S. Langer. A ”self-pinning” adhesive based on responsive surface wrinkles. *Journal of Polymer Science, Part B: Polymer Physics*, 49(1):40–44, 2011. ISSN 08876266. doi: 10.1002/polb.22165.

[105] Jinhwan Yoon, Pei Bian, Jungwook Kim, Thomas J. McCarthy, and Ryan C. Hayward. Local switching of chemical patterns through light-triggered unfolding of creased hydrogel surfaces. *Angewandte Chemie - International Edition*, 51(29):7146–7149, 2012. ISSN 14337851. doi: 10.1002/anie.201202692.

[106] Phanindhar Shivapooja, Qiming Wang, Beatriz Orihuela, Daniel Rittschof, Gabriel P. López, and Xuanhe Zhao. Bioinspired Surfaces with Dynamic Topography for Active Control of Biofouling. *Advanced Materials*, 25(10):1430–1434, mar 2013. ISSN 09359648. doi: 10.1002/adma.201203374. URL `http://doi.wiley.com/10.1002/adma.201203374`.

[107] Lihua Jin, Shengqiang Cai, and Zhigang Suo. Creases in soft tissues generated by growth. *EPL (Europhysics Letters)*, 95(September):64002, 2011. ISSN 0295-5075. doi: 10.1209/0295-5075/95/64002. URL `http://iopscience.iop.org/0295-5075/95/6/64002/fulltext/`.

[108] Tuomas Tallinen, Jun Young Chung, François Rousseau, Nadine Girard, Julien Lefèvre, and L. Mahadevan. On the growth and form of cortical convolutions. *Nature Physics*, 12(6):588–593, feb 2016. ISSN 1745-2473. doi: 10.1038/nphys3632. URL `http://www.nature.com/nphys/journal/v12/n6/pdf/nphys3632.pdfhttp://www.nature.com/doifinder/10.1038/nphys3632`.

[109] Jinhwan Yoon, Jungwook Kim, and Ryan C. Hayward. Nucleation, growth, and hysteresis of surface creases on swelled polymer gels. *Soft Matter*, 6(22):5807, 2010. ISSN 1744-683X. doi: 10.1039/c0sm00372g.

[110] Verónica Trujillo, Jungwook Kim, and Ryan C. Hayward. Creasing instability of surface-attached hydrogels. *Soft Matter*, 4(3):564, 2008. ISSN 1744-683X. doi: 10.1039/b713263h.

[111] Xudong Liang, Feiyu Tao, and Shengqiang Cai. Creasing of an everted elastomer tube. *Soft Matter*, 12(37):7726–7730, 2016. ISSN 1744-683X. doi: 10.1039/C6SM01381C. URL `http://dx.doi.org/10.1039/C6sm01381Chttp://xlink.rsc.org/?DOI=C6SM01381C`.

[112] Jelena Tomac, Durdica Cekinovć, and Jurica Arapović. Biology of the corpus luteum. *Periodicum Biologorum*, 113(1):43–49, 2011. ISSN 00315362.

[113] C. Llorens, M. Argentina, NO. Rojas, J. Westbrook, J. Dumais, and X. Noblin. The fern cavitation catapult: mechanism and design principles. *Journal of The Royal Society Interface*, 13(114):20150930, jan 2016. ISSN 1742-5689. doi: 10.1098/rsif.2015.0930. URL `http://www.ncbi.nlm.nih.gov/pubmed/26763327{%}5Cnhttp://www.pubmedcentral.nih.gov/articlerender.fcgi?artid=PMC4759797http://rsif.royalsocietypublishing.org/lookup/doi/10.1098/rsif.2015.0930`.

[114] Jacques Dumais and Yoël Forterre. "Vegetable Dynamicks": The Role of Water in Plant Movements, 2012. ISSN 0066-4189.

[115] E. Reyssat and L. Mahadevan. Hygromorph: from pine cone to biomimetic bilayers. *Journal of the Royal Society-Interface*, 6(June):951–957, 2009.

[116] SW. Lee, J. Prosser, PK. Purohit, and D. Lee. Bioinspired hygromorph actuator exhiniting controlled locomotion. *ACS Macro letter*, 2(11):960–965, 2013. ISSN 2161-1653. doi: 10.1021/mz400439a.

[117] Xavier Noblin, Sylvia Yang, and Jacques Dumais. Surface tension propulsion of fungal spores. *Journal of Experimental Biology*, 212(17):2835–2843, sep 2009. ISSN 0022-0949. doi: 10.1242/jeb.029975. URL `http://jeb.biologists.org/cgi/doi/10.1242/jeb.029975`.

[118] Patrick T. Martone, Michael Boiler, Ingo Burgert, Jacques Dumais, Joan Edwards, Katharine MacH, Nick Rowe, Markus Rueggeberg, Robin Seidel, and Thomas Speck. Mechanics without Muscle: Biomechanical inspiration from the plant world. *Integrative and Comparative Biology*, 50(5):888–907, 2010. ISSN 15407063. doi: 10.1093/icb/icq122.

[119] X. Noblin, N. O. Rojas, J. Westbrook, C. Llorens, M. Argentina, and J. Dumais. The Fern Sporangium: A Unique Catapult. *Science*, 335(6074):1322–1322, mar 2012. ISSN 0036-8075. doi: 10.1126/science.1215985. URL `http://www.sciencemag.org/cgi/doi/10.1126/science.1215985`.

[120] Y. Cao and J. W. Hutchinson. From wrinkles to creases in elastomers: the instability and imperfection-sensitivity of wrinkling. *Proceedings of the Royal Society A: Mathematical, Physical and Engineering Sciences*, 468(2137):94–115, 2012. ISSN 1364-5021. doi: 10.1098/rspa.2011.0384. URL `http://rspa.royalsocietypublishing.org/cgi/doi/10.1098/rspa.2011.0384`.

[121] A. N. Gent. A New Constitutive Relation for Rubber. *Rubber Chemistry and Technology*, 69(1):59–61, 1996. ISSN 0035-9475. doi: 10.5254/1.3538357.

[122] Xudong Liang and Shengqiang Cai. Gravity induced crease-to-wrinkle transition in soft materials. *Applied Physics Letters*, 106(4), 2015. ISSN 00036951. doi: 10.1063/1.4906933.

[123] R.G. Rice and D.D. Do. Dissolution of a solid sphere in an unbounded, stagnant liquid. *Chemical Engineering Science*, 61(2):775–778, jan 2006. ISSN 00092509. doi: 10.1016/j.ces.2005.08.003. URL `http://linkinghub.elsevier.com/retrieve/pii/S0009250905006573`.

[124] Greg C Randall and Patrick S Doyle. Permeation-driven flow in poly(dimethylsiloxane) microfluidic devices. *Proceedings of the National Academy of Sciences*, 102(31):10813–10818, aug 2005. ISSN 0027-8424. doi: 10.1073/pnas.0503287102. URL `http://www.pnas.org/cgi/doi/10.1073/pnas.0503287102`.

[125] Stephen J. Harley, Elizabeth A. Glascoe, and Robert S. Maxwell. Thermodynamic study on dynamic water vapor sorption in sylgard-184. *Journal of Physical Chemistry B*, 116(48):14183–14190, 2012. ISSN 15206106. doi: 10.1021/jp305997f.

[126] J. M. Watson and M. G. Baron. Precise static and dynamic permeation measurements using a continuous-flow vacuum cell. *Journal of Membrane Science*, 106(3):259–268, 1995. ISSN 03767388. doi: 10.1016/0376-7388(95)00090-Y.

[127] A N Gent and I S Cho. Surface Instabilities in Compressed or Bent Rubber Blocks. *Rubber Chemistry and Technology*, 72(2):253–262, may 1999. ISSN 0035-9475. doi: 10.5254/1.3538798. URL `http://rubberchemtechnol.org/doi/abs/10.5254/1.3538798`.

[128] Rachelle N. Palchesko, Ling Zhang, Yan Sun, and Adam W. Feinberg. Development of Polydimethylsiloxane Substrates with Tunable Elastic Modulus to Study Cell Mechanobiology in Muscle and Nerve. *PLoS ONE*, 7(12), 2012. ISSN 19326203. doi: 10.1371/journal.pone.0051499.

[129] I D Johnston, D K McCluskey, C K L Tan, and M C Tracey. Mechanical characterization of bulk Sylgard 184 for microfluidics and microengineering. *Journal of Micromechanics and Microengineering*, 24:035017, 2014. ISSN 0960-1317. doi: 10.1088/0960-1317/24/3/035017. URL `http://iopscience.iop.org/0960-1317/24/3/035017/article/`.

[130] T. Tallinen, J. S. Biggins, and L. Mahadevan. Surface sulci in squeezed soft solids. *Physical Review Letters*, 110(2):1–5, 2013. ISSN 00319007. doi: 10.1103/PhysRevLett.110.024302.

[131] Dayong Chen. *Creasing Instability of Hydrogels and Elastomers A Dissertation presented*. Doctoral dissertation, University of Massachusetts - Amherst, 2014. URL `http://scholarworks.umass.edu/dissertations{_}2/61/`.

[132] Tobias D. Wheeler and Abraham D. Stroock. The transpiration of water at negative pressures in a synthetic tree. *Nature*, 455(7210):208–212, sep 2008. ISSN 0028-0836. doi: 10.1038/nature07226. URL `http://www.nature.com/articles/nature07226`.

[133] K Sivasailam and C Cohen. Scaling behavior: Effect of precursor concentration and precursor molecular weight on the modulus and swelling of polymeric networks. *Journal of Rheology*, 44(4):897–915, 2000. ISSN 01486055. doi: 10.1122/1.551120.

[134] Robin P. Berkelaar, Erik Dietrich, Gerard A. M. Kip, E. Stefan Kooij, Harold J. W. Zandvliet, and Detlef Lohse. Exposing nanobubble-like objects to a degassed environment. *Soft Matter*, 10(27):4947, 2014. ISSN 1744-683X. doi: 10.1039/c4sm00316k. URL `http://xlink.rsc.org/?DOI=c4sm00316k`.